

ANALYTICAL APPLICATIONS OF TIME-RESOLVED POWERCHIP LASER
SPECTROSCOPY

By

JONATHAN ALAN MERTEN

A DISSERTATION PRESENTED TO THE GRADUATE SCHOOL
OF THE UNIVERSITY OF FLORIDA IN PARTIAL FULFILLMENT
OF THE REQUIREMENTS FOR THE DEGREE OF
DOCTOR OF PHILOSOPHY

UNIVERSITY OF FLORIDA

2011

© 2011 Jonathan Alan Merten

To Ray Kesler, who should have had this opportunity

ACKNOWLEDGMENTS

I would like to thank all of those who kept me on my feet physically and mentally through these years- Jim, Nico, Ben, Dr. Williams, Kay Niemax, Erick, Erin, Virginie and many dance partners, and my parents, especially my mother, an English major who once taught herself calculus so that I could finish high school.

TABLE OF CONTENTS

	<u>page</u>
ACKNOWLEDGMENTS.....	4
LIST OF TABLES.....	7
LIST OF FIGURES.....	8
LIST OF ABBREVIATIONS.....	11
ABSTRACT.....	14
CHAPTER	
1 INTRODUCTION TO MICROCHIP LASERS.....	16
Lasers.....	16
Microchip Lasers.....	17
2 DEVELOPMENT OF SINGLE PARTICLE AEROSOL FLUORESCENCE INSTRUMENT.....	23
Bacterial Fluorescence.....	23
Bioaerosol Instruments.....	26
Description of Instrumental Concept.....	28
Overview.....	28
High-Speed Operation.....	29
Low Speed Operation.....	30
Real Time Lifetime Measurement.....	30
Experimental.....	31
Results.....	36
Emission Spectra.....	36
Time-Resolved Fluorescence.....	37
Method performance.....	37
Bacterial lifetimes.....	38
Discussion.....	39
3 LASER INDUCED BREAKDOWN SPECTROSCOPY.....	61
Basics.....	61
Plasma Formation.....	61
Plasma formation- nanosecond laser pulses.....	63
Plasma formation-femtosecond laser pulse.....	64
Plasma formation- picosecond laser pulse.....	64
Plasma evolution and local thermodynamic equilibrium.....	66

MicroLIBS	70
Microchip LIBS.....	72
4 TIME-RESOLVED CHARACTERIZATION OF POWERCHIP LIBS PLASMA	77
Instrumentation	77
Laser-Sample Interaction.....	81
Plasma Dimensions	85
Time-Resolved Excitation Temperature.....	86
Time Resolved Electron Number Density	90
Microplasma LTE	93
5 SIGNAL TO NOISE RATIO CONSIDERATIONS IN POWERCHIP MICROLIBS .	115
Figures of Merit.....	115
Precision and Systematic Error	117
Limit of Detection.....	120
6 CONCLUSIONS	136
APPENDIX	
A SPECTROSCOPIC DATA FOR SELECTED IRON TRANSITIONS	139
B COMPOSITION OF ALUMINUM STANDARDS	140
LIST OF REFERENCES	142
BIOGRAPHICAL SKETCH.....	149

LIST OF TABLES

<u>Table</u>		<u>page</u>
2-1	Fluorescence parameters of selected bacterial fluorophores	48
2-2	Optical parameters calculated for different experimental uncertainties	48
4-1	Thermal properties of elements, molecules and mixtures	96
4-2	Time-resolved extended LTE calculations	97
A-1	Spectroscopic parameters for atomic iron lines used in excitation temperature calculations	139
B-1	Composition of aluminum standards used in LIBS microanalysis.....	141

LIST OF FIGURES

<u>Figure</u>		<u>page</u>
1-1	Optical diagram of microchip laser.	21
1-2	Optical diagram of powerchip laser	22
2-1	Schematic of aerosol instrument	49
2-2	Single shot decay profiles of aerosols in aerosol instrument	50
2-3	Benchtop fluorescence setup schematic.	51
2-4	Normalized fluorescence spectra of bacteria and allergens	51
2-5	Ethanol emission spectrum	52
2-6	Normalized bacterial fluorescence.....	53
2-7	Fluorescence spectra scaled to indicate relative intensities	53
2-8	Selected wavelength-resolved fluorescence decay profiles	54
2-9	Intensity averaged lifetimes of bacteria	56
2-10	Representative decay profiles and lifetime uncertainties at different single-shot S/N ratios	57
2-11	Effect of shot noise on lifetime fits	57
2-12	Lifetime standard deviation vs. wavelength for all species studied.....	58
2-13	Algorithm for generating synthetic decay profiles	59
2-14	Uncertainties in fitting synthetic decays as a function of number of integrated photons.....	60
3-1	Evolution of LIBS plasma- composition and radiation.....	76
4-1	LIBS microscope arrangement.	98
4-2	Knife-edge profiling of laser focus.	99
4-3	Calibration of relative ICCD gain.	99
4-4	CCD readout procedure.	100

4-5	Experimental timing with on-chip integration and readout register binning of region of interest.....	100
4-6	Shots required to drill through 0.001" aluminum sheet using 532nm laser.	101
4-7	Shots required to drill through 0.001" aluminum foil using 1064nm powerchip laser.....	102
4-8	Laser shots required to drill through 0.002" brass shim stock with 1064 laser .	103
4-9	Time resolved plasma diameter taken from H α line emission images	104
4-10	Time resolved plasma expansion velocities measured from H α images	105
4-11	Low-resolution spectrum of Fe lines in aluminum standard b8.....	106
4-12	Representative Boltzmann plot for temperature measurements using Fe lines	106
4-13	Variation of optical response across face of CCD	107
4-14	Effect of instrument response function (IRF) correction on iron emission lines in LIBS plasma.	108
4-15	Effect of IRF on calculated excitation temperature.	109
4-16	Time resolved temperatures under different atmospheres	110
4-17	Time-resolved H α line profiles from plasmas formed on aluminum under helium.....	111
4-18	Time-resolved aluminum plasma electron number densities in various atmospheres.....	112
4-19	Comparison of experimental electron number density under helium as a function of time and the corresponding value required to fulfill the McWhirter criterion.....	113
4-20	Comparison of experimental electron number density under air as a function of time and the corresponding value required to fulfill the McWhirter criterion .	113
4-21	Comparison of experimental electron number density under argon as a function of time and the corresponding value required to fulfill the McWhirter criterion.....	114
5-1	Laser shot energy distribution histograms recorded with a boxcar and an amplified photodiode	126
5-2	Iron calibration curve in aluminum matrix using 379.1nm.....	127

5-3	Excitation temperatures calculated from iron calibration curve data in aluminum samples.....	128
5-4	Excitation temperature and Fe calibration curve residuals	129
5-5	Correlation in residuals of iron calibrations using 371.9 and 376.3nm lines	130
5-6	Spectral standard deviation and RSD of copper in aluminum	131
5-7	S/N of Cu 327.4nm line vs. gate on delay	131
5-8	Background noise as a function of background signal at late gate onsets in aluminum sample n1075	132
5-9	Background noise as function of background signal with early gate onset.....	133
5-10	Binning regions for time-resolved S/N study.....	134
5-11	Time-resolved signal to background ratio in 327.4nm copper line.....	135

LIST OF ABBREVIATIONS

A/D	Analog to digital conversion
A_{mn}	Transition probability of state $m \rightarrow n$
c	Speed of light
DC	Direct current
CCD	Charge-coupled device
Cr:YAG	Chromium yttrium aluminum garnet
E_m	Energy of state m
FAD	Flavin adenine dinucleotide
FOM	Figure of merit
FWHM	Full width at half maximum
g_m	Statistical weight
h	Planck's constant
ICCD	Intensified charge-coupled device
IRF	Instrument response function
k	Boltzmann constant
LOD	Limit of detection
LTE	Local thermodynamic equilibrium
Laser	Light amplification by stimulated emission of radiation
LIBS	Laser-induced breakdown spectroscopy
LOFI	Laser optical feedback imaging
MALDI	Matrix-Assisted Laser Desorption Ionization
MCP	Microchannel plate
NA	Numerical aperture
NADH	Reduced nicotinamide adenine dinucleotide

NADPH	Reduced nicotinamide adenine dinucleotide phosphate
NATA	N-acetyl tryptophanamide
NATyrA	N-acetyl tyrosinamide
Nd:YAG	Neodymium doped yttrium aluminum garnet
n_e	Electron number density
$N(T)$	Number density
PLS	Partial least squares
PMT	Photomultiplier tube
RET	Resonance energy transfer
RSD	Residual standard deviation (typically expressed as %)
S/B	Signal to background ratio
S/N	Signal to noise ratio
STED	Stimulated emission depletion
T	Absolute temperature
t	Time
TCSPC	Time correlated single photon counting
TEM	Transverse electromagnetic mode
Trp	Tryptophan
$U(T)$	Partition function
UV	Ultraviolet
XeCl	Xenon chloride (laser)
α	Pre-exponential constant (unitless)
$\Delta\lambda$	Spectral line width
ϵ	Radiance
λ	Wavelength

π	Pi (3.14)
ρ	Density
σ	Standard deviation (units as average)
τ	Lifetime, time constant

Abstract of Dissertation Presented to the Graduate School
of the University of Florida in Partial Fulfillment of the
Requirements for the Degree of Doctor of Philosophy

ANALYTICAL APPLICATIONS OF TIME-RESOLVED POWERCHIP LASER
SPECTROSCOPY

By

Jonathan Alan Merten

August 2011

Chair: Nicolás Omenetto

Major: Chemistry

Microchip and powerchip lasers represent a new source of cheap, reliable pulsed radiance. With rugged passive Q-switches, they operate at frequencies $>1\text{kHz}$ and can produce pulses of 500ps or less. They have not found many applications in analytical chemistry to date. In this work, they have been evaluated for bacterial aerosol fluorescence detection and laser-induced breakdown spectroscopy (LIBS).

A single-particle aerosol sampler and concentrator has been constructed for detection and identification of bioaerosols using particle sizing and laser-induced fluorescence with the 4th harmonic of the powerchip laser. Fast detection of fluorescence with an analog system (microchannel plate photomultiplier tube and 6GHz oscilloscope) theoretically allows single-shot measurement of lifetimes. In order to evaluate this concept, spectrally resolved measurements of native fluorescence lifetimes were made with *Bacillus subtilis*, *Staphylococcus epidermis*, *Lactobacillus lactus*, *Micrococcus luteus*, and *Escherichia coli*. All species could be distinguished by their lifetime at a minimum of one wavelength. Signal to noise, however, was inadequate to make identifications from single cells.

The laser was also evaluated for use in LIBS. Powerchip lasers are an order of magnitude shorter in pulse duration than the typical laser employed in LIBS. Because of the jitter caused by their passive Q-switch, the temporal evolution of the powerchip-induced laser plasma has not been characterized previously. By operating a 532nm powerchip with a delay line, time-resolved temperatures, electron number densities and volume were recorded with a fast intensified charge-coupled device (ICCD) under various atmospheres. The usual trends among the different atmospheres, corresponding to the physical properties of the gases, were observed. The powerchip laser induced plasma figures of merit were also evaluated as a function of temporal gate position. Gating was shown to be beneficial in terms of limit of detection, although the ultimate limiting noise was continuum shot noise rather than detector dark noise. With evolving detector technology, these lasers will continue to find applications in analytical chemistry.

CHAPTER 1 INTRODUCTION TO MICROCHIP LASERS

Lasers

Maiman announced the first demonstration of laser action with 4 paragraphs in August of 1960 ¹. Although this first laser employed a flashlamp-pumped ruby rod as the gain medium and oscillator and Geusic and Marcos introduced the much more efficient neodymium-doped yttrium aluminum garnet (Nd:YAG) in 1964 ², it was mostly gas lasers that found their way into industrial and medical applications during the first few decades. More broadly, however, the laser remained a “solution without a problem” for many years, in spite of garnering Basov, Prokhrov and Townes the 1964 Nobel Prize for Physics. By 1970, however, the additional basic advances underlying microchip laser technology, including Q-switching and diode laser technology, had been published.

Lasers generally consist of three elements: a gain medium (solid, liquid, gas or plasma), a partially reflecting laser cavity (generally a pair of mirrors) that allows the selective buildup of stimulated emission by the gain medium, and a method of pumping energy into the lasing species in the gain medium. The gain medium is pumped out of equilibrium using a kinetic “trick” involving a fast transition into the upper lasing level, or out of the lower lasing level. The disequilibrium between the upper and lower laser levels allows amplification of photons corresponding to energy of the transition between the two lasing levels. Q-switching or cavity dumping mechanisms can be added to the cavity to concentrate the laser emission into short pulses of increased peak radiance.

Microchip Lasers

In 1989, Zayhowski and Mooradian published the first account of their rugged new microchip lasers³. Their new adaptation of solid-state lasers used a thin wafer of Nd:YAG gain medium (<1mm thick) with dielectrically-coated polished faces and transverse diode laser pumping at 808nm (Figure 1-1). The short cavity length ensured that only one of the widely-spaced cavity modes fell under the gain profile, providing single transverse mode operation, even when pumped at many times threshold.⁴ Gain guiding and nonlinear effects also contributed to beam quality, ensuring TEM₀₀ operation. The tiny cavities allowed for mass production since entire Nd:YAG wafers cut from boules could be polished and dielectrically coated before being diced into individual laser chips. Thus, a single boule yielded as many as 6000 lasers⁴. The small cavities also allowed for higher neodymium doping densities, as the required pump penetration depth is only a few times the transversely pumped cavity length.⁵

These short cavity lengths allow very short cavity lifetimes for pulsing or modulation. Various Q-switching paradigms have been tested, including replacing the output mirror with a tunable etalon⁶, saturable absorber codoping of the gain medium⁷, and electrooptic Q-switching⁸. Active Q-switching requires fast, high voltage electronics, and possibly maintenance of interferometric control of etalon positioning, increasing the price and size of the laser and decreasing robustness and reproducibility. Passive Q-switching has the advantage of simplicity and produces extremely uniform pulse profiles and energies. Commercial versions of Q-switched microchip lasers generally employ Cr⁴⁺:YAG saturable absorbers, which can be bonded into the monolithic microchip cavity prior to coating and dicing. In recent years, the microchip

cavity paradigm has been extended to other gain media, providing a variety of possible wavelengths in the near infrared and mid-visible wavelength region.

Microchip radiance has increased over the years. The initial microchips were driven with ~1W of pump power, and yielded tens to hundreds of milliwatts of fundamental output. By optimizing microchip laser operation with numerical models, Sakai et al. recently demonstrated a prototype microchip laser that produces >1MW peak power pulses at 100Hz (0.69mJ, 590ps).⁹ The laser used in this work (referred to as a Powerchip laser) was a modification of the initial microchip design whereby the laser cavity is extended without compromising the robustness of a monolithic cavity design. By sandwiching a traditional microchip cavity in between two additional regions of undoped YAG and depositing the cavity mirrors on the far edges of the new undoped regions, the laser mode volume within the doped Nd:YAG is increased, allowing more efficient use of the pump energy ¹⁰ (Figure 1-2) in a powerchip. The powerchip's larger cavity is pumped by a multiwatt lens-coupled diode laser bar.

In the powerchip laser used in this work, the laser pulse sequence begins when the pump diode current is turned on by a trigger pulse. The population inversion builds up within the Nd:YAG region, but does not oscillate due to absorption from the adjacent Cr⁺⁴-doped region. As the Cr⁺⁴ region bleaches due to the long upper state lifetime of the Cr⁺⁴ species, the now-saturated absorber begins to pass the Nd⁺ emission, allowing the buildup of the optical field between the mirrors, eventually resulting in optical amplification and a laser pulse. An internal transducer detects the emission of the optical pulse and turns the pump diode current back down to prevent emission of an additional pulse from the cavity before the next trigger pulse. The delay between the

start of laser pumping and the emission of the powerchip pulse is a function of the cavity build-up time and varies between 40 and 500 μ s.¹⁰ This jitter can complicate time-resolved analytical measurements, as will be discussed.

Because the laser uses a high wall plug-efficiency diode laser to pump the Nd:YAG gain medium with high spectral efficiency, the powerchip is cooled by two thermoelectric coolers and forced air. The laser head runs on 24V DC, with a maximum current of 5A, with 3A operating current (maximum). The laser head and associated electronics (excluding the power supply) weigh 5kg, and occupy ~ 30cm x 10cm x 15cm.

Although, like the original lasers, the microchip laser was initially a solution without a problem, analytical chemists have begun to appreciate its economical high peak power and repetition rate, as well as its potential in subnanosecond time-resolved spectroscopy. Hugon et al. took advantage of the short cavity lifetime of CW microchip lasers as both a signal source and a backscatter heterodyne detector with the potential to provide high-resolution, contrast-free 3d microscopic imaging of tissues via laser optical feedback imaging (LOFI).¹¹ Stefan Hell's lab has employed microchip laser-induced supercontinuum to generate depletion pulses for stimulated emission depletion (STED) sub-diffraction-limit microscopy.¹² Ritschdorff and Shear have used a 36kHz frequency doubled powerchip laser (532nm) to induce multiphoton photopolymerization, demonstrating cost-effective 3D printing of protein or acrylate microstructures with potential analytical applications.¹³ Similarly, Farnsworth's group used the high peak power of a frequency doubled microchip to demonstrate a two-photon fluorescence device capable of detecting 10⁻⁷M bovine serum albumin in a femtoliter volume.¹⁴

Finally, Gornushkin and others have used microchip lasers for laser-induced breakdown spectroscopy (LIBS) elemental analysis of solids.¹⁵

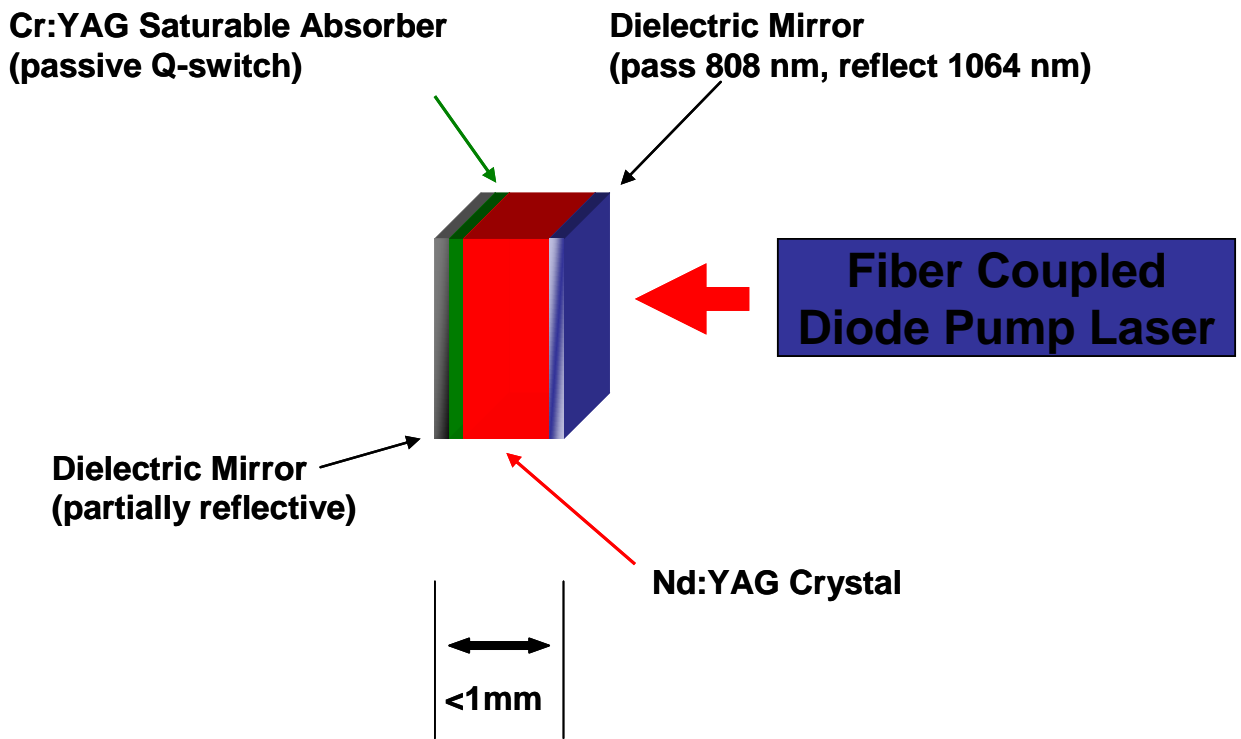


Figure 1-1. Optical diagram of microchip laser.

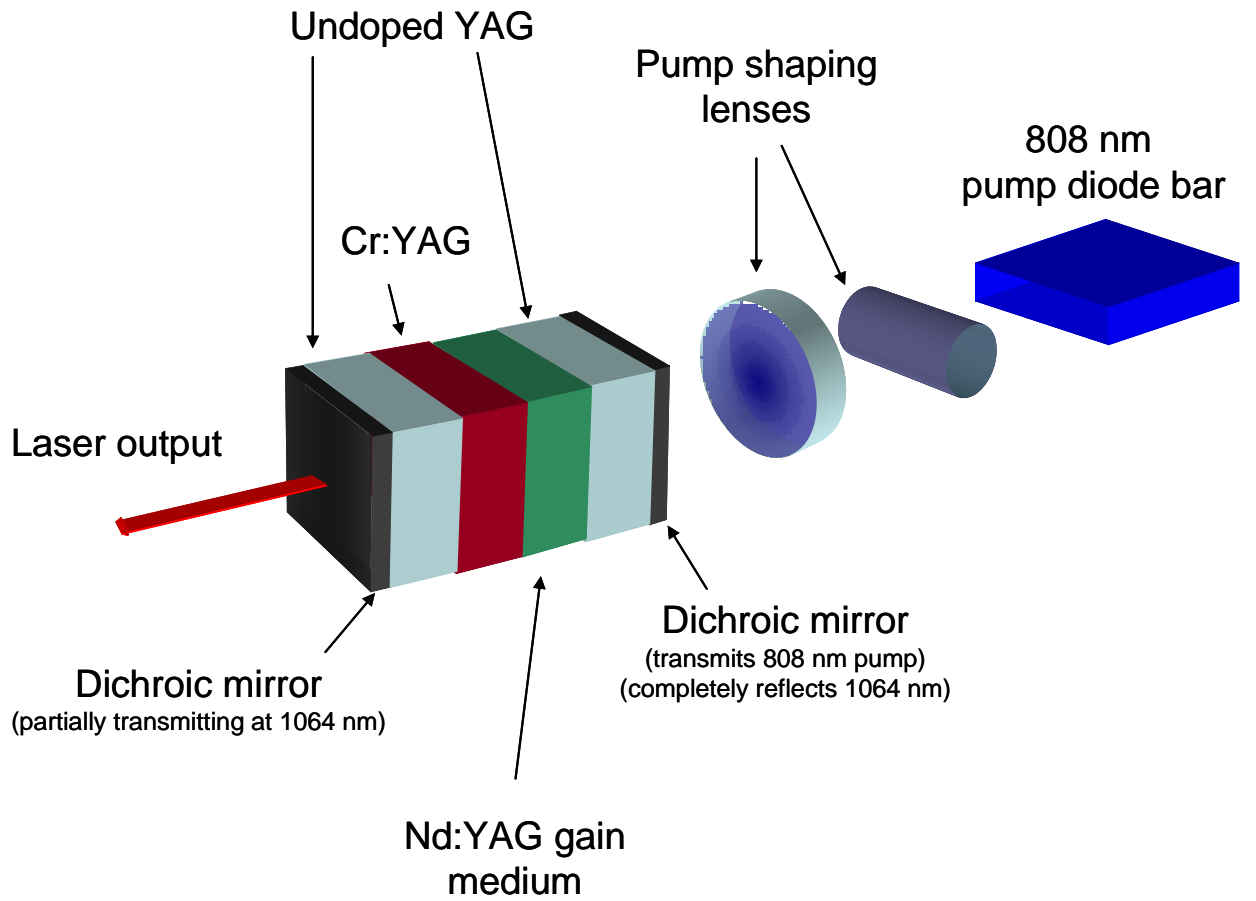


Figure 1-2. Optical diagram of powerchip laser. [Adapted from JDS-Uniphase *Diode Pumped Solid State PowerChip NanoLasers User's Manual*; 24 October 2002, 2002; p 45.]

CHAPTER 2 DEVELOPMENT OF SINGLE PARTICLE AEROSOL FLUORESCENCE INSTRUMENT

Bacterial Fluorescence

With a few intriguing exceptions, lasers are only available at a select number of wavelengths. In order to extend their usefulness, non-linear optics are used to generate beams of coherent light at other discrete wavelengths. Because the efficiency of such non-linear processes scales with the square of the pump intensity, microchip lasers with their high peak powers can be extended to the visible and ultraviolet where many organic fluorophores are excited.

Bacteria contain a number of fluorophores (Table 2-1). In the practical experimental terms relevant to this work, they fall into three groups according to their excitation spectra. The aromatic amino acids and the nucleic acids are all excited in the deep UV. NADH, pterins, and lumazine, on the other hand, are best excited in the mid-UV. FMN, FAD and riboflavin absorb in the near UV and far visible.

The deep UV-absorbing aromatic amino acids, phenylalanine, tyrosine and tryptophan have long been of interest in the biochemical and physical chemical community for the information that they provide about proteins. Of these, tryptophan is the most studied. It is known, for instance, that the emission spectrum of protein tryptophan residues is a function of the residue's immediate environment; tryptophan residues in a hydrophobic protein core show the more vibrationally structured emission of indole dissolved in cyclohexane, while tryptophan residues exposed to water exhibit a more red-shifted, unstructured emission.¹⁶

Tryptophan's lifetime dependence as a function of emission wavelength is even more complex, and does not follow a clear trend with emission maximum, as might

otherwise be expected.¹⁶ Free tryptophan displays a biexponential decay, with the separate lifetimes thought to be the result of different rotamers.¹⁷ The neutral tryptophan analogue, N-acetyl-tryptophanamide, however, shows a single exponential decay, and would be expected to mimic the decay characteristics of tryptophan residues in polypeptides.¹⁷ (Table 2-1) Nonetheless, even single-tryptophan containing proteins demonstrate multiexponential decays, possibly due to different protein conformations.¹⁶

Tyrosine, on the other hand, shows a single exponential decay in solution, but the neutral analogue shows a biexponential decay.¹⁸ There is very little information on the fluorescence decay dynamics of phenylalanine, though a single lifetime of ~5ns has been reported.¹⁹ Fluorescence intensity from individual residues in proteins with deeper UV emission spectra is decreased by resonance energy transfer (RET) from phenylalanine→tyrosine→tryptophan, and even from tryptophan_{high_energy}→tryptophan_{low_energy} within the macromolecules.¹⁶ In order to simplify the interpretation of spectral and lifetime data, studies of protein fluorescence frequently use longer wavelength excitation (295nm and longer) to selectively excite tryptophan. Nonetheless, various authors have generalized that the majority of protein fluorescence is from tryptophan.²⁰ This generalization may still apply to Nd:YAG-excited fluorescence of mixtures of proteins, in spite of the short excitation wavelength (266nm), due to the low quantum yields of phenylalanine and tyrosine, as well as their propensity for RET.

Among the biological fluorophores, NADH has also seen a significant amount of research. In solution, free NADH exhibits a single lifetime of 0.4ns, while bound NADH exhibits lifetimes in excess of 1ns.²¹ In fact, Lakowicz and colleagues first introduced

fluorescence imaging microscopy (FLIM) by imaging the fluorescence lifetimes of adjacent cuvettes of free and protein-bound NADH.²²

There has been a resurgence in interest in laser induced fluorescence detection of microorganisms recently, especially in instruments for the real-time detection and identification of single biological particles. Fluorescence detection and discrimination of microorganisms has been covered in a recent review.²³ Bioaerosol detection by intrinsic fluorescence has been reviewed as well.²⁴

The bulk of the intrinsic fluorescence experiments thus far have used time-integrated, spectrally resolved information to classify or detect the bacteria. For example, fluorescence spectra and principle component analysis have been used to discriminate between lactic acid bacteria isolated from a sausage factory.²⁵ Likewise, Ammor et al. have used PCA (principle component analysis) and fluorescence spectra to discriminate among cultures of different species and subspecies of the *Bifidobacterium* genus.²⁶ Fluorescence excitation-emission matrices have been successful in fiber optic based in-vivo discrimination between otitis media cases caused by three different clinically relevant bacteria.²⁷

Time-resolved fluorescence identification of bacteria has been less discussed, perhaps because the equipment required is less common. Brahma et al. first suggested the possibility of discriminating among bacteria by their fluorescence decay profiles in 1985.²⁸ Dalterio and coworkers expanded the experiments to multiple ultraviolet excitation and emission wavelengths and speculated on the molecular source of the various decay lifetimes.²⁹ More recently, Thomas et al. have taken advantage of modern high-bandwidth oscilloscopes and fast detectors to make analog measurements

of bacterial lifetimes, in contrast to the scanned boxcar and TCSPC (time correlated single photon counting) measurements of the earlier works.³⁰ They found that emission wavelength-resolved lifetimes could be used to discriminate among a limited variety of bacteria and potentially confounding particles.

Bioaerosol Instruments

Real-time bioaerosol detection and discrimination is a far more intractable problem than the bulk laboratory experiments described above. Several instruments have been constructed to address the problem, but the minimal signal available from single interrogations of entrained particles remains a problem for discriminating particles. TSI Incorporated has developed and commercialized several generations of the UVAPS (ultraviolet aerosol particle sizer), adding a fluorescence channel to their conventional laser velocimeter particle sizer.³¹ The instrument measures particle aerodynamic diameter via laser time-of flight velocimetry and measures particle fluorescence emission at one (or more recently, several³²) discrete wavelengths, as selected by filters. This instrument has been through several incarnations, initially employing a 354 and 325nm CW HeCd laser to excite the laser fluorescence. Subsequently, the CW laser was replaced with a pulsed diode pumped solid state (DPSS) Q-switched neodymium yttrium lithium fluoride (Nd:YLF) laser frequency tripled to produce 30 μ J, 5-8ns pulses at 349nm.³³ Operating with a pulsed laser in such instruments requires a complex timing circuit due to the size-specific particle velocity.³⁴ The current commercial model of the UVAPS employs a 30 mW 405nm CW diode laser. Ho et al. envision it as a non-specific potential threat (i.e. high concentration bioaerosol) detector that would trigger a subsequent, more selective wet chemistry assay.²⁴

The Yale University Center for Laser Diagnostics has developed a similar instrument capable of conditionally recording spectra from single particles in real time.³⁵ The instrument draws the aerosol through a CW-laser scatter detection region. When laser scatter from a particle is detected, a pulsed Nd:YAG (266 or 355nm) laser is fired at a fixed delay after detection of CW laser scatter.³⁶ Unlike the TSI instrument, however, this instrument does not provide data on particle size. Chang et al. do, however, incorporate a degree of potential selectivity by dispersing the fluorescence across a 32 anode PMT and separately sampling the charges accumulated at each of the anodes to generate a fluorescence spectrum.³⁶

Other fluorescence excitation sources have been investigated. Chang et al. experimented with LED microarrays at 290 and 340nm to acquire spectra of aerosolized tryptophan and NADH particles.³⁷ Their linear microarray is fired in coordinated sequential microsecond pulses, tracking the particle's trajectory past the array of LED junctions, thereby increasing the total radiant exposure from an otherwise low peak-radiance source. Kaye et al. have excited single bioaerosol particles with broadband Xe flashlamps and bandpass filters selected for the excitation bands of NADH or amino acid absorption.³⁸ They collected a single spectral emission channel for each lamp and did not generate spectra. It is interesting to note that the particle probing rate in this system is limited by the demanding thermal dissipation requirements of the broadband Xe lamp.

In addition to these optical systems, several mass spectrometric instruments have been developed to address the problem of bioaerosol detection and discrimination. Stowers et al. have incorporated a fluorescence preselection circuit into

their XeCl vacuum laser-desorption ionization aerosol mass spectrometer, allowing them to increase the effective data acquisition rate of their instrument.³⁹ Furthermore, their group has developed an online bioaerosol MALDI interface chamber to coat particles with MALDI matrix prior to drawing them into the mass spectrometer.⁴⁰ Lawrence Livermore National Laboratory has also developed a dual-polarity bioaerosol time of flight mass spectrometer (BAMS) capable of distinguishing between two species of *Bacillus* spores using the ions desorbed from them by a pulsed 266nm laser.⁴¹

Description of Instrumental Concept

Overview

Our lab has developed a flexible bioaerosol instrument incorporating aerosol preconcentration, aerodynamic sizing, and laser induced fluorescence.³⁴ (Figure 2-1) The instrument is based around a series of adjustable aerodynamic lenses designed and optimized using FLUENT.⁴² Ambient aerosol is sampled through a flow limiting critical orifice. The aerosol flow relaxes, then passes through an aerodynamic lens. The lenses can be used as a size filter to select a specific range of particle diameters (size segregator), or can be used to concentrate a broad range of particles into a collimated particle beam. Collimation serves to increase the system efficiency, allowing the sampling of large volumes of low-density aerosols through a small detection region.

The particles proceed through a skimmer into the sizing and characterization chamber. The particle velocity beyond the skimmer is a function of the pressure of the final chamber. At high downstream pressures, the particles are accelerated by the supersonic expansion at the skimmer, but then relax back to lower speeds due to drag in the downstream gas. At sufficiently low downstream pressures, the particle is accelerated by the supersonic expansion without subsequent relaxation in the low-

pressure sizing region. The experimental details of the probe modality in the final chamber are tailored to the pressure regime used as detailed below.

High-Speed Operation

When the pressure downstream of the sizing chamber is maintained below 10^{-4} mbar by a turbodrag pump, collisions with the gas are negligible. Thus, the particle is accelerated by the supersonic expansion, acquiring and maintaining an aerodynamic size-dependent final velocity on the order of 10^2 m/s. The particle beam is intercepted by two CW argon-ion laser beams. Particle scatter from each of the beams is collected by a PMT, then conditioned into TTL pulses. The time of flight delay between the two pulses is inversely proportional to the particle speed (and therefore its aerodynamic diameter). This time of flight/diameter relationship can be calibrated with an aerosol of standard spheres.

The first scatter TTL pulse also starts a countup circuit running at an adjustable frequency. The counter is stopped by the second TTL pulse. The pulse count is then used in a countdown circuit triggered at the fraction of the countup frequency corresponding to the ratio of the trigger beam spacing to the subsequent distance from the second trigger laser to the probing volume.⁴³ The countdown circuit is used to trigger a low-jitter laser to coincide with the particle's arrival at the probing region. Wu et al. have determined that the particle incidence rate must be kept below ~ 15 Hz to prevent particle coincidence and resulting artifacts in the particle sizing.⁴⁴ It should be noted that commercial passively Q-switched powerchip lasers are not compatible with this operating regime because of their microsecond-level jitter.

Low Speed Operation

When the pressure in the sizing chamber is on the order of one millibar, particle speed in the probing region is $\sim 10^{-1}$ m/s, and laser velocimetry for conditional triggering is no longer feasible, since the particles relax back to the speed of the carrier gas.³⁴ The long particle residence time in the probe region at these speeds allows multiple probings with a high repetition rate powerchip laser. Note that the DAQ device (ICCD or oscilloscope) must be triggerable at the laser repetition rate if multiple shots of a passively Q-switched powerchip laser are used to interrogate the particle.

Real Time Lifetime Measurement

Particle mass is given by:

$$mass = \frac{\pi d^3 \rho}{6} \quad (2-1)$$

where ρ is the particle density and d is the particle diameter. Assuming a density of 1.0 g/cm^3 , a $1.0 \mu\text{m}$ particle has a mass of 0.52 pg . Single shot fluorescence measurements from such a small sample will be signal shot-noise limited as long as detectors are operated with sufficiently high gain. In order to maximize the S/N ratio of the measurement, the excitation irradiance may be increased up to a maximum imposed by the breakdown limit of the particle (or the onset of some other nonlinearity), and the throughput of the collection optics must be maximized. Elliptical mirrors are well suited for this purpose as they can collect a high fraction (0.4) of the 4π steradians emitted by a particulate point source, they can be made relatively spectrally flat, and they should add an insignificant level of fluorescence background in the event of significant scatter of a deep UV excitation pulse.³⁴

As shown in Figure 2-2, previous work in our lab has demonstrated that single shots of $\sim 2\mu\text{J}$ are capable of producing high S/N fluorescence decay profiles from aerosolized pure tryptophan particles.³⁴ In this case, an undetermined number of $\sim 0.7\mu\text{m}$ tryptophan particles or $1.09\mu\text{m}$ polystyrene spheres is present in the laser beam. The two decays are visually distinguishable, differing by nearly an order of magnitude in their lifetime. It is unclear, however, if single biological particles can generate adequate S/N ratios for fluorescence detection, much less for discrimination given their lower concentration of fluorophore. Consequently, we have conducted benchtop cuvette experiments with bacteria and other potential bioaerosol particles as well as computational “synthetic” fluorescence experiments to address these questions.

Experimental

The optics setup used for the steady-state and time-resolved fluorescence measurements is shown in Figure 2-3. The second harmonic output ($20\mu\text{J}$) of the JDS Uniphase Nanolase Powerchip Nd:YAG laser was doubled using a type 1 (Photox Optical Systems, $\theta=47.7^\circ$) BBO crystal to produce 266nm pulses with a FWHM $<500\text{ps}$. Pulse energy was greater than $7\mu\text{J}$ at 266nm . The second and fourth harmonics were separated by passing them through a Glan-Thompson calcite polarizer, followed by further attenuation of the 532nm light with either a colored glass filter or a shortpass filter. The post-filter UV energy was adjusted with neutral density filters to keep it below $1.5\mu\text{J}/\text{pulse}$. The laser was factory optimized for operation at a kilohertz, but can operate with single external triggering for pulse on demand.

Fluorescence was collected at 90° with a fused silica lens matched to the F/n of the 0.14m Jobin-Yvon MicroHR emission monochromator. The $1200\text{g}/\text{mm}$ grating was blazed at 330nm . The monochromator was rotated in order to fill the complete height of

the slit. The spectral bandpass was nominally 10nm. A 532nm colloidal notch filter placed in front of the entrance slit was used to reject both 266 and 532nm stray light.

A Hamamatsu R1564U-07 MCP PMT operated at -3100V was coupled either to a Stanford Research SR 250 boxcar for time-integrated measurements, or to a TDS6604 digitizing oscilloscope (6GHz, 20Gs/s) for time-resolved measurements. The boxcar was triggered off of the laser's internal photodiode, with the gate set to encompass the entire width of the fluorescence emission. Boxcar output was offset and scaled with an SR225 analog processor, then digitized with a National Instruments USB6009 DAQ. Each point in the spectra is an average of 12 laser shots. In order to guarantee that the emission spectra reflect the emission at the short delays examined in time-resolved measurements, the PMT signal was not amplified prior to the boxcar. Thus, the noise present in triggering the boxcar limited the signal to noise ratio of spectra, necessitating averaging. Fluorescence measurements were uncorrected for the instrument's spectral response function. During time-resolved measurements, the oscilloscope was set to operate in real time, limiting the time resolution to 50ps/pt and the total record length to 50ns. Decay profiles were taken every 10nm from 290nm to 430nm. A variable attenuation neutral density filter in the excitation laser beam path was used to keep the maximum of the time-resolved fluorescence signal below 400mV. By attenuating the signal to match the electronics, the S/N could be kept more constant across the emission spectrum, which could vary by more than an order of magnitude between the peak emission wavelength and 430nm (the longest wavelength employed in the lifetime measurements).

All solutions and suspensions were prepared with MilliQ water and Fisher Certified ACS grade reagents, and were checked for background fluorescence prior to use. Bacteria (*Bacillus subtilis*, *Staphylococcus epidermis*, *Lactobacillus lactus*, *Micrococcus luteus*, and *Escherichia coli*) were cultured on nutrient agar plates to stationary phase in the University of Florida Microbiology department, then gently scraped and washed into centrifuge tubes with 10mL of pH 7 phosphate buffered saline (PBS). Tubes were vortexed, then centrifuged. Supernatant was pipetted off and the plug was resuspended in an equal volume of fresh PBS. The process was repeated for a total of 4 centrifugings. Washed suspensions were stored overnight at 4 °C. The suspensions were brought to room temperature for measurements, diluting in a 1cm² fused silica cuvette with fresh PBS to give an optical density of 0.30, corresponding to approximately 3.5x10⁸cfu/mL, though no attempt was made to calibrate this relationship. Optical densities were measured at 600nm with an Ocean Optics SD2000 fiber optic spectrometer and a tungsten lamp. Cuvettes were stirred with magnetic stirbars during both optical density and fluorescence measurements. Bermuda grass smut (*Ustilago cynodontis*), corn smut (*Ustilago maydis*) and Bermuda grass pollen (*Cynodon dactylon*) powdered allergen samples were purchased from Greer Laboratories (Lenoir, NC) and were suspended in PBS to an optical density of 0.30 without any further processing.

Precautions were taken to minimize the UV exposure of the samples in the course of measurements in order to avoid potential artifacts due to photobleaching. The PMT was operated at high gain to ensure that the S/N ratio was signal shot noise dominated at the given laser energy. Laser firing, monochromator grating movement,

and DAQ/scope acquisition were controlled with programs written in Labview. During the decay profile acquisitions at each wavelength, the number of laser shots was exactly matched to the averaging settings of the oscilloscope (500 waveforms), as well as its 300Hz maximum trigger rate. Likewise, while scanning to measure fluorescence emission spectra, laser firing at each wavelength was exactly matched to the boxcar averaging settings. Spectra were always taken subsequent to lifetime measurements, as the latter were the main focus of the research. In order to minimize the total UV irradiance on a given cell, the ~3mL volume of the cuvette was stirred continuously during measurements. Also, measurements from each suspension were performed in 3 replicate cuvettes to further improve S/N without increasing the total irradiation within a single cuvette. Total sample exposure during lifetime determinations was less than 12mJ, with an additional 4.5mJ during emission spectral determinations. Spectra were taken without amplifying the PMT signal to ensure that only the nanosecond-regime portion of luminescence was measured. Similarly, the boxcar gate was set to integrate the entire nanosecond-regime signal since an optimized gate would have favored the fast-decaying components' spectra. This did have the effect of decreasing S/N ratio in the spectra, however.

The lifetime instrument's temporal response function (IRF) was measured by scattering the 266nm beam off of 1 μ m silica spheres (Bangs Laboratories) in a cuvette with the notch filter removed and the monochromator set to the excitation wavelength. All decay curves and instrument response functions were background subtracted to remove the ring caused by scope triggering. The pulse was inverted, then the absolute value was taken to reflect any negative-going noise points. The absolute value

operation was necessary because the fitting software is primarily designed for time correlated single photon counting (TCSPC) data and does not accept negative data points. The profiles were then normalized to a peak value of 10^4 , as required for deconvolution. Lifetime data were extracted via iterative reconvolution with the IRF using a commercial software package (Fluofit, Picoquant GMBH). Fits were performed over the first 20ns of the decays in order to avoid a signal reflection occurring at ~21ns due to impedance mismatch. No combination of terminations was able to remove this ring, so it was simply moved to long times by using a 1.75m cable. Because of the complexity of assuring reasonable fits of our analog data with additional lifetime parameters and because we are simply interested in distinguishing bacteria via their time-resolved fluorescence, decays were fit to a 2-exponential model:

$$I(t) = \int_{-\infty}^t IRF(t') \sum_{i=1}^n A_i e^{-\frac{t-t'}{\tau_i}} dt' \quad (2-2)$$

where $I(t)$ is the measured decay profile, $n=2$, IRF is the measured scatter decay profile and A_i and τ_i are the fitting parameters. This model represents a compromise between the reproducibility of fits and the flexibility of the model to represent the behavior of the various decays. Three separate sets of samples were measured over a period of three months in order to better understand the uncertainties. In addition, the uncertainty in fitting was studied as a function of signal shot noise in single shot acquisitions with a single culture of *M. luteus* in order to evaluate the applicability of this method to small samples where S/N will limit lifetime uncertainty. The S/N was varied by changing the excitation energy of the single shot. As the laser pulse energy was varied between one and $8.5\mu\text{J}$, the PMT voltage was varied between 2600 and 2900V as necessary to keep

the single-shot signal on scale. This empirical exploration of S/N and uncertainty was supplemented with a simulation-based experiment to better interpret the results.

Results

Emission Spectra

The fluorescence spectra of suspensions revealed bacterial fluorescence emission maxima at approximately 320nm. (Figure 2-4) Since the spectra were taken with the 532nm notch filter removed, they also showed strong geometric particle scattering at 266nm, which was not quite baseline resolved at the spectral bandpass of the monochromator, as well as a strong water Raman peak at 295nm, which appeared as a barely visible shoulder in some of the weaker fluorescence spectra. These scattering phenomena were easily distinguished by watching the oscilloscope traces during spectral scanning, as in the emission spectrum of ethanol seen in Figure 2-5. The bacterial fluorescence showed an apparent FWHM of approximately 50nm, indicating a slight convolution with the 10nm instrumental bandpass. The emission spectra seen in Figure 2-6 were fairly similar for two of the five bacterial samples (*M. luteus* and *E. coli*). However, the *B. subtilis*, *L. lactis* and *S. epidermis* samples showed emission maxima that were broadened to the blue to varying degrees. Other investigators have noted this feature in *B. subtilis*.⁴⁵ Scans at higher resolution (data not shown) confirmed that this observation is not an artifact caused by variable relative contamination by the 3500cm^{-1} water Raman peak.

E. coli gave the highest signals of the bacteria. The Bermuda grass pollen gave the highest signal of the allergen samples and showed an emission maximum that was shifted to slightly longer wavelengths (335nm) relative to the other samples. The two smuts gave minimal signal, resulting in poor S/N ratios in both the integrated and time-

resolved data. All three samples from Greer Laboratories showed evidence of additional emission peaks at approximately 350 and 420nm. (see Figure 2-4) It was assumed that these peaks were the result of the supplier's sample processing, so further experiments with the allergen samples were suspended.

Time-Resolved Fluorescence

Method performance

The ability of our current setup to resolve sub-nanosecond decay times was demonstrated by measuring lifetimes of unbuffered aqueous tryptophan at 320nm. We found values of τ_1 , τ_2 , and the ratio of the preexponential factors to be 2.8ns, 0.45ns, and 1.7, respectively. Szabo and Rayner¹⁷ reported similar values of 3.17ns, 0.67ns, and 1.5 with 280nm excitation. Similar measurements with tyrosine at 300nm showed a single lifetime of 3.30ns, in good agreement with the literature value of 3.27ns.¹⁸ Though we attempted to use free tryptophan as a standard to evaluate the stability of our experimental setup from day to day, we found that solutions were too unstable, and would decompose even after a few minutes on the benchtop. Because of the high number densities used in our experiments, the lifetime of *E. coli* (at 330nm emission) was measured at optical densities of 0.4, 0.3, and 0.2 to check for artifacts caused by optical trapping or photon diffusion. The results (not shown) showed identical decays at the three number densities. A sample of *E. coli* in a was also irradiated with 8000 shots (12mJ) at 266nm with comparison of the pre and post-irradiation decays to verify the absence of photobleaching artifacts (data not shown) in the course of data acquisition in the stirred cuvettes.

Bacterial lifetimes

Lifetime decays were examined visually before fitting. The signal to noise ratios of the decays from the edges of the fluorescence emission profiles were lower than those near the emission maximum, as would be expected. At shorter emission wavelengths, the decays generally resolved into two groups, with *E. coli* and *L. lactis* decaying in the longer decay group and *S. epidermis*, *B. subtilis* and *M. luteus* decaying with shorter lifetimes (see Figure 2-8). In the shorter lifetime group, *B. subtilis* tended to be the fastest decaying, though the curve was not highly resolved from the other decays (inset of Figure 2-8). In the intermediate 330-350nm range, *S. epidermis* may be visually resolvable from the other two fast-decaying bacteria (Figure 2-8).

Beyond 400nm, *L. lactis* showed a significantly longer lifetime than the other organisms. (Figure 2-8) *S. epidermis*, *M. luteus* and *B. subtilis* showed markedly faster decays, but were fairly unresolved from each other. *E. coli* demonstrated an intermediate lifetime at this wavelength and was well resolved from both the fast-decaying group and the slower-decaying *L. lactis*.

In fitting the bacterial decays, the “best” model (one exponential, two exponential, etc.) seemed to vary with organism and wavelength. To simplify procedures, the two-exponential model was selected, since all decays show at least two strong lifetime components with evidence of a lesser contribution from a third component in some cases. The lifetime data is presented as the true average lifetime (τ_{av} , intensity averaged lifetime), which weights the different lifetimes according to their contribution to the total time-integrated fluorescence (τ_{av}) where τ_i and A_i are the lifetime and preexponential factor of the *i*th lifetime component:

$$\tau_{av} = \frac{A_1\tau_1^2 + A_2\tau_2^2}{A_1\tau_1 + A_2\tau_2} \quad (2-3)$$

The wavelength resolved intensity averaged lifetimes are presented in Figure 2-9. The 290nm and 300nm fluorescence decays contain a significant amount of Raman scatter from water in addition to bacterial fluorescence. As a result, the fits at the two shortest wavelengths are probably of questionable quality in spite of the fact that the software subtracts out a portion of the instrumental function from the fluorescence decay during the fitting process in order to correct for excitation light scatter. The average lifetime approaches a maximum around 410nm for all of the organisms but *L. lactis*, whose fluorescence lifetime increases with wavelength across the whole measurement range. The plot reflects the general observations made from visual inspection of the decay profiles- shorter wavelength decays generally resolve into at least two groups- *E. coli*/*L. lactis* and *S. epidermis*/*B. subtilis*/*M. luteus*, with *B. subtilis* being the fastest decaying. At longer wavelengths, *L. lactis* shows a distinctly longer lifetime, while *S. epidermis*, *M. luteus* and *B. subtilis* form an unresolved group. The maximum and minimum lifetimes between species are within one nanosecond of each other at almost all wavelengths. The fits of the *M. luteus* decays at seven different single shot energies (Figures 2-10 and 2-11) showed standard deviations ranging from 0.35-1ns in three separate determinations at each energy, significantly larger than the total month-to-month variation in the fitted lifetimes from repeated excitations. (Fig. 2-12)

Discussion

The fluorescence spectra alone allow visual classification of the bacteria into two groups by the peak shape below 325nm: SE+BS vs. LL+ML+EC. We have not

calculated any measure of the difference, however, as the main thrust of this investigation is lifetime measurements. Although the total range of lifetimes at each wavelength is small, the average of the lifetimes can be resolved at a minimum of one wavelength for each of the three bacteria studied due to the surprisingly small inter-month standard deviations. In most cases, however, the difference is still very slight relative to the uncertainties, LL being an exception at long emission wavelengths.

In single particle, or single-particle-single-shot situations applicable to bioaerosols, the S/N is likely to be less than that seen in Figure 2-8. In examining Figure 2-11, however, there is no clear trend in the uncertainty with S/N. By definition, the shot noise limited S/N improves by a factor of 2.9 between 1 and 8.5 μ J of excitation (assuming that the signal is not saturated), but there is no apparent decrease in uncertainty within this modest range. As a reference, consider that each shot in Figures 2-9 and 2-10 interrogates $\sim 10^7$ bacteria.

In order to further evaluate the feasibility of distinguishing single bacteria by their wavelength-resolved fluorescence decays, a clearer understanding of the relationship between fitting uncertainty and signal is needed. As has been mentioned, the signal to noise ratio decreases as the emission decays within a single time-resolved profile. The MCP PMT is operated at a high enough voltage that measurements are signal shot noise limited. In fitting the experimental curves with Fluofit, there are two options for weighting the residuals to determine the minimum in the iterative reconvolution process. The standard weighting assumes a Poisson distribution, and is used for TCSPC. Otherwise, the publishers suggest using the software's uniform weighting option, as there is no generally accepted noise distribution model for non-TCSPC data.⁴⁶

In general, the experimental uncertainty in bacterial lifetimes is approximately 0.6ns (Figure 2-12) across much of the spectrum, increasing slightly at the longer wavelengths. This is likely because the peak fluorescence signal was kept approximately equal across much of the spectrum by attenuating the excitation laser pulse. At longer and shorter wavelengths, the signal dropped off, even when the maximum specified excitation energy was employed, leading to decreased quality in the lifetime fits and increased uncertainty.

In order to determine the applicability of fluorescence lifetime measurements to online screening of aerosol particles, a computer program was written in Labview to generate random photons with an average probability distribution curve corresponding to the exponential decay of powerchip-induced fluorescence. These curves were then used in a pseudo-bootstrap error analysis. The software (Figure 2-13) downloads an instrumental response function (i.e. the time-resolved 266nm scatter signal) from the oscilloscope then convolves the IRF with a user-configurable biexponential decay. The resulting convolved function becomes the **Probability Distribution Function**. The probability distribution is then summed and normalized to unity to generate a **Cumulative probability Distribution Function** according to:

$$\mathbf{CDF}(x) = \frac{\int_0^x \mathbf{PDF}(x)dx}{\int_0^{\infty} \mathbf{PDF}(x)dx} \quad (2-4)$$

The built-in Labview random number generator is then used to produce a random number between 0 and 1. This value is located on the probability axis of the cumulative probability distribution function (ordinate), and the photon arrival time read from the

abscissa. This event arrival time is added to a histogram of arrival times (i.e. a TCSPC plot). The random number generation is repeated until the desired number of virtual photons has been histogrammed.

Fifteen histograms were generated for each point (i.e. for each integral number of photons). Each histogram was exported to Fluofit and fit to a biexponential decay via iterative deconvolution. The preexponentials and lifetimes were used to calculate the intensity averaged lifetime (τ_{av}). Standard deviations were determined from the 15 τ_{av} values, and are graphed in Figure 2-14. In instances where the reconvolution software settled on nonsensical decay parameters (i.e. two preexponentials with indistinguishable decays or negative preexponentials), the individual decay was refit with slightly constrained parameters or the point was excluded. These fits produced a tell-tale residuals distribution, and were easily spotted.

Because convolution is associative, convolving with the fluorescence decay law after convolving the laser profile with the PMT and oscilloscope response should be equivalent to the experimental situation where the effective order of operations is different. It should be kept in mind, however, that the synthetic data is essentially time correlated single photon counting data (i.e. it is digital). The experimentally measured decays do not necessarily have the same signal to noise characteristic at all points in the decay- i.e. the noise may not be governed by Poisson statistics. Additionally, the synthetic data was generated with a time interval resolution (50ps) that exceeded the analog resolution of the PMT (~500ps), which may not be entirely comparable to the experimental situation. In order to check the effect of reduced resolution on the

uncertainty, decay curve points were binned (in groups of 3 or 5) within a curve and additional fits were generated.

In general, the uncertainties from unbinned fits show an approximately $n^{-1/2}$ dependence on the total number of photons in the fitted curves (i.e. slopes of log-log curves were approximately -0.5). The effect of binning is not as clear, as it improves uncertainty in one case, and degrades it in the other. The experimental bacterial decays summarized in Figure 2-9 display uncertainties in the vicinity of ~0.06ns. This level of uncertainty is achieved in the synthetic data (Figure 2-14) when the number of photons in the TCSPC curve is on the order of 3×10^5 photons. A less robust criterion, the uncertainty required to distinguish *E. coli*/*L. lactis* from *S. epidermis*/*B. subtilis* at 370nm (0.4ns) is achieved with more than an order of magnitude fewer photons ($\sim 8 \times 10^3$).

Although fluorescence cross sections were not measured in this work, fluorescence cross sections for spores and vegetative cells have been reported in the literature.⁴⁷ The excitation fluence (J/cm^2) required to give a specified number of photons, i_{ph} from a single bacterial cell is given by the equation:

$$F = \frac{i_{ph} \cdot h \cdot c \cdot \Delta\lambda_{em}}{\sigma_{\Omega} \cdot \lambda_{ex} \cdot s_g \cdot \Omega \cdot \eta_d} \quad (2-5)$$

where h is Planck's constant, c is the speed of light (nm/s), $\Delta\lambda_{em}$ is the fluorescence peak width (nm), λ_{ex} is the excitation wavelength (nm), σ_{Ω} is the fluorescence cross section ($\text{cm}^2/\text{cell} \cdot \text{sr}$), s_g is the monochromator/filter bandpass (nm), Ω is the solid angle of collection and η_d is the dimensionless detection efficiency. This equation assumes a simplified square emission profile-- clearly, the optical demands would be greater at the edges of the emission profile.

Assuming $i_{ph}=3.7 \times 10^5$, $\Delta\lambda_{em}=50\text{nm}$, $s_g=10\text{nm}$, $\Omega = \pi$ steradians and $\eta=0.3$, and taking Sivaprakasam's value^{47a} for the fluorescence cross section of *Micrococcus luteus* ($4 \times 10^{-12}\text{cm}^2/\text{sr} \cdot \text{cell}$), an excitation fluence of $3.6 \times 10^{-1}\text{J}/\text{cm}^2$ is required to provide a $\sim 0.06\text{ns}$ uncertainty in the intensity averaged lifetime (Table 2-2). If this fluence is delivered in a single powerchip laser pulse, the cell experiences an irradiance of $7 \times 10^8\text{W}/\text{cm}^2$. Thus, fast pulsed excitation has the disadvantage of possible nonlinearities at high irradiance, and even laser breakdown as irradiance approaches GW/cm^2 . Although the calculated irradiance is an order of magnitude below the breakdown threshold, the fluorescence cross section and the detector solid angle and optoelectronic efficiency are fairly optimistic. Thus, the required irradiance may be even closer to the breakdown threshold. Furthermore, the uncertainty provided at this signal level would only distinguish relatively distinct pairs of decays. More subtlety (and higher irradiance) would be required to make the technique useful.

Based on the 266nm pulse energy of the laser used in this study ($8\mu\text{J}$), a laser spot diameter of $52\mu\text{m}$ is required to extract adequate fluorescence from a single excitation for a 0.06ns uncertainty. Assuming a beam radius of one millimeter at the laser output, this beam waist is achievable with a focal length of 0.3 m, allowing a Raleigh range of $\sim 0.8\text{cm}$, and even the possibility multiple laser-particle interactions if the beam is counter-propagating with the particle trajectory. Assuming a particle speed of $0.2\text{m}/\text{s}$ (i.e. low-speed operation of the inlet), the particle could experience as many as 80 laser shots before exiting the 1.6cm-long Raleigh region. This, however, requires an oscilloscope that triggers at the full laser repetition rate. A more likely limitation to the residence time and, therefore, the photons collected is the volume of the collection

optic focus and/or the length of the MCP PMT photocathode. Additionally, a beam waist diameter of $\sim 50\mu\text{m}$ would necessitate low particle beam divergence.

It should be kept in mind that the above parameters were calculated so as to give a modest lifetime uncertainty of 0.06ns. Far less uncertainty would be required to allow adequate discrimination among the infinite number of possible fluorescent particles.

Additional assumptions include:

- 1) linearity of the signal of all the fluorophores contributing to the decay profile
- 2) isotropic fluorescence emission
- 3) that oscilloscope trace fitting uncertainty is well approximated with TCSPC data
- 4) absence of photobleaching at high laser irradiance and/or exposure
- 5) low variation in intra-culture fluorescence lifetime (i.e. that all cells in a culture display the same fluorescence lifetime)

Assumption 5 results from the fact that measured uncertainties up to this point have been uncertainties in large samples (i.e. each cuvette contains $\sim 10^9$ bacteria). There is likely to be variation within that population that further complicates assigning a single cell to a category based on its fluorescence emission. In an effort to address assumption five, we have evaluated several setups for generating single-bacterium data. To date, these measurements have been stymied by the short excitation wavelength.

In the first attempt to characterize single-cell fluorescence, an electrodynamic balance based on the design of Davis et al.⁴⁸ was built and successfully trapped particles less than $10\mu\text{m}$ in diameter. Unfortunately, the 266nm excitation used in this work proved energetic enough to photoionize particles, which were subsequently lost

from the trap. Subsequently, a fluorescence microscope was constructed around a Thorlabs cage setup and a reflecting microscope objective in order to make measurements from single particles in aqueous suspension. In this case, measurements were hampered by the background fluorescence of the optics train. At such short excitation wavelengths, background fluorescence is a significant issue. For instance, the highest grade fused silica (UV-S1, Esco Products, Oak Ridge, NJ) microscope slides and cover slips were required, and these were cleaned in concentrated nitric acid between uses. Even this high-grade fused silica can develop color centers that contribute emission under the high irradiance necessary to generate adequate signal from small sample volumes. Attempts were made to subtract out a background signal from time-resolved and spectrally resolved data, but the variability of the laser scatter and the resulting fluorescence made this difficult. As a corollary to the fifth assumption, an understanding of the variability of fluorescence lifetime with various microbiological parameters is required. Factors such as bacterial growth medium, metabolic state, and growth stage may affect fluorescence, as might contamination from concomitant non-bacterial fluorophores on the bacterial particles.

These initial explorations of time-resolved bacterial fluorescence do indicate a limited potential for the use of fluorescence to generate at least some level of discrimination among bacteria. In order to differentiate bacteria of different species from each other, as well as from potential confounding contaminants, an extremely high selectivity is required. This study has been performed as a preliminary “sorting” problem, with only a few species. Even still, the S/N ratio for single bacteria may be too low to measure the slight differences between bacterial lifetimes in a single probing of a

single cell. Thus, it seems unlikely that the technique would be appropriate for bioaerosol identification. Multiple probings in order to increase signal to noise would be necessary if there is any chance of success- i.e. a high repetition rate laser coupled with a fast, high trigger rate data recorder, such as a streak camera. In fact, a streak camera would be ideal for this measurement as they provide parallel time and wavelength resolution when coupled to a spectrograph. These, however, would be difficult to couple to an aerosol system as the light is delivered to the spectrometer via a single optical fiber, or as a point source.

Additionally, the robustness of the population differences and the photophysics of the measurement itself need investigation. Multiple probings to improve signal to noise from a single particle may be useless if the excitation changes the molecular structure of the fluorophores after the first shot. This is not unlikely, given the short wavelength of the excitation wavelength. As in most fluorescence measurements, the short wavelength excitation used here reduces the selectivity of the technique and increases the demands on the materials used in the optics.

Table 2-1. Fluorescence parameters of selected bacterial fluorophores

Fluorophore	Excitation maxima (nm)	Emission maxima (nm)	Lifetime (ns)	Reference for lifetime	
Tryptophan		280	350	3.1, 0.53	17
NATA				3.00	17
Tyrosine	275		300	3.27	18
NATyrA				1.66, 0.11	18
Phenylalanine	260		280		
FAD, flavins	450		535	3→5	29
NADH	290, 351	440, 460		0.4, >1ns	21
NADPH		336	464		
Pterins	275, 360		440	2-8	49

[Adapted from Ammor, M. S. *Journal of Fluorescence* **2007**, 17, 455-459.]

Table 2-2. Optical parameters calculated for different experimental uncertainties

Uncertainty	0.4ns	0.06ns
Photons	7.9E+03	3.7E+05
Fluence (J/cm ²)	7.8E-03	3.6E-01
Irradiance (W/cm ²)	1.6E+07	7.3E+08
Radius required (μm)	1.8E+02	2.6E+01
Focal length required (m)	2.1E+00	3.1E-01
Rayleigh range (m)	3.9E-01	8.3E-03

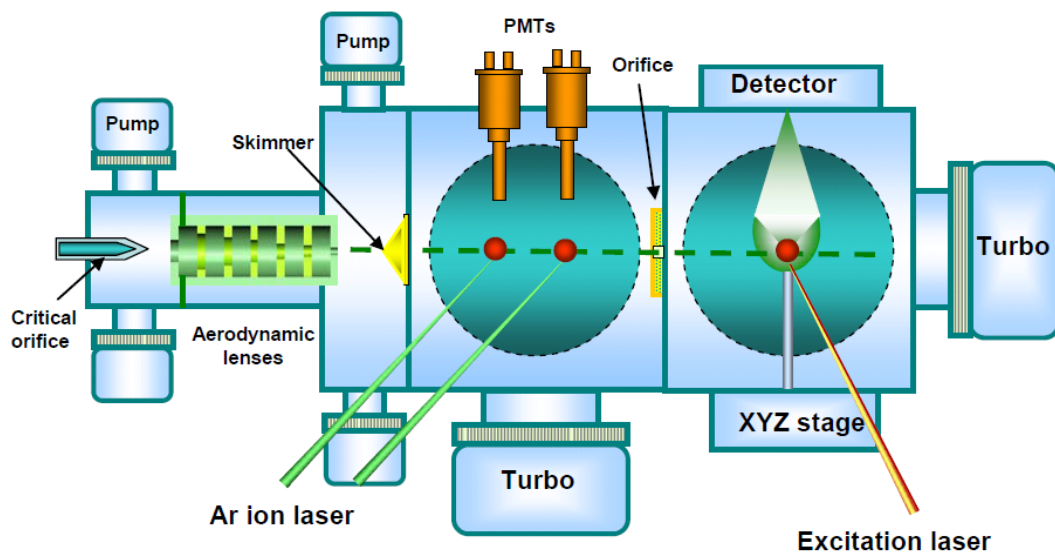


Figure 2-1. Schematic of aerosol instrument. [Figure reproduced from Wu, X.; Merten, J. A.; Omenetto, N.; Smith, B. W.; Winefordner, J. D. *Laser Chemistry* **2009**, *2009*, 14.]

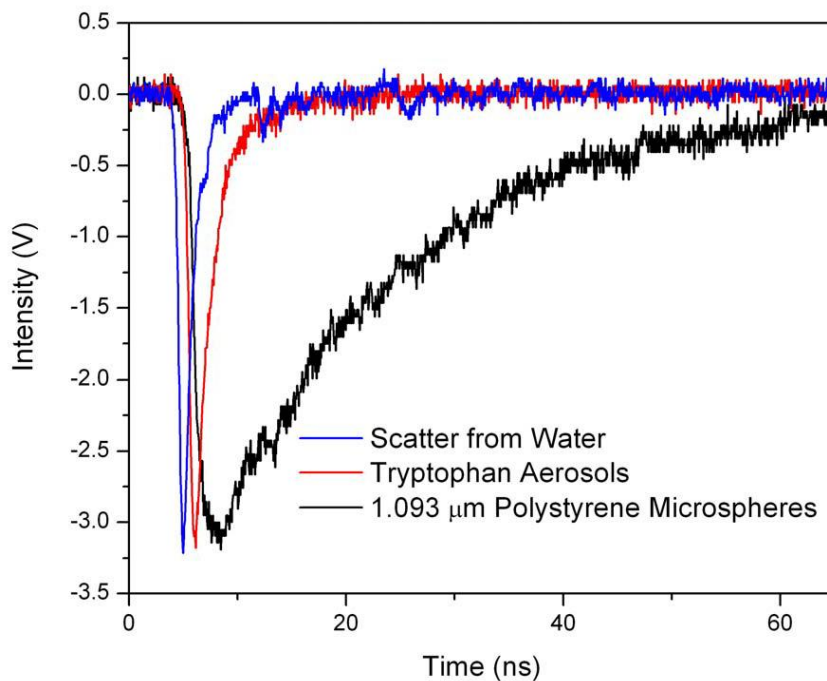


Figure 2-2. Single shot decay profiles of aerosols in aerosol instrument. Excitation is by ~3ns 337nm nitrogen laser. [Figure reproduced from Wu, X.; Merten, J. A.; Omenetto, N.; Smith, B. W.; Winefordner, J. D., Development, Characterization, and Application of a Versatile Single Particle Detection Apparatus for Time-Integrated and Time-Resolved Fluorescence Measurements—Part II: Experimental Evaluation. *Laser Chemistry* **2009**, *2009*, 14.]

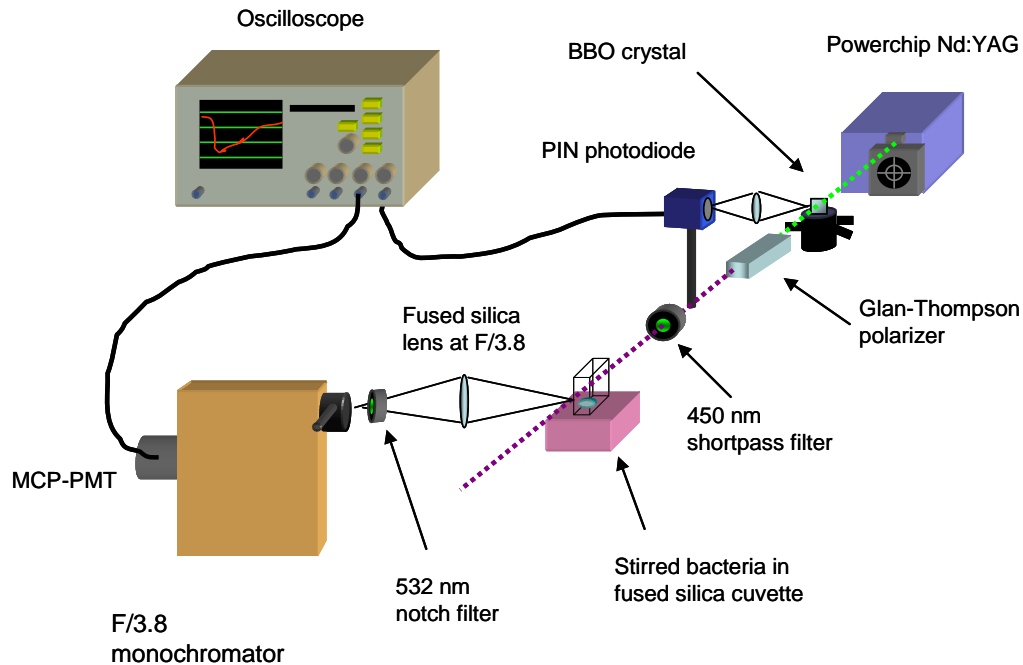


Figure 2-3. Benchtop fluorescence setup schematic.

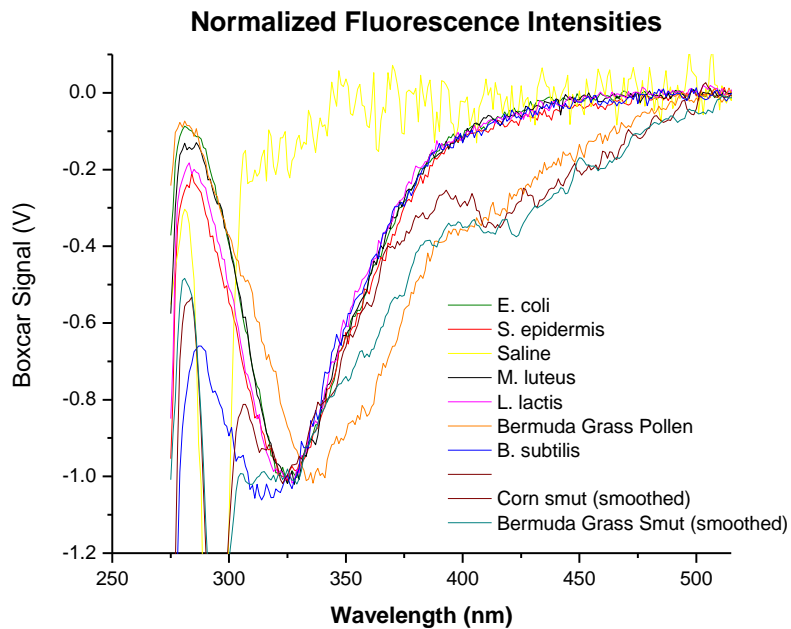


Figure 2-4. Normalized fluorescence spectra of bacteria and allergens under 266nm excitation. Detection via boxcar and MCP-PMT.

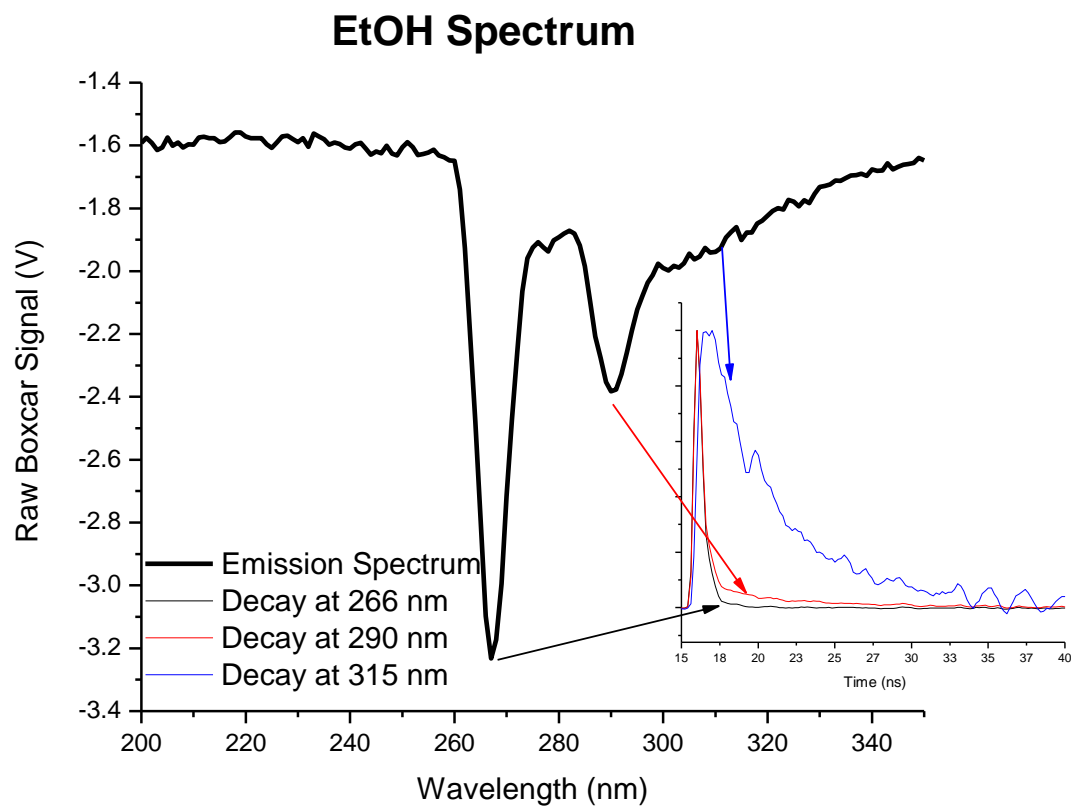


Figure 2-5. Ethanol emission spectrum. Inset shows normalized time-resolved decay profiles at indicated spectral regions.

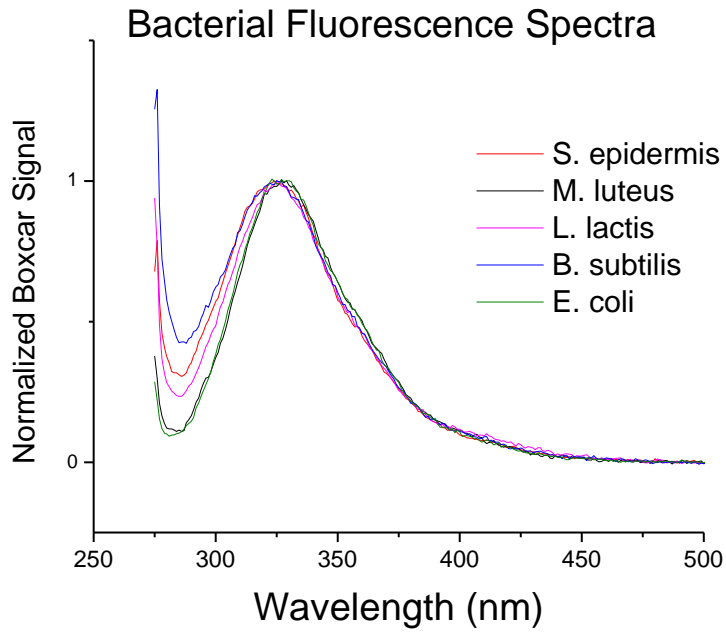


Figure 2-6. Normalized bacterial fluorescence.

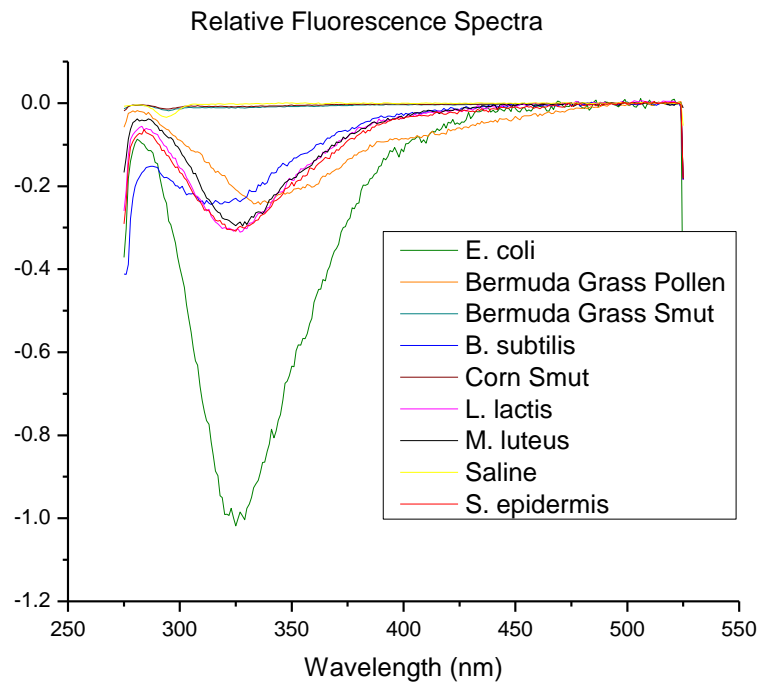


Figure 2-7. Fluorescence spectra scaled to indicate relative intensities.

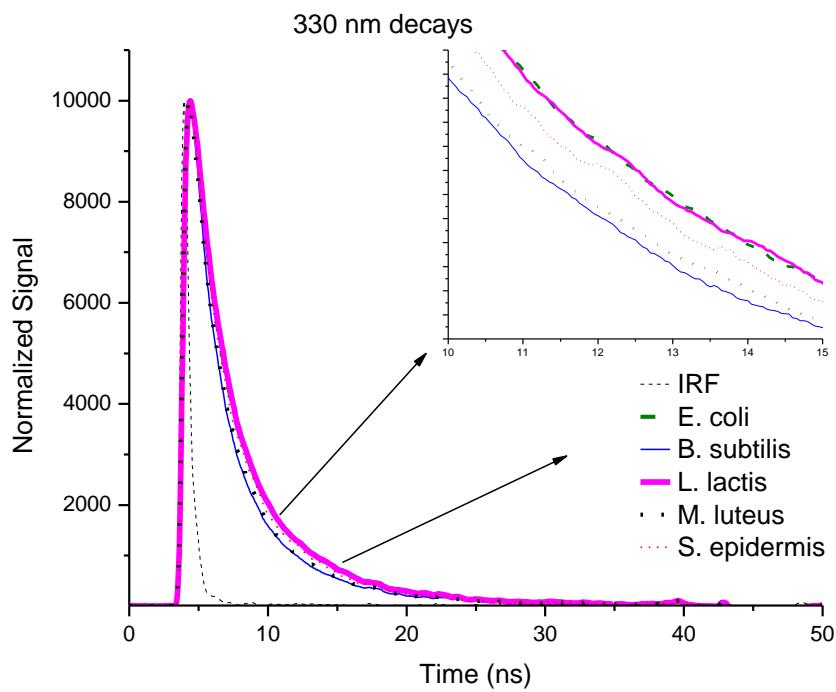
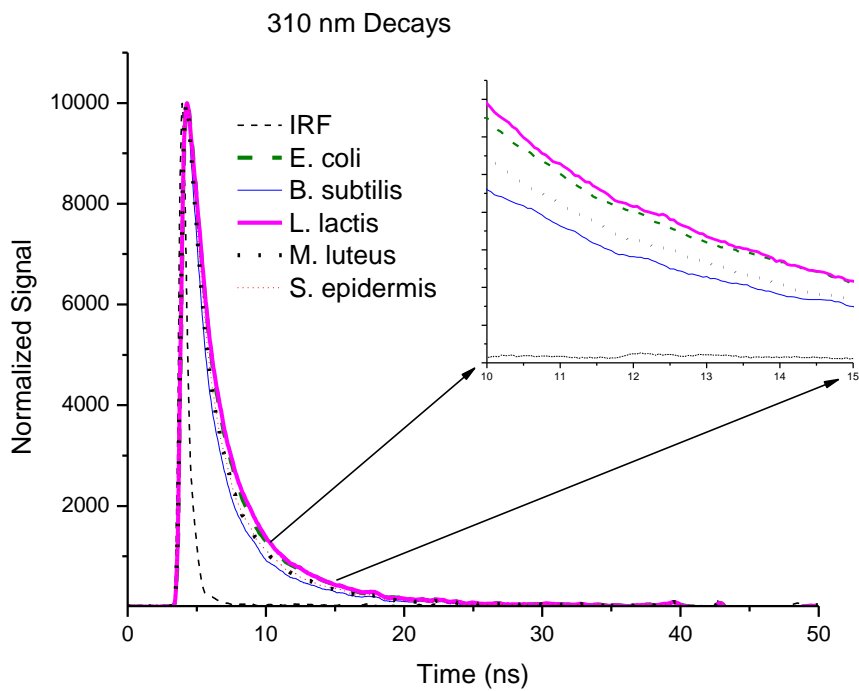


Figure 2-8. Selected wavelength-resolved fluorescence decay profiles.

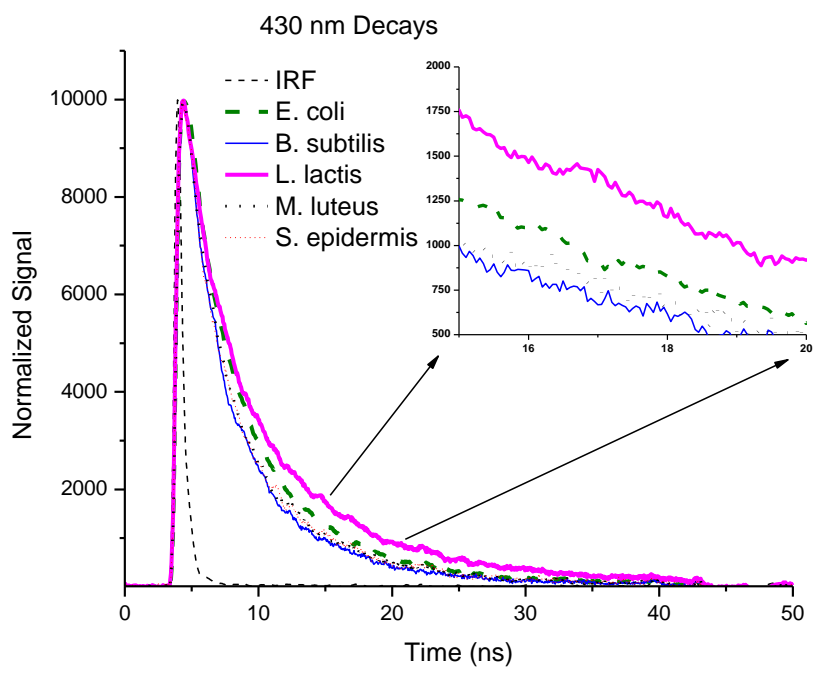


Figure 2-8. Continued.

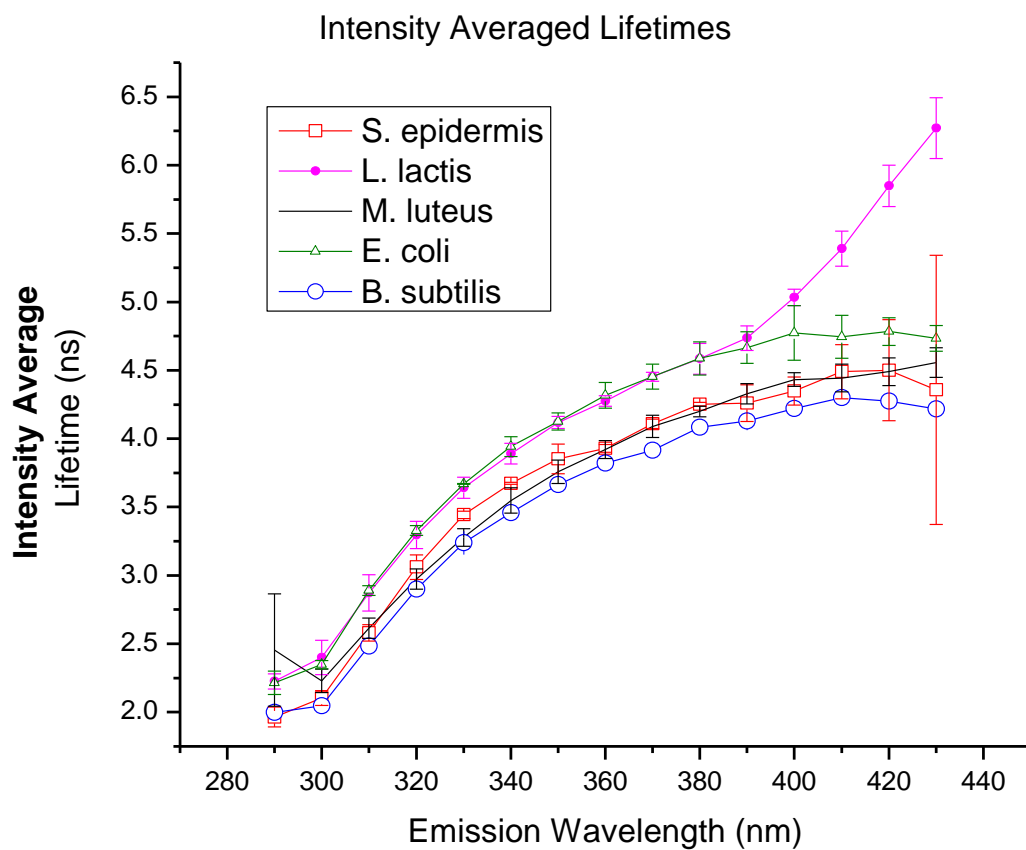


Figure 2-9. Intensity averaged lifetimes of bacteria. Error bars are \pm one standard deviation of $n=3$.

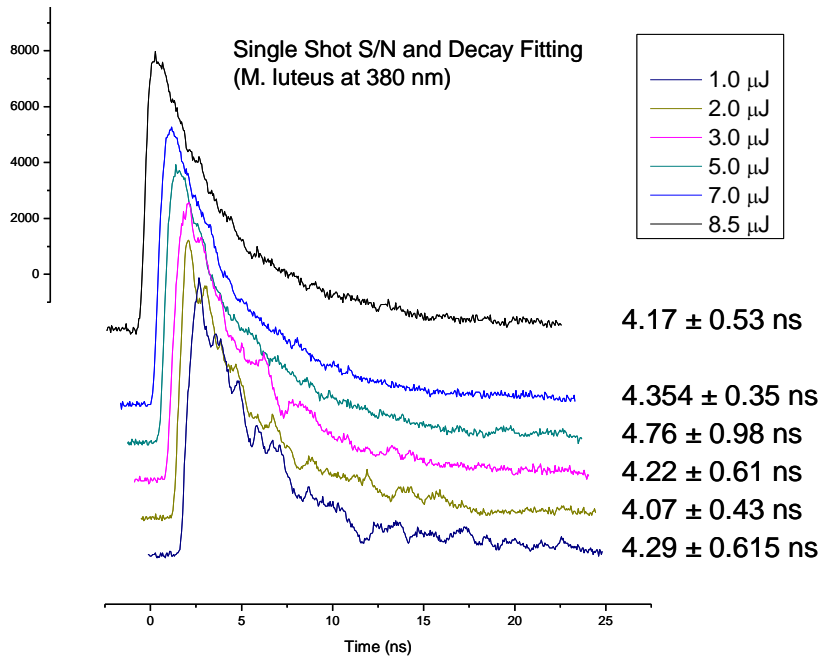


Figure 2-10. Representative decay profiles and lifetime uncertainties at different single-shot S/N ratios. Note that the true lifetime of this sample was determined to be 4.12ns.

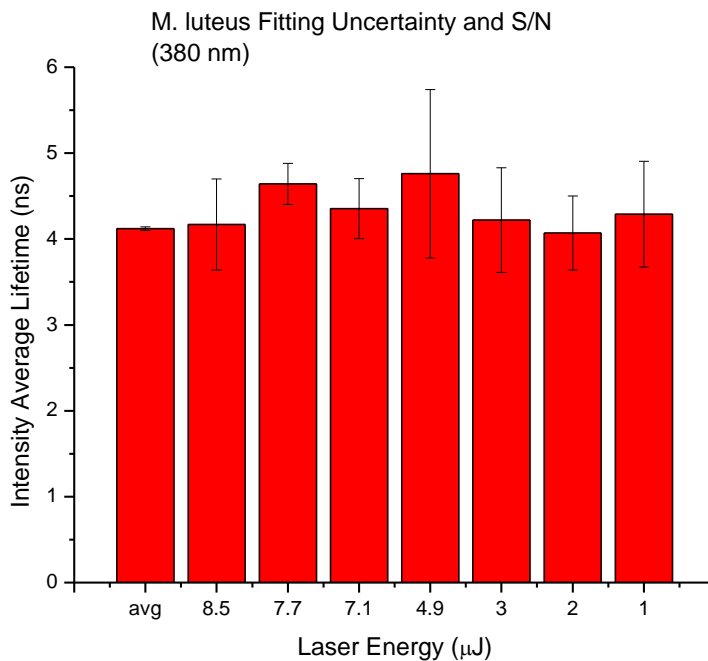


Figure 2-11. Effect of shot noise on lifetime fits. In this study, signal is proportional to laser energy, while SNR is proportional to the square root of the laser energy.

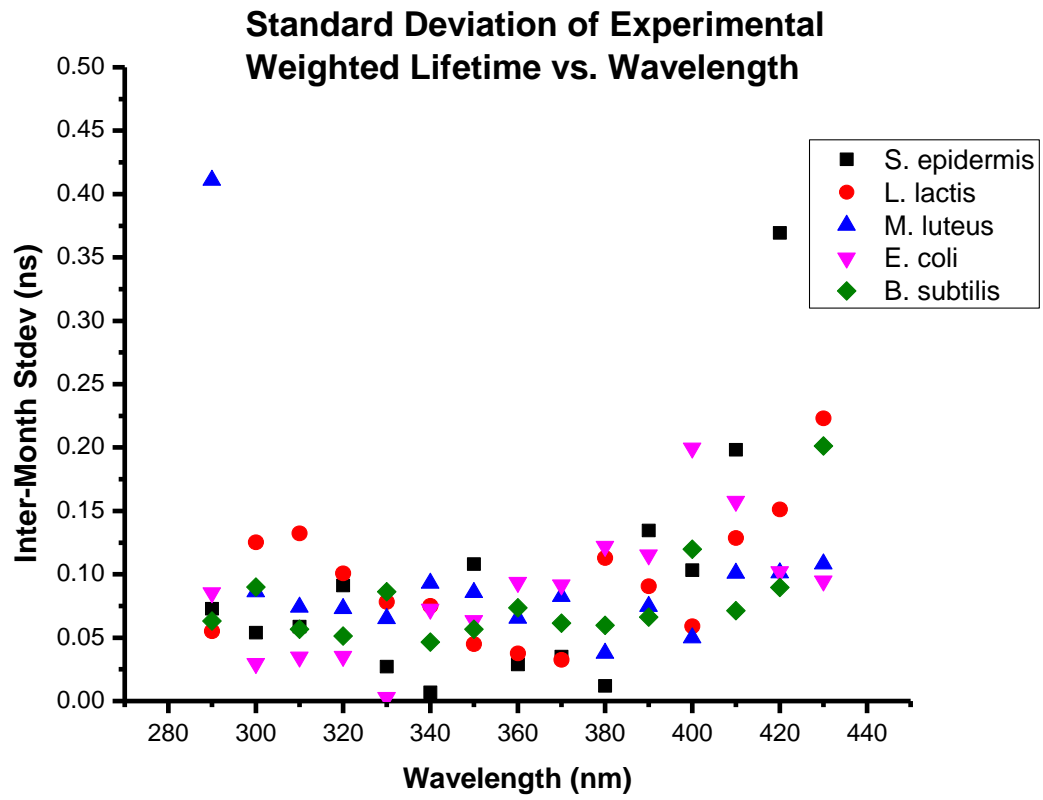


Figure 2-12. Lifetime standard deviation vs. wavelength for all species studied.

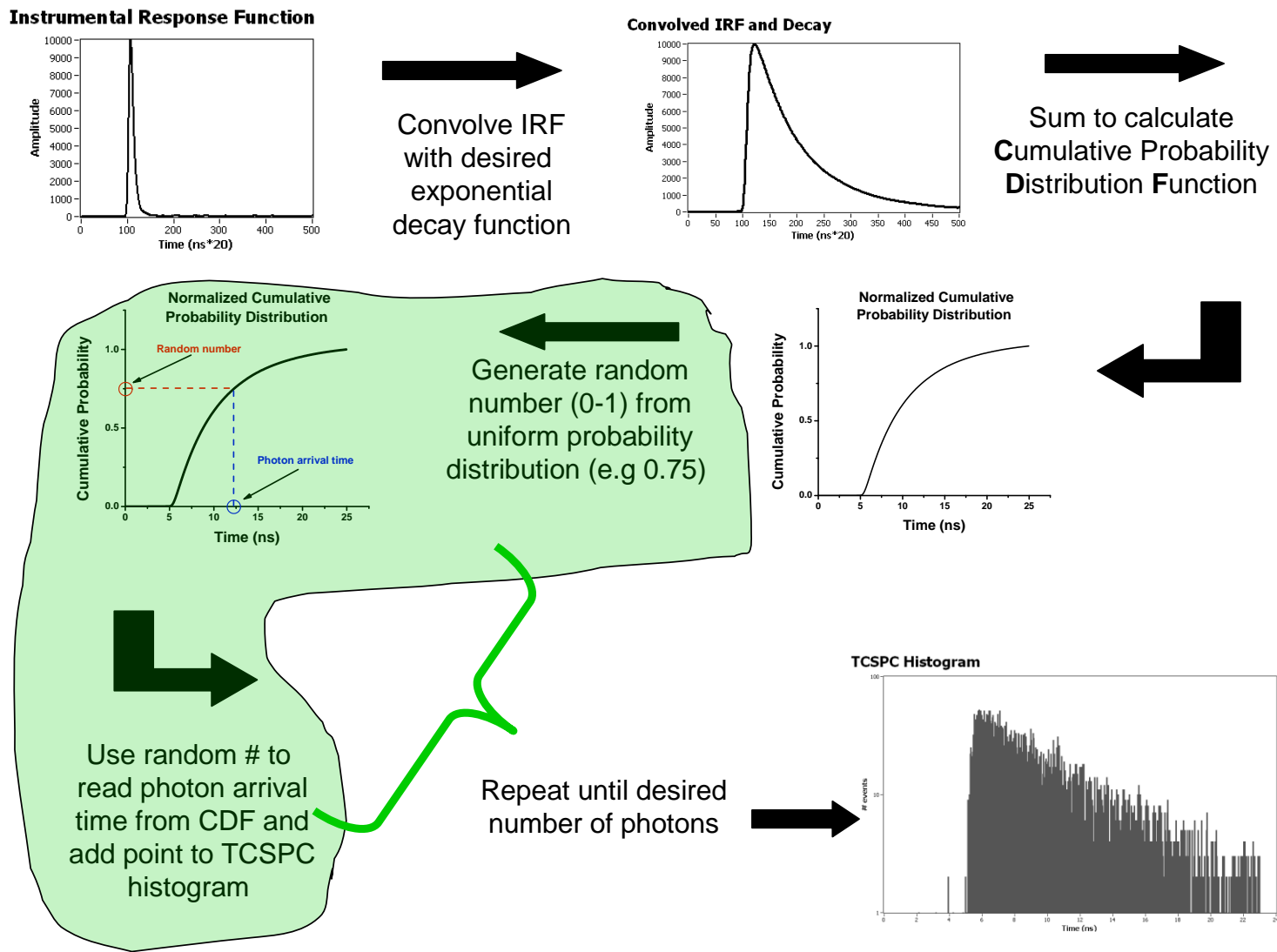


Figure 2-13. Algorithm for generating synthetic decay profiles.

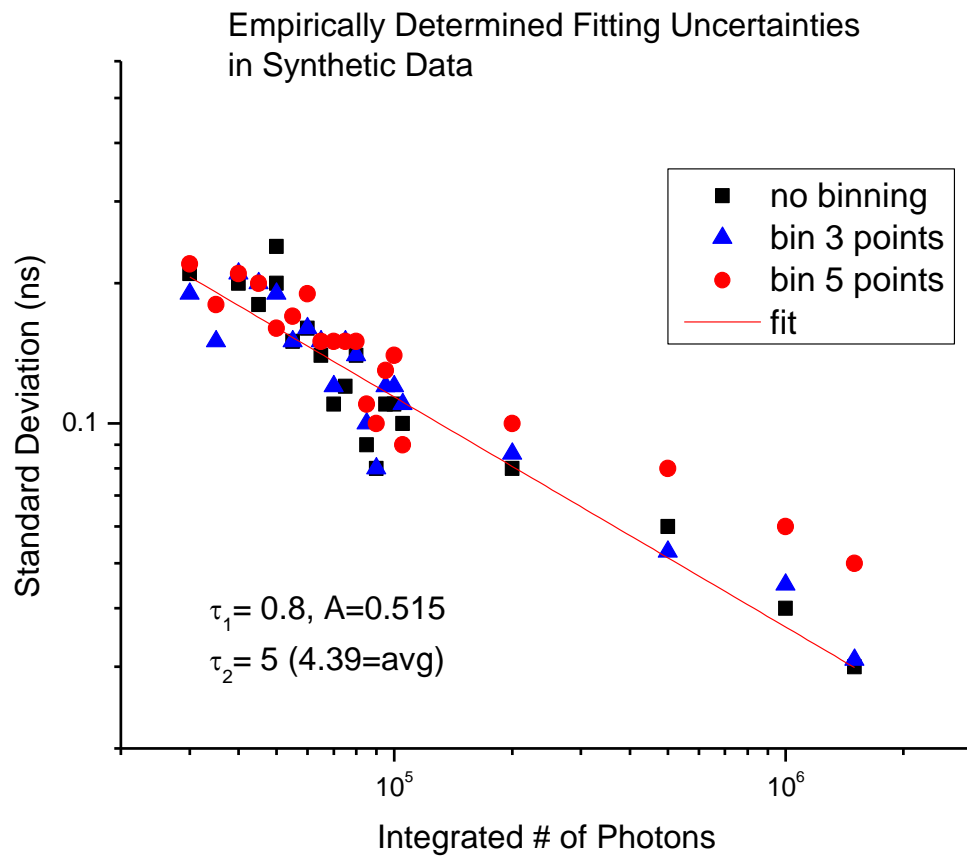


Figure 2-14. Uncertainties in fitting synthetic decays as a function of number of integrated photons.

CHAPTER 3 LASER INDUCED BREAKDOWN SPECTROSCOPY

Basics

The previous chapter evaluated time-resolved, powerchip-induced fluorescence for the identification of bioaerosols. The remainder of this dissertation focuses on powerchip LIBS, specifically diagnostics of the spatially and temporally evolving microplasma and the reproducibility of the breakdown process, measurements that have not been performed until now due to the timing jitter of the powerchip laser. The laser is also evaluated for applications in time resolved LIBS microanalysis.

LIBS has been known since Brech first reported on “Optical Microemission Stimulated by a Ruby Maser” at X CSI in 1962.⁵⁰ The recent interest in LIBS, however resulted from an improvement in laser technology and the introduction of the intensified charge coupled device (ICCD). The ICCD allowed the time-discrimination required to bring background noise to an acceptable level, as will be discussed. It also allowed access to the parallel nature of thermal emission spectroscopy that is one of the oft-quoted advantages of LIBS. Ideally, the technique combines sampling and excitation into a single, time-resolvable step. Many challenges remain, however, if LIBS is to become a routine quantitative technique.

Plasma Formation

The initiation of the laser plasma has seen extensive research for material processing, fusion research and analytical applications. Although much effort has been put into reducing matrix effects, the initiation of a LIBS plasma is very much a function of the sample, the wavelength of the laser, the laser fluence (J/cm^2) and the peak

irradiance (W/cm²). Impurities and substrate inhomogeneities play a significant role in the production of the initial seed electrons and plasma initiation.⁵¹

The formation of free (or conduction-band) electrons is necessary for plasma ignition and heating. The high laser irradiance may induce these by cascade ionization or multiphoton ionization. Cascade ionization begins with three-body absorption of photons by seed electrons as they impact with neutrals (inverse bremsstrahlung).

Russo⁵² and Root⁵³ give the inverse bremsstrahlung absorption coefficient, α_{IB} , as:

$$\alpha_{IB} = \left[Qn_e N_0 + \frac{4e^6 \lambda^3 N_e Z^2 N_i}{3hc^4 m_e} \times \left(\frac{2\pi}{3m_e k_b T_e} \right)^{1/2} \right] \times \left[1 - \exp\left(-\frac{hc}{\lambda k_b T_e} \right) \right] \quad (3-1)$$

where Q is the cross section for photon absorption during a collision, n_e is the electron number density, N_0 is the atomic number density, c is the speed of light, h is Planck's constant, Z is the charge of the ion, k_b is the Boltzmann constant, T_e is the electron temperature, e is the fundamental charge, N_i is the ion number density, m_e is the mass of an electron and λ is the wavelength of the photon. The first term on the right is the electron atom term while the second term is the electron-ion term. Although α_{IB} is initially dominated by the electron-atom term, the electron-ion term takes over once ionization reaches 1%.⁵³ It should be noted that the electron-ion term scales with λ^3 , making this term more important at 1064nm than shorter UV wavelengths. After the electrons gain sufficient energy through inverse bremsstrahlung, they begin to ionize neutrals through impact ionization, increasing the free electron concentration available for further inverse bremsstrahlung and beginning the exponential increase in free electron number density. Modeling of the process is complex as a result of the various energy loss pathways for the electrons.⁵¹

Multiphoton ionization, on the other hand is the simultaneous absorption of multiple photons by a chemical species according to:



where n is the number of photons required to exceed the ionization threshold.

Multiphoton ionization is a nonlinear optical process with a rate that scales with I^n , where I is the irradiance and n is the number of photons. Thus, high irradiances are necessary; Russo⁵² indicates that multiphoton processes do not contribute below $\sim 10^8 \text{W/cm}^2$. Because of the non-linear dependence on irradiance, multiphoton ionization becomes more likely at shorter wavelengths, where n is smaller.

Plasma formation- nanosecond laser pulses

Nanosecond laser ablation is generally a thermal process involving distinct transitions between phases. Non-thermal ablation (multiphoton ionization) can contribute at laser irradiances above 10^8W/cm^2 , however.⁵² Weyl⁵¹ divides the discussion of laser breakdown by substrate: transparent dielectrics, absorbing dielectrics, and metals.

Plasmas formed on solid, non-absorbing dielectrics are seeded by multiphoton excitation of valence electrons. Subsequent avalanche ionization and electron impact heats the substrate, causing vaporization. The inverse bremsstrahlung-induced avalanche continues in the vapor phase.

In absorbing dielectrics, the substrate is heated by the electronically absorbed energy and vaporizes. Superheated vapor may already be partially ionized, or plasma ignition may proceed by subsequent avalanche ionization from seed electrons in the vapor. In metals, the plasma is initiated by heating of conduction band electrons and surface plasmon coupling. Electron-atom and electron-ion collisions distribute energy among the various species and the electron-hole plasma explodes. Because the

duration of laser-substrate interaction is long compared to the thermal conductivity of the sample, melting, boiling and sublimation occur, leading to significant modification of the sample outside of the actual ablation zone. Additionally, the phase changes may allow for fractionation of the sample and departure from stoichiometric ablation.

Plasma formation-femtosecond laser pulse

In femtosecond ablation, the laser-substrate interaction is so brief that thermalization is impossible, given that the laser duration is shorter than the phonon relaxation time of solids. In conductors, the conduction band electrons are heated directly. In semiconductors and dielectrics, single and multiphoton absorption promote electrons to the valence band. Once an electron-hole plasma is formed by promotion of electrons to the conduction band, avalanche ionization sets in, further ionizing and heating the solid. Once enough electrons are removed from the valence bonding levels, coulomb repulsion between the nuclei leads to an explosion of cations from the ionized solid substrate. Femtosecond ablation is not affected by plasma shielding since an absorbing plasma cannot form within the duration of the laser pulse. Because femtosecond ablation is non-thermal, it is expected to be stoichiometric.

Plasma formation- picosecond laser pulse

Picosecond regime pulses show both thermal and non-thermal ablation mechanisms, as phonon relaxation times are on the order of 10^{-10} - 10^{-11} s (see, for example Reference 54). As a result, lattice heating *may* occur faster than any possible diffusion of deposited energy, allowing a degree of non-thermal ablation. Russo points out that plasma shielding is possible in the case of picosecond plasmas, though it is due to absorption by a cover-gas plasma plume rather than the substrate plume, which does not develop within the short duration of the laser pulse.⁵² Because microchip and

powerchip lasers can deliver irradiances on the order of 10^4GW/cm^2 , it is not unreasonable to expect that they may produce substantial multiphoton ionization, though previous work has shown evidence of significant thermal action on the samples.^{15a, 15c}

After plasma initiation, its evolution is similar for most substrates. The nascent plasma continues to absorb energy from the laser pulse, further ionizing and heating. As has been pointed out, the degree of laser absorption in the developing plasma plume can limit the amount of material ablated by longer pulses, as the laser no longer penetrates to the sample surface due to shielding by the absorbing plasma.⁵⁵ The shock wave formed in the ambient gas by the plasma explosion propagates away from the plasma, which continues expanding until collisions with ambient gas damp its progress. Under high laser intensities and long pulse durations, the shock front itself becomes opaque as the high electron and ion number densities increase the inverse bremsstrahlung absorption coefficient. As a result, the plasma plume absorbs laser energy, propagating asymmetrically toward the laser and shielding the sample from further heating and ablation. This effect is expected to be less significant at shorter wavelengths, however (Equation 3-1). Multiphoton absorption, on the other hand, is higher at shorter wavelengths, but the effect is not expected to be significant in most shielding situations. As the plasma cools, ions and electrons recombine (Fig. 3-1). At much later times, atoms recombine to form clusters and molecules, which dissipate over the course of microseconds to milliseconds. The spatial and energetic evolution of the plasma is obviously highly complex.

Plasma spectra are equally complex and time-dependent. Early plasma emission is characterized by bremsstrahlung (free-free transition) and recombination (free-bound) continuum emission. The continuum dominates plasma emission for the first few tens of nanoseconds as indicated in Figure 3-1. Although it contains diagnostic information on the plasma⁵⁶, it contains little analytical information and degrades the S/N ratio of the spectral lines that do carry analytical information about the sample. Initial work in LIBS employed complex mechanical gating with rotating mirrors to gate away from the continuum (see, for example, Reference 57). ICCD's simplify the process by electronically gating the passage of primary photoelectrons between the photocathode and the MCP image intensifier.

Plasma evolution and local thermodynamic equilibrium

Although a kinetic description of LIBS plasmas is desirable because of their fast spatial and temporal evolution, it is complicated by the tremendous number of processes coexisting in the plasma. As a result, many researchers have turned to statistical mechanical equilibrium descriptions to simplify the process of understanding and characterizing the plasma. A plasma in complete thermodynamic equilibrium (TE) can be fully described by a single temperature and three equations (see Reference 58 and the references therein). The Boltzmann distribution describes the electron kinetic energy and the various excitational states of a given species (i.e. an atom or a single ionization state of an atom):

$$N_n = \frac{N}{U(T)} \cdot g_n e^{\frac{-E_n}{kT}} \quad (3-3)$$

where N_n is the number density of a given level, N is the number density of the species, $U(T)$ is the partition function, g_n is the degeneracy of the level, k is the Boltzmann

constant, T is the temperature and E_n is the energy of the level. Similarly, the Saha-Eggert equation describes the equilibrium between the atomic and ionized states:

$$\frac{n_e N_{II}}{N_I} = 2 \frac{U_{II}(T)}{U_I(T)} \left(\frac{m_e kT}{h^2} \right)^{3/2} e^{-(E_\infty - \Delta E)/kT} \quad (3-4)$$

Where N_I and N_{II} are the number densities of the first and second ionization states of the element in the plasma (relevant species in typical LIBS conditions), h is Planck's constant, n_e is the electron number density, m_e is the electron mass, E_∞ is the first ionization energy and ΔE is the plasma perturbation of the ionization energy. Finally, the Planck function governs the density of photon energies ($\text{J} \cdot \text{cm}^{-3} \cdot \text{Hz}^{-1}$):

$$W(\nu) = \frac{8\pi h \nu^3}{c^3 \cdot (e^{h\nu/kT} - 1)} \quad (3-5)$$

where ν is the frequency of the photon (Hz). Complete thermal equilibrium is only possible, however, for a stationary and homogeneous blackbody plasma, where emission and absorption are equal.

With their short lifetimes, intense emission and rapidly expanding plumes, LIBS plasmas are far from stationary, homogeneous, or blackbody. In light of this, researchers fall back on the concept of local thermodynamic equilibrium (LTE) to describe the plasma. LTE relaxes the requirement of complete thermal equilibrium, decoupling the characteristic radiation temperature from the other energetic degrees of freedom with the assumption that the rate of radiation losses is small relative to the total energy of the plasma.⁵⁸ Because the main collision partner in plasmas (due to their high relative velocity) is electrons, the LTE assumption relies on these to dynamically redistribute energy among the various degrees of freedom faster than any radiative transition can depopulate the level. To this end, LTE assumes that the rate of collisions

with adequately energetic electrons (i.e. the electron's kinetic energy is at least equal to the ΔE of the transition) is 10 times faster than the radiative relaxation of an energy level, an assumption generally summarized by the McWhirter criterion:⁵⁹

$$n_e > \frac{2.55 \cdot 10^{11}}{\langle \bar{g} \rangle} T^{1/2} (\Delta E)^3 \quad (3-6)$$

where n_e is the experimentally measured electron number density (cm^{-3}), T is the plasma temperature (K), $\langle \bar{g} \rangle$ is the unitless Gaunt factor and ΔE is the energetic separation of the energy levels under consideration (eV). If the experimental n_e is less than the McWhirter value, the levels under consideration are not in local thermodynamic equilibrium. Because the ground to lowest excited state energy gap is frequently too high (and because these resonance transitions have relatively high coefficients of spontaneous emission⁵⁶) for LTE, partial LTE (pLTE) is sometimes invoked, meaning that pairs of states with some stated maximum ΔE are in LTE with each other. Thus, the McWhirter criterion can be rearranged to define the maximum energy separation across which two levels *may* be in equilibrium within a plasma.

This qualification is important because conformity to the McWhirter criterion only guarantees (partial) LTE for a homogenous, stationary plasma. Cristoforetti et al. point out that two more conditions are necessary for LTE in LIBS plasmas. The additional stipulations arise from the finite time, τ_{rel} , required for electron collisions to redistribute energy after a perturbation:

$$\tau_{rel} \approx \frac{6.3 \cdot 10^4}{n_e f_{nm} \langle \bar{g} \rangle} \Delta E_{mn} (kT_e)^{1/2} e^{\frac{\Delta E_{mn}}{kT_e}} \quad (3-7)$$

where f_{nm} is the transition oscillator strength and the other parameters are as defined above.⁵⁸ To maintain LTE, the relaxation time must be shorter than the time in which the plasma evolves, a condition summarized by Cristoforetti et al.⁵⁸ with the relations:

$$\frac{T(t + \tau_{rel}) - T(t)}{T(t)} \ll 1 \quad (3-8a)$$

$$\frac{n_e(t + \tau_{rel}) - n_e(t)}{n_e(t)} \ll 1 \quad (3-8b)$$

The spatial variation in parameters is also constrained such that a particle cannot diffuse through a temperature or n_e gradient faster than electron collisions can bring it into thermodynamic equilibrium with its new plasma surroundings, a condition summarized as:

$$\frac{T(x + \lambda) - T(x)}{T(x)} \ll 1 \quad (3-9a)$$

$$\frac{n_e(x + \lambda) - n_e(x)}{n_e(x)} \ll 1 \quad (3-9b)$$

where λ is the characteristic diffusion length- i.e. the distance that a particle diffuses during τ_{rel} .⁵⁸

Equations 3-8a and 3-8b are evaluated by determining the characteristic time scale over which the plasma populations evolve (i.e. over which they are perturbed): $T^*(dT/dt)^{-1}$ and $n_e^*(dn_e/dt)^{-1}$. In order for the plasma to remain in equilibrium, both of these “perturbations” must be slower than the plasma populations re-equilibrate, as measured by τ_{rel} . Evaluating Equations 3-9a and 3-9b is more difficult experimentally, since it requires spatially resolved measurements of plasma parameters and knowledge of the diffusion coefficient.

In short, the McWhirter criterion is the minimum condition necessary for LTE in a LIBS plasma, but is not sufficient to guarantee LTE.⁵⁸ The spatial and temporal gradients must also fulfill the conditions set out in equations 3-8 and 3-9.⁵⁸ These latter conditions are not commonly evaluated in the LIBS literature, especially in the more exotic, short-lived plasmas where they are likely to be most important.

MicroLIBS

MicroLIBS (μ LIBS) is confusingly defined as both LIBS carried out with micrometer spatial resolution, or LIBS carried out with microjoule pulse energies.⁶⁰ Only a few researchers, including Mermet⁶¹, refer to the spatial character separately as “LIBS microprobe”. Each necessitates the other, however, as low laser pulse energies are required to sample on a micron length scale and tightly focused laser spots are required to achieve breakdown with microjoule laser pulses. As a result, microLIBS requires good laser focusing optics and tight control over sample presentation and positioning to create a robust and repeatable breakdown.

Traditionally, microLIBS setups have scaled down the ablation dimensions by simply attenuating a Nd:YAG or excimer laser. A survey of the microLIBS literature yields the usual variety of lasers found in macroLIBS- Nd:YAG (fourth harmonic, 266nm), excimer (308nm XeCl and 248nm ArF), femtosecond Ti:Sapphire (second harmonic, 400nm). In every case surveyed except the Ti:Sapphire used by Fedosejevs et al.⁶², the laser energy was attenuated by at least an order of magnitude to allow microLIBS. Such large lasers, in addition to their price, are cumbersome and are limited to repetition rates less than 100Hz in many cases. Recently, microchip lasers have appeared in the LIBS literature, though the studies have not emphasized the potential applications for micron-level material characterization.

The small plasma size of microLIBS allows better coupling with spectrometer entrance slits or fiber optic apertures, while the low laser energy diminishes the need for detector gating. MicroLIBS allows elemental surface mapping, the identification of surface inclusions and the characterization of single particles. The small sampling size, however, complicates the calibration process, as there are relatively few standard samples that are homogenous on a micrometer spatial scale.⁶³ In the absence of appropriate calibration standards, calibration-free techniques could simplify measurements, but all such techniques assume LTE, which has not been studied at such low pulse energies.

Additionally, the usual inverse relationship between resolution (spatial, in this case) and signal applies. Although the semiconductor industry has pushed optical resolution to extreme limits, Mauchien⁶⁴ and others⁶⁵ have found that laser spots much smaller than three micrometers do not produce detectable plasma atomic emission. The actual crater size or laser spot size may not be the relevant figure of merit, in any case, as the LIBS process can modify the sample beyond the ablation crater as Cravetchi et al. found in their study of scanning microLIBS for aluminum alloy surface mapping.⁶⁶ Although the laser craters were only 10 μ m in diameter, they found that the plasma shock wave would clear the oxide layer from the adjacent surface, creating an effective modification region that was closer to 50 μ m in diameter for each shot, potentially affecting adjacent samplings if the surface were mapped at a 10 micron pitch. Redeposition of ablated material adjacent to the crater may also limit the effective resolution.

The relatively low pulse energies used in microLIBS (microjoules rather than millijoules) give rise to unique plasma dynamics. While standard LIBS measurements are overwhelmed with continuum for a microsecond or more, microLIBS plasmas may only last for a few tens of nanoseconds to just a few microseconds from plasma ignition to the disappearance of plasma emission. Many authors have noted, however, that the continuum is much shorter in microLIBS plasmas. Rieger et al., for instance, found that the optimum signal to background ratio was achieved with ICCD gates beginning ~100ns after their 100μJ ablation pulses.⁶⁷ They also found that as the pulse energy increased, the S/N maximum moved to later gate delays. Gornushkin et al. demonstrated microLIBS plasmas with the majority of the continuum lasting only a few hundred picoseconds.^{15a} Because of the decreased continuum emission, authors speculate that gating may not be necessary, or that the benefits are marginal. In any case, gating such fast-evolving plasmas requires careful timing and fast electronics.

Microchip LIBS

Microchip and powerchip lasers are a natural fit for Mermet's "LIBS microprobe" as they are limited to pulse energies less than a hundred microjoules.⁶¹ The new microchip lasers were quickly absorbed into the LIBS community as they became available commercially in the early 2000's.^{15a, 15c, d} Gornushkin et al. performed one of the initial qualitative studies of the potential for microchip LIBS with a commercial microchip laser producing sub-nanosecond pulses of 7μJ.^{15a} The peak irradiance of ~25GW/cm² produced plasmas exhibiting two spectral lifetimes- a fast 0.8ns portion and a longer, less intense emission lasting for ~8ns. This is several orders of magnitude shorter than the lifetime of emission from more typical nanosecond-millijoule laser plasmas. The laser was evaluated for use with simple, ungated spectrometers, which

could allow for the construction of very portable, low-power consumption instruments, but exclude the possibility of gating, especially at the 5kHz repetition rate of the laser. The authors do note, however, that gating would still be desirable, if impractical.

The ablation regime was clearly more akin to ablation by nanosecond lasers than the more exotic picosecond and femtosecond lasers, with evidence of melting on the craters. The ablation craters were extremely symmetrical, probably because of the quality focus provided by the highly gaussian beam. The authors also point out a situation typical of ablation in the sub-millijoule regime, namely that repeated breakdown on the same spot leads to weak plasmas, then to a complete cessation of breakdown, requiring that the sample be moved constantly to take advantage of the laser's high repetition rate. Furthermore, surface preparation was found to be critical- irregular pellets of graphite and magnesium hydroxide were not amenable to measurement.

To date, microchip lasers have not been employed for the type of surface mapping that Cravetchi and others have demonstrated.^{64, 66, 68} This would be logistically complicated with passively Q-switched microchip lasers due to their fixed repetition rate. Some commercial powerchip lasers, on the other hand, can be factory-optimized for specified repetition rates and can even be singly externally triggered, allowing a greater degree flexibility in experimental design. In any case, recording individual spectra at a kilohertz would tax the CCD readout and data transfer speeds of current detectors.

The studies of microchip and powerchip LIBS have noted that the spectral lines are quite wide, and thus, that increased spectral resolution is not practical or useful. Two studies at Aerodyne Research (Billerica, MA) have found that analytical measurements with microchip lasers are hampered by poor resolution of neighboring

lines.^{15d, 69} They used partial least squares (PLS) calibrations to compensate for the poor resolution, achieving LOD's between 0.05 and 0.15%. They also note that the precision is limited by noise with a 1/f character.

Gornushkin et al.'s subsequent work with the higher energy powerchip lasers at the University of Florida compared figures of merit for intensified, high-resolution detection with detection via a portable, low resolution spectrometer in the analysis of steels.^{15c} The ICCD was operated in an ungated mode, and was not used to discriminate against continuum, so the comparison may be misleading (since ICCD's are typically employed in LIBS in order to gate away from the continuum). As will be discussed later, this laser does have a jitter of several microseconds, which precludes gated measurements within plasma lifetimes. They also measured time-integrated plasma excitation temperatures at ~11,000K, using Boltzmann plots, and found them to be independent of sample temperature. Once again, it should be pointed out that this is a time-integrated measurement. In the context of the temporally and spatially evolving plasma, spectra are records of plasma emissivity, and are thus weighted to the most emissive, hottest points in the plasma's spatial and temporal evolution. The Boltzmann expression for the spectrally integrated line emissivity ($W \cdot cm^{-3} \cdot sr^{-1}$) intensity of the emission from a single state is exponential in temperature and is given by:

$$\epsilon_{mn} = \frac{hc}{4\pi\lambda_{mn}} \cdot \frac{N(T)}{U(T)} \cdot g_m A_{mn} e^{\frac{-E_m}{kT}} \quad (3-1)^{56}$$

where ϵ_{mn} refers to a transition between upper state m and lower state n , h is Planck's constant, c is the speed of light, λ_{mn} is the wavelength of the transition, $N(T)$ is the number density the atomic species in the plasma, $U(T)$ is the partition function, g_m is the statistical weight of the upper level, A_{mn} is the spontaneous transition probability of the

transition, E_m is the energy of the upper level, k is the Boltzmann constant and T is the absolute temperature. Ignoring the temperature dependence of the partition coefficient, a time-integrated temperature measurement is exponentially weighted to the highest temperature in the plasma. Likewise, as the temperature is highest in the early part of the plasma, any characterization made from time integrated emission will represent the conditions present in the earliest part of the plasma.

To date, there has been little characterization of microchip and powerchip plasmas, and certainly no time-resolved studies. Acceptance and deployment of microchip/powerchip LIBS will require understanding of the evolution of the plasma. Better understanding of the plasmas will allow a better match between microchip LIBS and its potential niche in the wider technique.

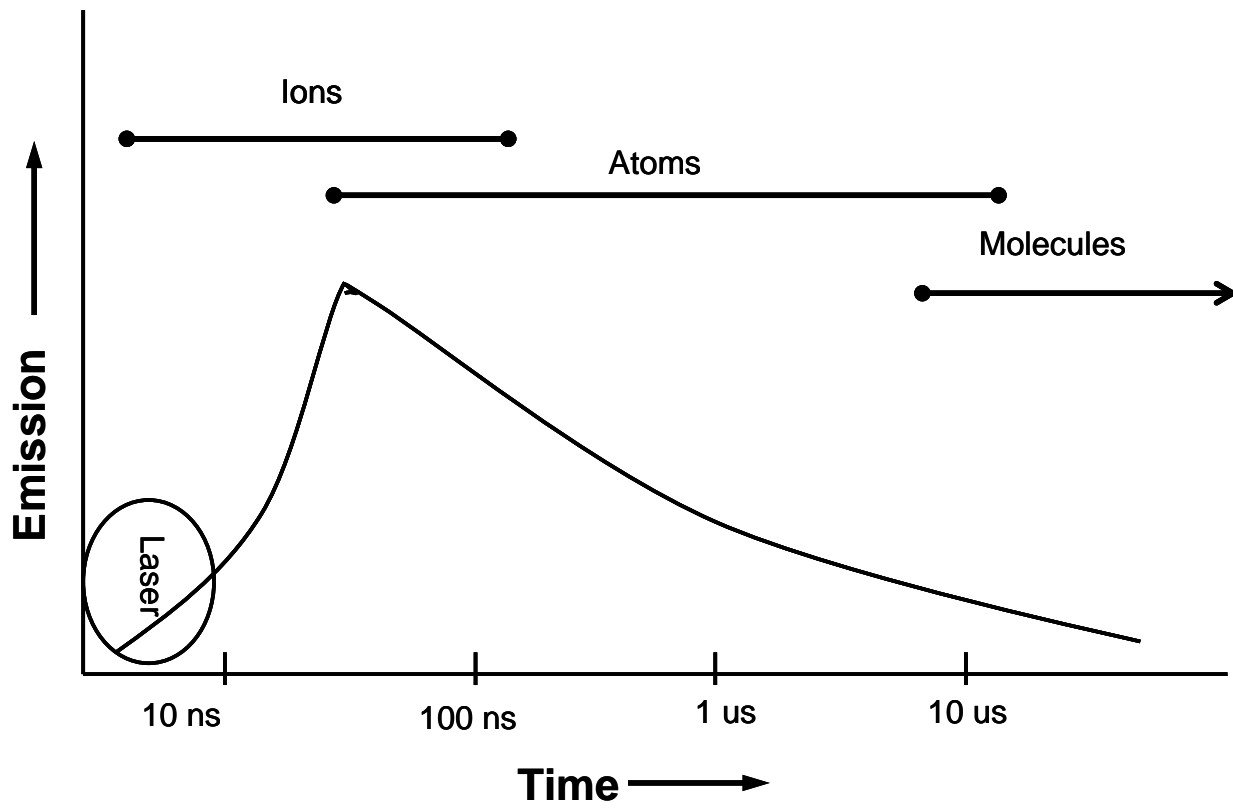


Figure 3-1. Evolution of LIBS plasma- composition and radiation.

CHAPTER 4 TIME-RESOLVED CHARACTERIZATION OF POWERCHIP LIBS PLASMA

Instrumentation

Time-resolved measurements of the plasma were carried out with a LIBS microscope, as depicted in Figure 4-1. The optics are based around a Thorlabs optics cube. The laser pulse is reflected into the microscope objective by a dichroic mirror and focused on the sample by the objective lens (best form lens or reflecting Schwartzchild objective). The BK-7 glass best form lens (Thorlabs, 5cm focal length) is simple, provides high transmission due to an antireflective coating, and can produce spot sizes of 2-8 μ m, depending on alignment. It does, however, add significant chromatic aberration due to its short focal length. The Schwartzchild objective (15x, 0.4NA, 13mm focal length Newport 50105-02) provides a high numerical aperture for focusing the laser and collecting emission, but blocks 27% of the excitation and emission light due to the projected image of the central mirror. At small pulse energies, this is particularly problematic for super-linear processes like LIBS. As a result, the measurements in Chapters 4 and 5 are made with the best form lens unless otherwise specified.

The laser focus is measured by the knife-edge method. A razor blade is placed on the sample stage, which is mounted on an xyz-positioner actuated with piezoelectric stiction positioners (Picomotor, New Focus). These are capable of sub-micrometer resolved motion, though the repeatability of positioning was more questionable. The transmitted laser power was measured with a large area photodiode, amplified with a current to voltage amplifier (SR 570, Stanford Research) and integrated with a boxcar averager (Stanford Research). Boxcar output was measured with a USB 6009 DAQ (National Instruments). The entire measurement was automated with a program written

in Labview. In order to avoid ablating the razor blade or damaging the detector or amplifier, the laser energy was attenuated with absorption filters between the delay line and the microscope cube. The setup was checked for linearity with a 0.3 neutral density filter before focus measurements. A representative obscuration trace is shown in Figure 4-2. As measurements were not extremely stable (probably due to the delay line), all spot sizes reported should be taken as containing an uncertainty of at least 30%. By measuring the FWHM of the laser spot at a series of stage heights, the minimum focus was located. When the laser was focused through a window for measurements under different atmospheres, it was necessary to calibrate the height with the window in place due to the relatively high effective numerical aperture of the focusing lens. The laser focus shifted from day to day, perhaps due to the sensitivity of the ~20m delay line to any change in angle. As a result, the focus was located before spectroscopic measurements at the beginning of each day. All plasma measurements were made at the laser focus. This did not correspond to the optimal focus for emission collection, however, because the plasma propagated back toward the lens during its evolution and because the focal length of the lens at the UV emission wavelengths was less than that at the ablation laser wavelength (532nm).

Plasma emission was collected and collimated by the focusing objective. Because the best form objective lens is glass, it only transmits wavelengths above ~300nm. The shortpass dichroic passed wavelengths below ~ 450nm, resulting in a 150nm effective bandpass. For long wavelength (H α emission) measurements, the shortpass dichroic mirror was replaced by a 532nm longpass razor-edge dichroic (Semrock) designed for Raman spectroscopy. A colloidal knock-out filter (not shown in

Figure 4-1) optimized to block 532nm light could be placed between the dichroic and the flip mirror. The collimated light was imaged onto the monochromator slit with a 9.5cm focusing lens, resulting in magnifications of 7.3 and 1.9 for the Schwarzschild objective and the best form lens, respectively. The magnification was kept low in order to maximize light collection at the spectrometer slit. In this orientation, the collimating mirror of the F/6.5 Acton Spectrapro (0.5m) monochromator was slightly underfilled. Fine adjustment of the positioning was performed by mounting the flip mirror on a vertical translation stage. Adjusting the vertical position of the mirror moved the image up and down the slit while moving the depth of the image relative to the plane of the slit. Final adjustment was carried out with tip/tilt controls on the flip mirror.

Detection was with a PI Max II ICCD (Princeton Instruments, Trenton, N.J.) interline ICCD. The ICCD provides time resolved images by gating the bias between the photocathode and the MCP image intensifier. Depending on the electronics selected, the minimum gate width was 1.9ns or 8ns, although the 1.9ns gate has a lower effective quantum efficiency and may introduce spatial effects into measurements. The CCD chip was thermoelectrically cooled to reduce the production of thermal electrons (dark charge). Relative gain was calibrated with a deuterium lamp (Figure 4-3).

ICCD operation involves balancing several factors to maximize signal to noise on a given measurement. Spectral measurements were made with on-chip integration of multiple laser shots and with readout register binning of the region of interest (Figure 4-5). This binning procedure reduces the effect of readout noise at the charge amplifier and A/D converter. Because single plasmas actually produce relatively few photons, a

single readout would be CCD chip readout noise limited and suffer at low MCP gains. Thus, S/N is improved by integrating multiple plasmas on the CCD face, then binning the region of interest in the readout register, decreasing the relative influence of readout noise while maintaining a high linear dynamic range.

The rate of on-chip integration is limited only by the photocathode gating repetition rate (5kHz in this case), while single-shot readouts would be limited by the time required to read every pixel on the chip individually- approximately one second. Of course, on-chip integration of multiple shots only generates a signal to noise benefit if the experiment generates signal faster than dark charge can accumulate. Increasing the MCP gain can be used to improve the signal to dark charge ratio (as well as the signal to readout noise ratio) at the expense of dynamic range, as the electron capacity of each pixel is limited. Decreasing the CCD temperature decreases the rate at which it accumulates dark charge, but tended to cause arcing within the electronics if the thermoelectric cooler was set below -8.5°C . With judicious choice of detector settings, the S/N ratio of measurements was almost never detector noise limited, as will be discussed in Chapter 5.

The powerchip laser is externally triggerable, but with a jitter of $\sim 7\mu\text{s}$ due to variations in the cavity build-up time.¹⁰ Thus, time resolved measurements of plasma evolution cannot be made with a resolution greater than $7\mu\text{s}$, which exceeds the plasma lifetime reported in Amponsah-Manager et al. by three orders of magnitude.^{15b} In order to make time resolved measurements, the ICCD was triggered with the actual laser pulse. This procedure is complicated by the insertion time of the ICCD electronics, cables, etc., which amount to $\sim 60\text{ns}$. A 25 meter delay line was inserted between the

laser and the LIBS microscope so that the arrival of the laser pulse could coincide with the earliest allowable gate.

Although the powerchip laser divergence is less than 2mrad, this figure becomes appreciable over the length of the delay line. In order to compensate for the divergence and keep the transmitted laser energy high without losses from a beam expander, the delay line was constructed from two cavity ringdown mirrors (6 meter radius of curvature) with greater than 99.9% reflectivity at 532nm and a plane copper vapor laser cavity mirror. With this configuration, the fast axis of the laser beam was ~6mm at the dichroic mirror, substantially underfilling the 2.5cm focusing objective.

Laser-Sample Interaction

Microchip and powerchip lasers occupy a middle region in the available range of laser pulse durations. They are shorter than the typical LIBS laser by approximately an order of magnitude, but too long to expect significant picosecond ablation behavior, though perhaps still short enough to distinguish themselves from the more typical Nd:YAG lasers found in the LIBS literature. In order to study the powerchip ablation behavior, the drilling rate through a 0.001" (25 μ m) thick sheet of aluminum was measured with both fundamental and 532nm powerchip lasers. A variety of parameters have been used in the literature to quantitate the various aspects of substrate removal by laser ablation,⁵⁶ but this work will primarily use drilling rate (μ m/laser pulse).

The aluminum foil target was laminated onto microscope slides. Gas was flowed over the sample using a slightly constricted open-topped chamber sealed onto the laminated surface. Flows were kept at ~1L/min in order to purge the surface of ambient air. Laser focus was located with the knife-edge method as detailed above.

Laser breakthrough was determined by leaving the knife-edge detection setup under the microscope slide. In this case, however, there were no filters in front of the photodiode, making the system extremely sensitive to laser breakthrough. In fact, the breakthrough shot generally saturated the detection system. The whole setup was controlled by a program written in Labview; the computer alternately triggered a laser shot then read the boxcar voltage, repeating the process until the boxcar signal exceeded a threshold value, at which point the cumulative number of laser triggers was recorded. The laser trigger rate was kept under ~50Hz. Because the lamination process was not extremely repeatable and resulted in somewhat imperfect surfaces, data was taken with alternating gases in order to avoid systematic errors. Laser pulse energy was varied with neutral density filters between the delay line and the microscope cube.

The drilling data is displayed in Figures 4-6 and 4-7. Photomicrographs showed crater diameters of ~20 μm in aluminum for single shots of 30 μJ of 532nm under air. Extrapolating the air data in Figure 4-6 to 30 μJ , the average depth ablated/per laser pulse was ~600nm. Approximating with the volume of a cone, the 532nm powerchip removes 60 μm^3 /pulse at 30 μJ , which corresponds to 0.17ng of Al and an ablation efficiency of ~6ng/mJ. This rate is similar to the rate (85 μm^3 /pulse) reported by Lopez-Moreno et al. in copper using the slightly higher energy 1064nm powerchip.^{15c} They calculated crater volumes exactly using white light interferometer data, which may account for the difference, along with the different target material. In both Lopez-Moreno et al.'s study and this work, however, the drilling rate (μm /pulse) or the ablated

volume per pulse increased with laser fluence (note that they only examined breakdown under air).

Because of the high uncertainties in the 532nm powerchip data in this measurement, analysis at any given energy does not show a significant difference between the drilling rates under the different cover gases. Helium, though within the error bars of the other gases, did show consistently slower drilling than the other gases, especially at lower pulse energies. The rates under the various gases begin to converge at higher laser pulse energies.

The 1064nm powerchip drilling data, on the other hand, shows appreciable difference between drilling under the different gases, with drilling fastest under argon and slowest under helium. The air and helium drilling rates converge at higher 1064 energies, though the argon rate remains consistently higher. Comparison of air drilling rates with the two powerchip lasers using $\sim 25\mu\text{J}$ laser energies gave experimentally identical results (43 shots of 1064 vs. 41 shots of 532nm). It should be kept in mind that the error in determining spot diameter is on the order of 30% and reproducibility of sample presentation results in an additional measure of uncertainty in the spot size (diameter), with a quadratic effect on irradiance. At lower pulse energies, there is an additional caveat to approximating ablation efficiencies with the drilling method: because of the non-linear nature of LIBS, small experimental fluctuations near the breakdown threshold can seed or inhibit plasma formation, meaning that not every laser pulse leads to plasma formation and that the ablation rate may be underestimated.

These drilling results contrasts with the results of Gravel and Boudreau⁵⁵ shown in Figure 4-8. They measured drilling rates in brass with a 22ns, flashlamp-pumped

Nd:YAG laser emitting at the fundamental. Their data shows an increase in drilling rate up to a maximum fluence of 1064nm radiation ($\sim 2\text{GW}/\text{cm}^2$), after which the rate decreases with increasing laser energy. Significantly, the fall-off in drilling speed was faster under argon than under helium cover. They attributed this behavior to shielding by a secondary breakdown in the cover gas, but well above the target surface. The secondary plasma absorbed subsequent energy from the laser pulse, cutting off the end of the laser pulse.

Ionization energies for helium, argon, nitrogen and oxygen are tabulated in Table 4-1. Not surprisingly, the more easily ionized argon showed a greater decrease in drilling at high irradiance. Shadowgraphic imaging further supported their shielding hypothesis with the appearance of a laser-absorbing laser-supported detonation (LSD) wave in the cover gas at higher fluences. Helium, with its higher ionization energy, produced a much slower decrease in drilling rate at increasing irradiances, likely due to the lower electron number density that it generates in the shielding plasma. The lower electron number density in the shielding plasma keeps the α_{IB} low, and a lower percentage of the pulse tail is absorbed by the shielding plasma.

The data in this work, in comparison, was taken at peak irradiances well in excess of $10\text{GW}/\text{cm}^2$, and show no such decrease in drilling rate with increasing irradiance. In fact, the relationship between cover gas ionization energy and drilling rate in this work is the opposite of that found in Gravel and Boudreau. The 1064 powerchip data in Figure 4-7 is especially striking given that Equation 3-1 implies that plasma shielding due to the electron-ion term should be greater under 1064nm ablation (note that the less-cited inverse exponential dependence on wavelength in multiphoton

ionization does give the opposite trend). The difference between this work and Gravel could arise from a variety of factors, including different laser focusing numerical apertures, spot sizes, or beam qualities. Most likely, however, is the difference in laser pulse lengths, 22 vs. 0.5ns (this work). Given that there is no evidence of gas breakdown plumes and laser shielding in this work, we attribute the differences in drilling rate between gases at a given energy to either the thermal conductivity of the gases, or differential plasma confinement effects during the laser pulse. The higher molecular weight gases (argon, air) better confine the plasma and allow higher temperatures and longer plasma residence in the immediate vicinity of the surface at the extremely early times relevant to ablation. (Table 4-1)

Plasma Dimensions

Because of the optical and timing difficulty of carrying out shadowgraphy measurements on tiny LIBS plasmas, hydrogen emission imaging measurements were made in order to approximate plasma dimensions. Given the high RMS velocity of hydrogen, it was assumed that the hydrogen would very nearly diffuse to fill the entire LIBS plasma at any time. Estimates of LIBS plasma dimensions were made by imaging the collected light through an H α filter (Baader) centered at 656.5nm. The image was centered on the fully-opened slit of the monochromator with the grating set to the zeroth order (0nm). The H α filter bandpass was 7nm. Because the filter does not distinguish between continuum and line emission, however, the data at early times is a combination of the two. The earliest two time points were taken with a 2ns gate, while the subsequent points used 8ns gates. Plasma dimensions were estimated as the FWHM of the emission image. As a line of sight image, these measurements are necessarily convoluted by the 3-dimensional emissive volume. No attempt was made to correct for

this artifact. Additionally, there was spatial jitter in the plasma formation caused either by imperfections on the target surface, movement in the delay line or flex in the sample presentation stage, all of which may have smeared out the actual dimensions somewhat, especially at early times, though no attempt was made to quantitate this.

Plasma diameters and velocities are graphed in Figures 4-9 and 4-10. At early times plasmas under all three gases display similar dimensions. Although there is not adequate data to verify the trend due to poor S/N in air, the air plasma size eventually falls behind argon at late times. Although the error bars limit comparisons of the expansion rates at any single time, the velocity trends is clear: $v_{\text{He}} > v_{\text{Ar}} > v_{\text{air}}$. The difference in plasma sizes is easily explained with the fact that plasma confinement is inversely related to the molecular mass of the gas at a given pressure, giving rise to the larger plasma dimensions in helium. The higher thermal conductivity of helium may also distribute energy more rapidly throughout the plasma, allowing for a greater emissive volume of analyte and increasing the apparent plasma size. Additionally, the faster expansion under helium would be expected to lead to more rapid PV energy loss from the plasma, a consideration relevant to the temperature evolution of the plasma.

Time-Resolved Excitation Temperature

To supplement the simple time-integrated Powerchip LIBS temperature measurement that Lopez-Moreno et al.^{15c} made in air, excitation temperatures were measured under air, helium, and argon at various delays after plasma formation by the 532nm Powerchip. Plasmas were formed on aluminum alloy b8 (see Appendix A). The spectroscopic parameters of the Fe atomic lines used in the Boltzmann plots were taken from Reference 70, and can be found in Appendix B. The plots were constructed with integrated line intensities, as the line widths varied appreciably in the course of the

plasma evolution and plots of the simpler peak height measure were found to give significantly different results than the more accurate peak area. A representative group of spectra taken under air atmosphere can be found in Figure 4-11.

Spectra were measured in a custom-built sample chamber with a gas flow of ~300 cc/min. The chamber window attenuated the laser beam somewhat, allowing 26 μ J of 532nm laser energy to reach the ~8 μ m (FWHM) focal spot. Spectra were acquired using 50 μ m slits and a 2400mm⁻¹ grating unless otherwise specified, resulting in a CCD-pitch limited bandpass of 0.055nm. CCD acquisition parameters, including on-chip accumulation settings and gain were set to maximize S/N ratio as discussed earlier. Spectra were background subtracted and integrated with custom programs written in Labview. A representative Boltzmann plot can be found in Figure 4-12. At early and late times, some transitions were omitted due to interference from broadened lines or poor signal/noise.

The lines used in these Boltzmann plots are convenient because they span an eV of upper state energies within a narrow spectral range. As a result, it was initially assumed that calibration of the detector spectral response was not necessary. Unfortunately, later experiments indicated that the spectral response is irregular across the face of the chip. (Figure 4-13) We assume that this is due to the low quality of the short pass dichroic mirror used, although other less likely culprits include chromatic aberration of the lens and the gradual variation of the grating efficiency across the spectral range. Note that the efficiency also varies along the height of the slit, indicating that the spectral efficiency of the optics also varies across the numerical aperture,

further implicating the dichroic mirror, which might be expected to have a strongly angle-dependent spectral response.

In order to verify that the spectral response had no effect on the calculated temperatures, a simple spectral calibration procedure was devised. It was assumed that the continuum emission early in the plasma is fairly uniform over the narrow spectral range. Thus, by setting the gate to collect the continuum early in the plasma evolution ($t = -2\text{ns} \rightarrow 13\text{ns}$), the plasma itself could be used as a relative spectral calibration source located in approximately the same position as the plasmas used to collect the iron spectra. To correct the iron spectra they are background subtracted then divided by a high-quality continuum spectrum to correct for the varying optical efficiency of the setup. The effect of the correction on spectra can be seen in Figure 4-14.

There are caveats, however. The spectra must be taken early in the plasma, before the plasma has expanded. As a result, the calibration is for the central aperture of the optics. At later times, the optics collect emission from a larger area (i.e. wider numerical aperture), and the IRF from the early, narrow vertical distribution may not apply. Ideally, the vertical binning is kept as small as possible to minimize error from the numerical aperture.

A series of IRF-corrected and uncorrected temperature measurements are graphed in Figure 4-15. Within four measurements of excitation temperature, the determinations from corrected and uncorrected spectra did show a discrepancy, but were on the same order as the uncertainty of the measurement. The insignificance may be due to the random distribution of excitation energies across the response function

and the general uncertainty involved in integrating the peaks. In subsequent measurements, the instrument's spectral response was found to vary, probably as a result of changes in the plasma's position as the delay line shifted slightly over the course of several days.

In any case, the uncertainty at early times is likely dominated by difficulties in estimating the peak parameters due to poor resolution between the highly broadened lines. Accuracy is also limited by the narrow spread of upper state energies used in the Boltzmann plot. Additionally, the long (8ns) gate used also obscures some of the rapid evolution at early times due to the emissivity weighting of measurements discussed in Chapter 3.

The time-resolved temperature values are plotted in Figure 4-16. Not surprisingly, the temperatures reported by Lopez-Moreno et al.^{15c} (~11200K) are only representative of the first 15ns of plasma evolution, though it should be kept in mind that Lopez-Moreno used the fundamental output at a higher energy (~60μJ), and neither their study nor this work has measured plasma temperature as a function of pulse energy. The plasma temperatures in this work are similar for all three cover gases at early times, where uncertainty is large due to noise from the continuum and difficulty separating the broad lines. At later times, the plasmas under argon are approximately 20% hotter than those in helium, as could be expected from the relatively lower thermal conductivity of argon-- $38.8 \times 10^{-6} \text{ cal}/(\text{s} \cdot \text{cm} \cdot ^\circ\text{C})$ vs. 56.2×10^{-6} and 333.58×10^{-6} for air and helium, respectively.⁷¹ Cover gas confinement may play an even greater role at early times, as the degree of plasma confinement due to cover gas inertia is a function of the

cover gas' molecular mass (Table 4-1), as discussed earlier. Greater cover gas confinement leads to decreased PV work and should decrease plasma cooling.

The comparison of helium and air plasma temperatures is more complex. Although the two are not different within the uncertainties, the helium temperatures seem to be consistently lower than the air data at early times. At later times, $t > 70\text{ns}$, there seems to be a crossover and the helium plasmas are actually hotter than the air plasmas. Aguilera and Aragón's time resolved plasma studies with a conventional LIBS setup showed a similar crossover.⁷² Interestingly, the opposite trend has been observed by Iida at 100Torr; temperatures under helium are initially higher than under air, but temperatures under air are higher at later times.⁷³

Time Resolved Electron Number Density

The temperature measurements were combined with H α (656.5nm) Stark broadening measurements in order to calculate time-resolved electron number densities (n_e). It was necessary to replace the shortpass mirror with the Raman dichroic in order to make measurements at such long wavelengths. As a result, n_e and temperature measurements could not be made simultaneously.

The FWHM of the H α line is sensitive to the electron number density of the plasma, according to the relationship:

$$n_e = 8.02 \times 10^{-12} \left(\frac{\Delta\lambda}{\alpha} \right)^{3/2} \quad (4-1)^{74}$$

where n_e is in cm^{-3} , $\Delta\lambda$ is the HWHM of the spectral line and α is the Stark broadening parameter (\AA) and is a slight function of temperature. Appropriate α values were taken from Griem.⁷⁴ Representative profiles are shown in Figure 4-17. Tests showed that the $50\mu\text{m}$ slit did not convolute the line profile when coupled with the 2400mm^{-1} grating.

Doppler broadening was minimal compared to the Stark width. For example, a kinetic temperature of 10^4K produces a Doppler FWHM of 0.08nm in the H α 656.5nm line. Only at the longest delays in the helium data could there have been a slight convolution of Doppler and Stark broadening to create a Voigt profile as the line width approached 0.3nm (the Doppler width at this time was 0.06nm).

Initially, it was assumed that attempts to measure the hydrogen alpha line under noble gas atmospheres would require the addition of some source of hydrogen, and initial experiments were performed by bubbling the gas through water prior to the ablation cell. Later experiments showed that there was a natural source of hydrogen in the aluminum sample- either water adsorbed on the surface or hydroxides from reaction with atmospheric water. In fact, H α intensity was greatest in the dry noble gas atmospheres, and S/N was best in helium, an effect that has been noted by other authors,⁷⁵ possibly because the narrow line width increased the spectral radiance and, as will be seen, because the electron number density (and therefore the continuum) was decreased. The S/N ratio in air was particularly poor, perhaps due to quenching with molecular oxygen. As a result, Stark widths in air could not be determined at times beyond ~55ns, at which point the peak was still narrowing. At early times, measurements in argon and air were complicated by the line to continuum ratio, precluding determinations before ~15ns.

The calculated number densities are graphed in Figure 4-18. The electron number densities in helium are an order of magnitude lower than the n_e in air or argon, a finding that agrees well with data from more typical LIBS plasmas, such as the measurements of Aguilera and Aragón.⁷² At first glance, the data are easily explained

by the relative ionization energies of oxygen, argon and helium. (Table 4-1)

Consideration of the overall plasma composition clouds the picture, however, as is discussed below.

Assuming that aluminum is ablated with equal efficiency under helium and air at $\sim 25\mu\text{J}$ (their drilling rates are approximately equal), the aluminum number density in a $10^6\mu\text{m}^3$ plasma volume (estimated from Figure 4-6, 40ns) is $\sim 3 \times 10^{18}\text{cm}^{-3}$. The Lochschmidt number, on the other hand is 2.7×10^{19} at 273K and 1atm, and represents an upper bound on the helium number density. Both of these numbers are higher than the electron number density in the helium plasma at 40ns ($4.5 \times 10^{16}\text{cm}^{-3}$). Considering that the aluminum number density is on the same order as the cover gas number density (and likely much higher early in the plasma evolution), one expects that the ionization properties of aluminum (Table 4-1) would be the dominant contributor of electrons in the Saha equilibria (Eq. 3-4) by a factor of $\sim e^{18}$, taking kT as 1eV. This suggests that, regardless of any difference in atom number densities, aluminum should be the dominant source of ions, and that the ionization potential of the cover gas is not significant since it is bound to be much higher than the ionization potential of aluminum.

This leaves plasma temperature as the source of the difference in electron number densities between the gases. (see Saha Eggert Equation, 3-4) Temperature could explain the difference between argon and helium, as argon is much cooler than helium beyond 20ns. Given that the helium and air temperatures are similar, however, temperature can not explain the n_e difference between these two cooler plasmas. The plasma expansion rates may serve to explain part of the discrepancy, given that helium plasmas expand so rapidly. For instance, the ratio of helium to air plasma diameter at

40ns is 200:125, which gives a volume ratio of 4:1, which may explain part of the 10-fold difference in number density at this time. This is possibly a more plausible explanation for the n_e variation between cover gases than purely ionization energy if one assumes that ionization states are in equilibrium. In fact, the assumption of equilibrium is evaluated in the next section. These number densities, when coupled with plasma expansion rates have important implications for local thermodynamic equilibrium (LTE), or the lack thereof in powerchip plasmas.

Microplasma LTE

In light of the theoretical considerations described in Chapter 3, it is clear that fully space and time-resolved data is necessary to thoroughly evaluate LTE in powerchip microplasmas. The small dimensions (10^{-6}cm^3 based on a $100\mu\text{m}$ radius) and fast time evolution ($\sim 150\text{ns}$) complicate the measurements, however. We have solved the timing problem with a delay line and fast ICCD. Spatially-resolved data is more problematic, however, and is prohibitive even in “normal” LIBS plasmas.

As was discussed in Chapter 3, three spatial parameters and three temporal parameters are needed to fully evaluate the plasma for LTE:

- 1) τ_{rel} - the time required for the plasma to return to equilibrium after any perturbation. (Equation 3-7)
- 2) τ_{exp} - the time taken for the plasma to expand against the background gas, generally taken to be the ratio of the plasma diameter to the expansion velocity
- 3) $\tau_{\text{char}}(m)$ - the characteristic decay time of m (either the n_e or the temperature). Defined in Equations 3-8a and 3-8b as the value of the

parameter of interest at time t divided by its rate change at time t -- i.e. $m/(dm/dt)$.

At the time of this writing, no space-resolved data was available for powerchip microplasmas (or microplasmas in general), so this discussion will be limited to the time variation of n_e and temperature. Note that τ_{char} and τ_{exp} are measured values. τ_{rel} is calculated, although it is determined for a given excited state energy by the n_e and temperature (both of which are measured experimentally). The details of the individual measurements in the different atmospheres have been discussed above. The taus and the experimental parameters used to calculate them are summarized in Table 4-2, and all reference the 3.33eV energy of the Fe(I) resonance line at 371.99nm.

For equilibrium conditions to be warranted, τ_{rel} must be shorter than $\tau_{char}(m)$ at all times. From the data shown in Table 4-2, we can draw the following conclusions:

- 1) In helium plasmas, the characteristic taus for both temperature and n_e evolution are out of LTE at all times.
- 2) Air and argon plasmas are *possibly* in LTE at early times. At later times, both plasmas are out of equilibrium in terms of n_e , while T_{exc} is out of equilibrium in air at later times.
- 3) Helium plasma relaxation times (τ_{rel}) are far longer than the other plasmas at all measured times, mostly as a result of the ten-fold lower electron number densities in the helium plasmas (Equation 3-7)

Note that this discussion lacks spatially resolved data, so we can only *exclude* LTE with certainty; conformity to the McWhirter criterion and Equations 3-8a and 3-8b is

necessary, but not sufficient to guarantee LTE in the absence of any evaluation of Equations 3-9a and 3-9b.

Contrast these conclusions with the calculated McWhirter criteria in Figures 4-19, 4-20 and 4-21. The McWhirter criterion alone would indicate that argon and air plasmas are in LTE at all times and that helium is in LTE before 60ns. In light of Table 4-2, the helium plasma is *never* in equilibrium, and the argon and air plasmas may be in equilibrium only at early times, despite fulfilling McWhirter at all times. Note that this discussion has been developed in reference to a 3.33eV transition-- larger energy gaps in adjacent levels would require yet longer relaxation times and result in more stringent temporal requirements for LTE.

To our knowledge, this is the first evaluation of any LTE considerations “beyond the McWhirter criterion”⁵⁸ in microLIBS or microchip/powerchip LIBS plasmas. Powerchip plasmas are extremely fast evolving and relatively cool. Characterization of such plasmas requires the fast gates provided by our camera, as well as the low timing uncertainty provided by the delay line. Without this fast time resolution, the relaxation times would have been calculated with higher n_e 's and temperatures (due to emissivity weighting), resulting in underestimation of relaxation times which would erroneously indicate that the plasma could be in LTE. Because the minimum gate (2ns) in the ICCD used in this work is shorter than any of the τ_{rel} reported in Table 4-2, it is theoretically possible to watch the system respond to fast perturbations from equilibrium- for instance a reheating laser pulse (as in some double-pulse LIBS setups) or optical pumping of a specific transition with a fast dye laser pulse.

Table 4-1. Thermal properties of elements, molecules and mixtures

Element	Ionization Energy (eV)	Thermal Conductivity (cal*s ⁻¹ *cm ⁻¹ *K ⁻¹)	Specific Heat (cal*mol ⁻¹ *K ⁻¹)	Molecular Weight (g/mole)
O ₂	12.1	63.6	7.01	32.00
N ₂	15.6	62.4	6.98	28.01
Ar	15.8	42.6	4.95	39.95
He	24.6	360.4	4.96	4.00
Al	6.0	2300		26.98
air				28.97

[Adapted from Weyl, G. M., Physics of Laser-Induced Breakdown: An Update. In *Laser-Induced Plasmas and Applications*, Radziemski, L. J.; Cremers, D. A., Eds. Marcel Dekker, Inc.: New York, 1989; pp 1-67.]

Table 4-2. Time-resolved extended LTE calculations

	time (ns)	$d(n_e)/dt$ [$\text{cm}^{-3}\text{ns}^{-1}$]	n_e (cm^{-3})	τ_{ne} (ns)	τ_{relax} (ns)	time (ns)	$d(T_e)/dt$ [K/ns]	T (K)	τ_{Texc} (ns)	τ_{relax} (ns)
Air	16-32	-3.88E+16	7.99E+17	21	10	8.4-25.1	-132	9275	70	9
	40-56	-1.08E+16	2.49E+17	23	107*	33.4-92.0	-39	6464	166	598*
	-	-	-	-	-					
Argon	16-32	-2.68E+16	9.55E+17	36	5	9.4-28.1	-117	10514	90	5
	40-56	-1.34E+16	4.82E+17	36	27	37.5-122.0	-22.2	7835	352	73
	64-80	-5.13E+15	2.59E+17	50	75*					
Helium	8-32	-1.81E+15	9.42E+16	52	92*	9.4-28.1	-142	9198	65	88*
	40-56	-1.15E+15	3.92E+16	34	803*	37.5-84.4	-24.5	6539	266	2196*
	64-80	-4.75E+14	2.17E+16	46	2425*					

Calculated for a 3.33eV transition. (–) indicates regions where no data was available. Values showing departure from LTE are indicated with (*).

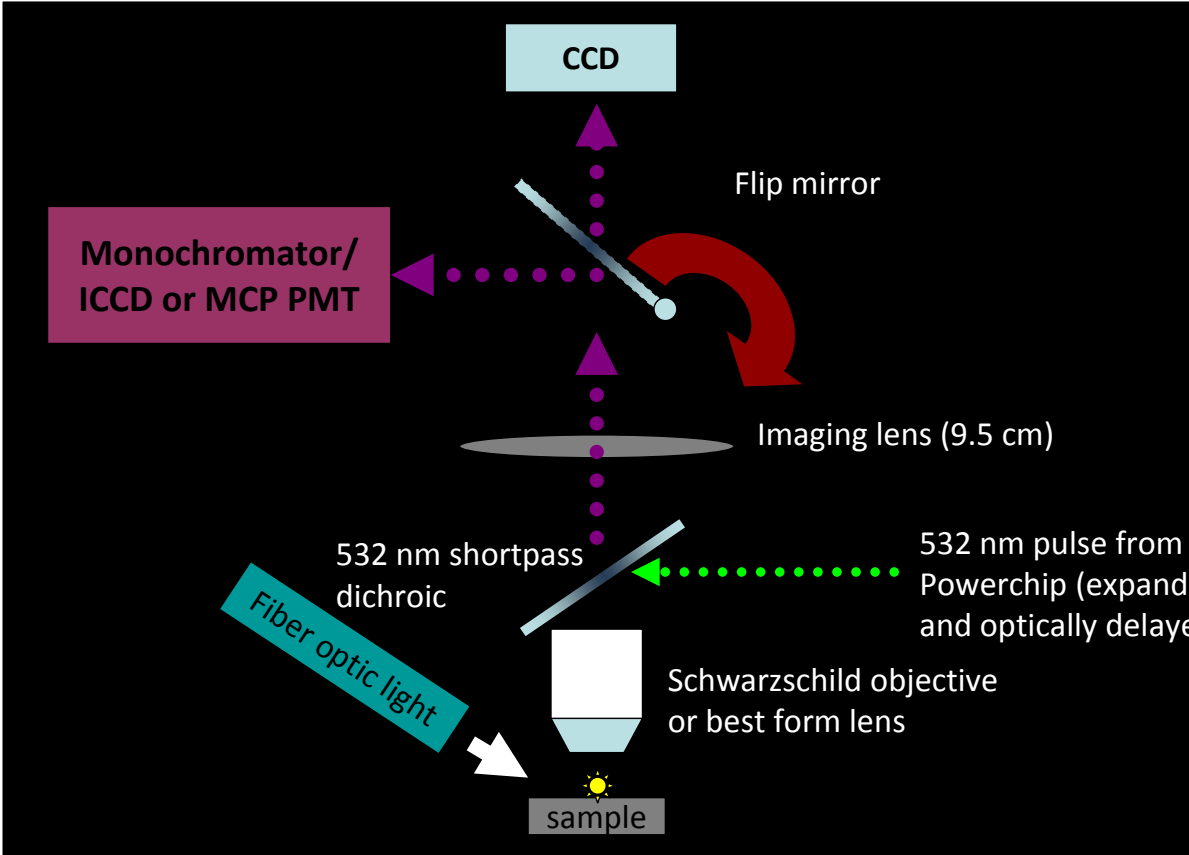


Figure 4-1. LIBS microscope arrangement.

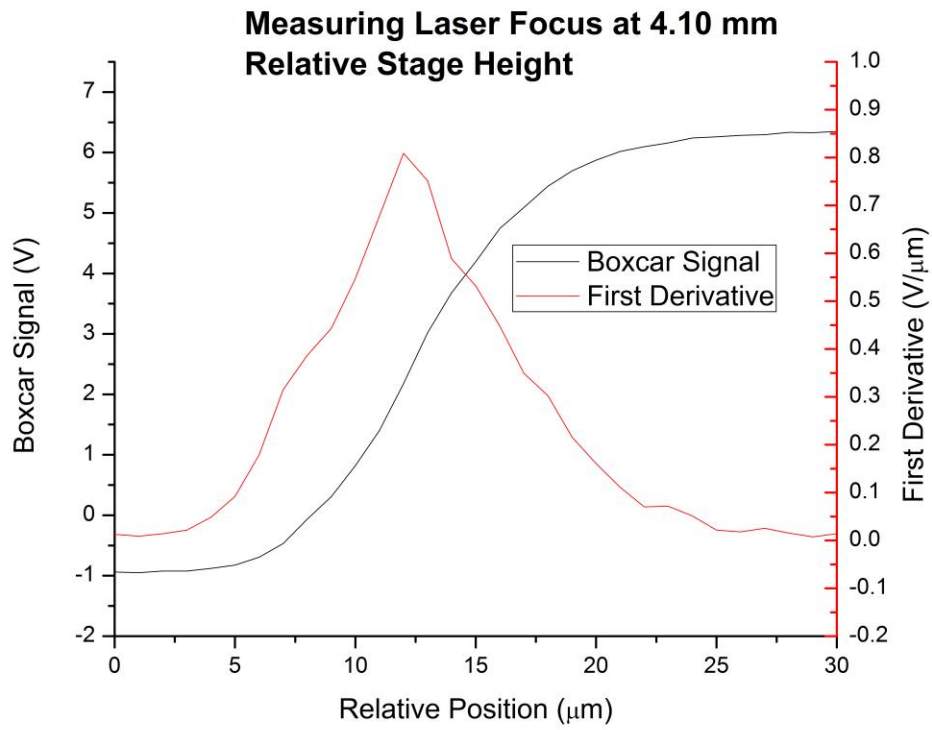


Figure 4-2. Knife-edge profiling of laser focus.

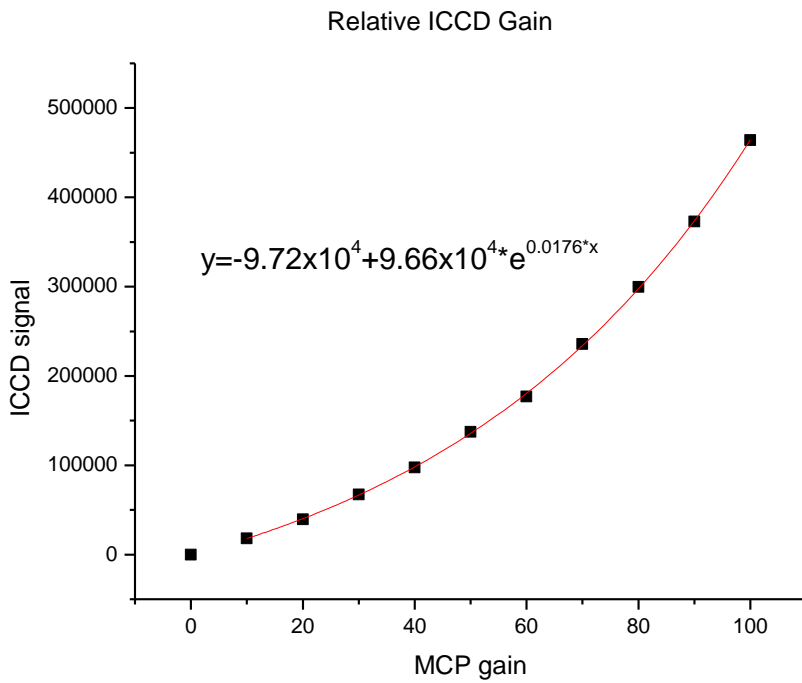


Figure 4-3. Calibration of relative ICCD gain.

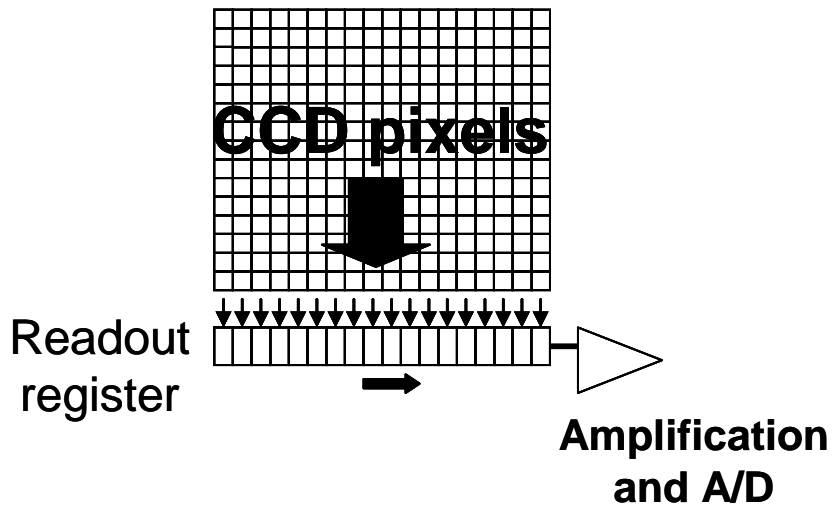


Figure 4-4. CCD readout procedure.

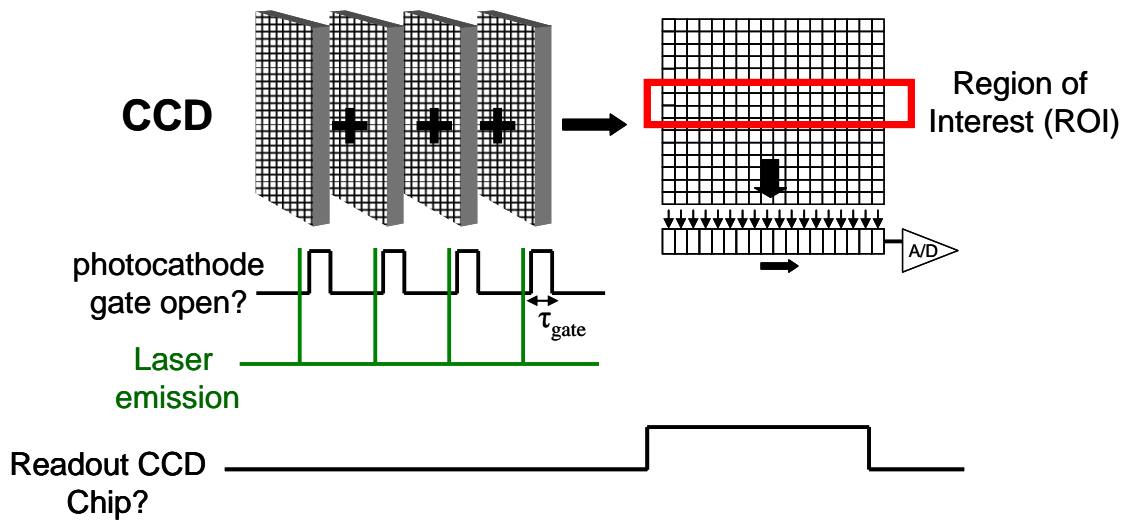


Figure 4-5. Experimental timing with on-chip integration and readout register binning of region of interest.

Shots to Drill through 0.001" Al Target with 532 nm Powerchip

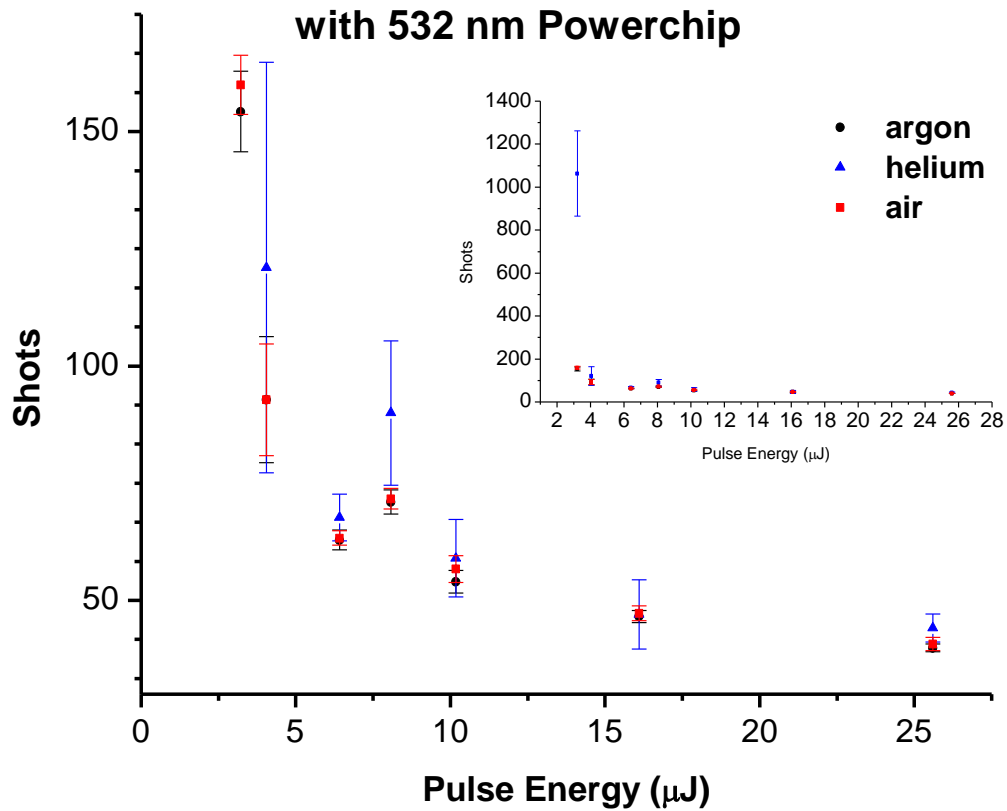


Figure 4-6. Shots required to drill through 0.001" aluminum sheet using 532nm laser. Error bars are 95% confidence intervals calculated from $n > 5$ measurements. Note that $1 \mu\text{J}$ corresponds to $12 \text{GW}/\text{cm}^2$.

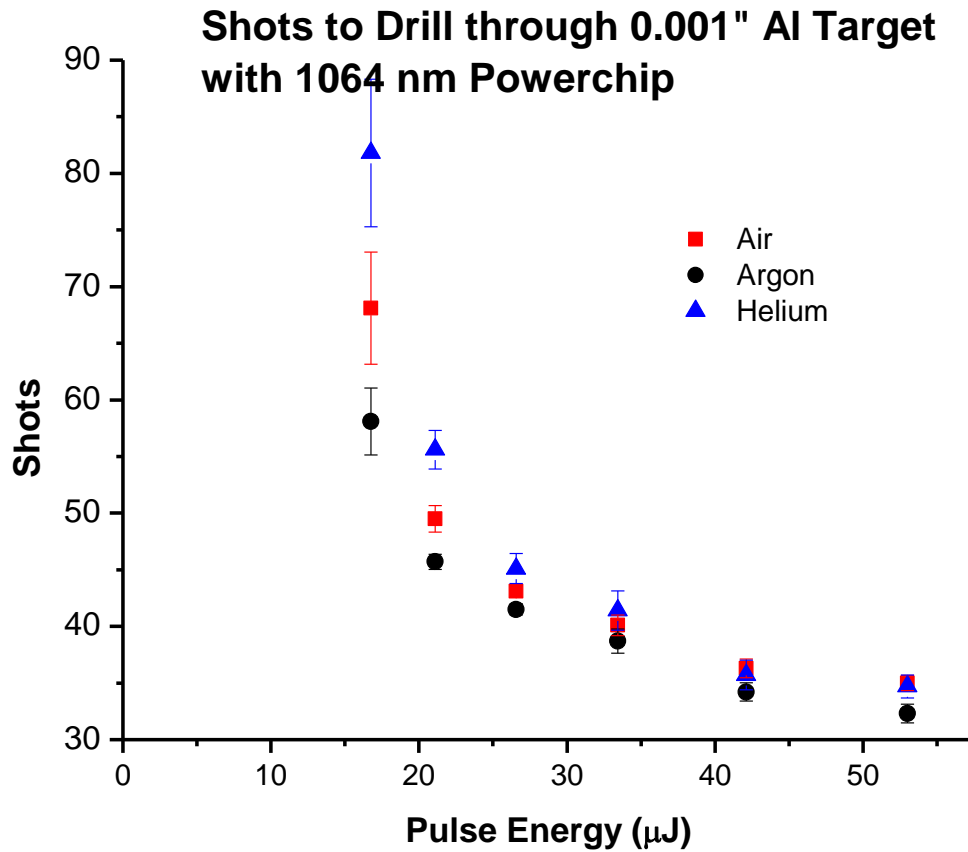


Figure 4-7. Shots required to drill through 0.001" aluminum foil using 1064nm powerchip laser. Unpublished data provided by Ebo Ewusi-Annan. Note different scaling from previous figure. Error bars are 95% confidence intervals. Note that $1\mu\text{J}$ corresponds to $12\text{GW}/\text{cm}^2$. [Ewusi-Annan, E., Merten, J., 2011]

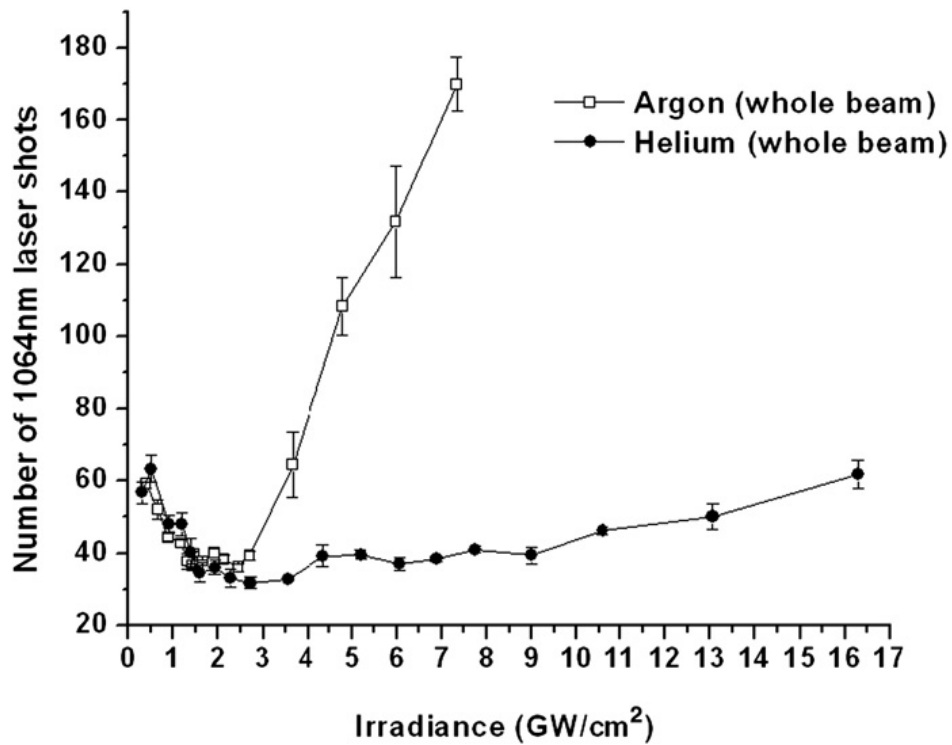


Figure 4-8. Laser shots required to drill through 0.002" brass shim stock with 1064 laser. [Used with permission from Gravel, J.-F. Y.; Boudreau, D., Study by focused shadowgraphy of the effect of laser irradiance on laser-induced plasma formation and ablation rate in various gases. *Spectrochimica Acta Part B: Atomic Spectroscopy* **2009**, *64* (1), 56-66.]

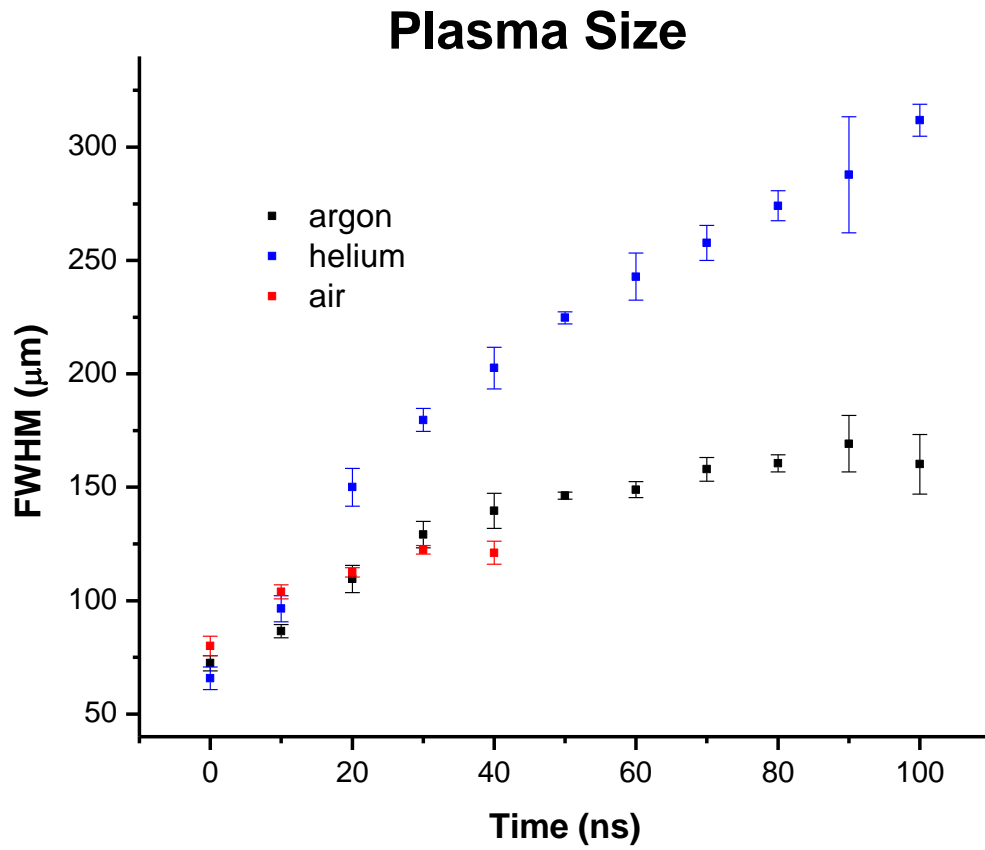


Figure 4-9. Time resolved plasma diameter taken from H α line emission images. Note that earliest two points use a 2ns gate, while later points use an 8ns gate. Error bars are one standard deviation.

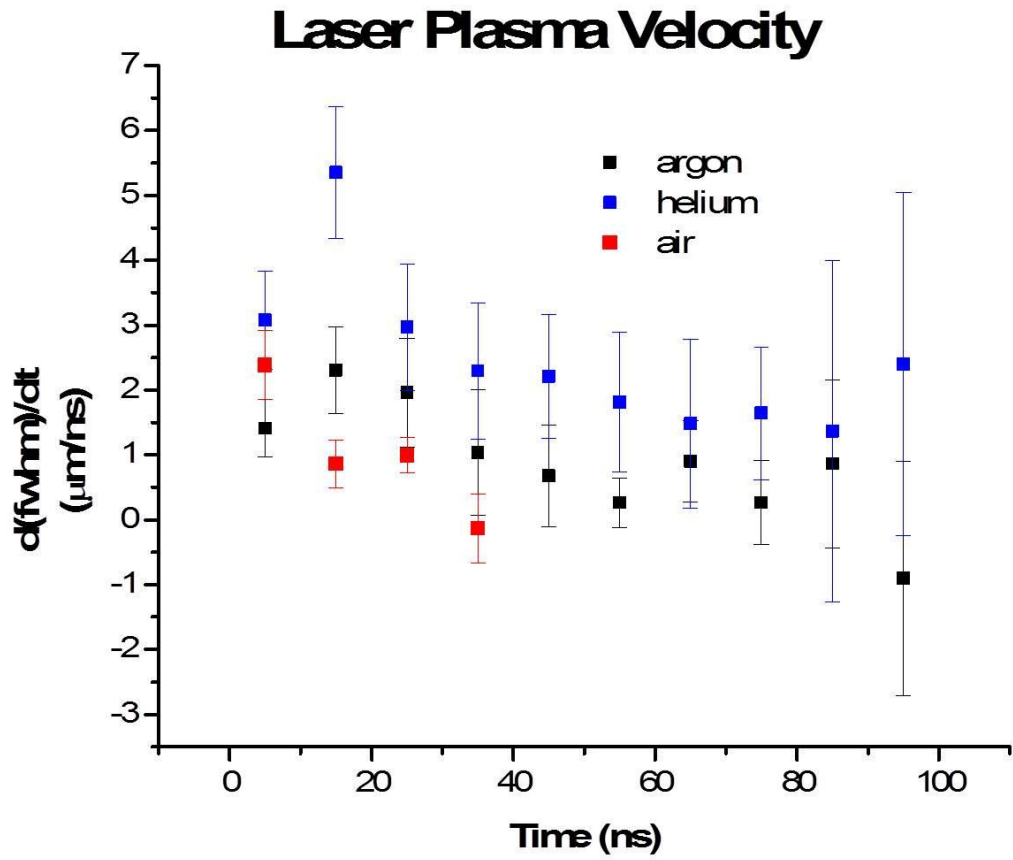


Figure 4-10. Time resolved plasma expansion velocities measured from H α images. Error bars are one propagated standard deviation.

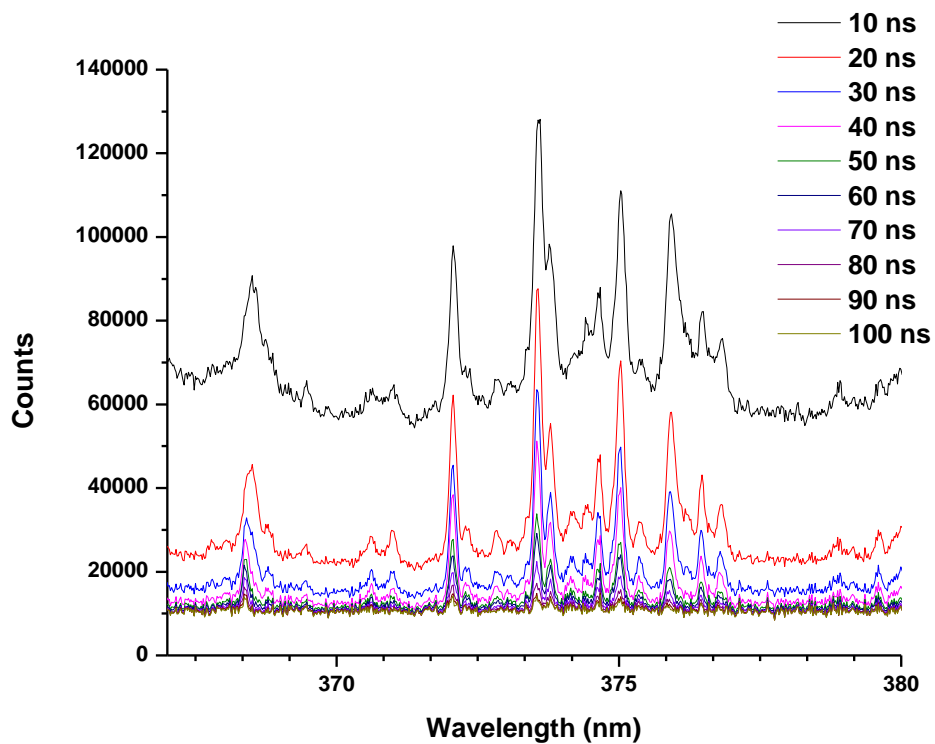


Figure 4-11. Low-resolution spectrum of Fe lines in aluminum standard b8.

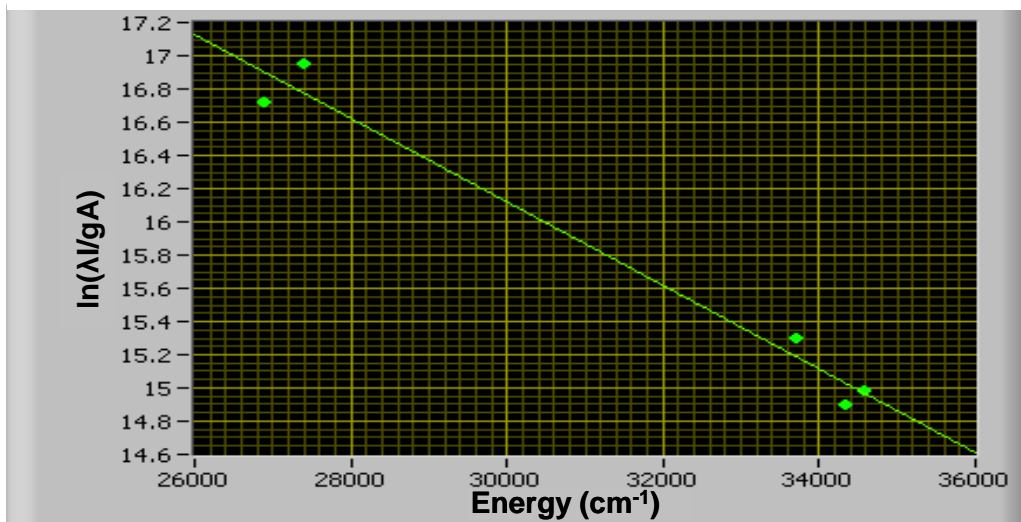


Figure 4-12. Representative Boltzmann plot for temperature measurements using Fe lines. Note that $1\text{eV}=8067\text{cm}^{-1}$.

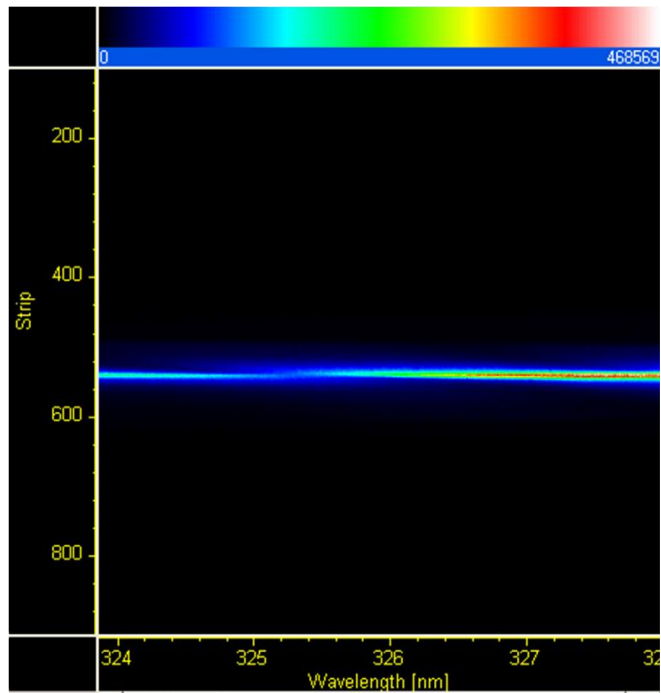


Figure 4-13. Variation of optical response across face of CCD. Note color scale (relative response) at top of figure.

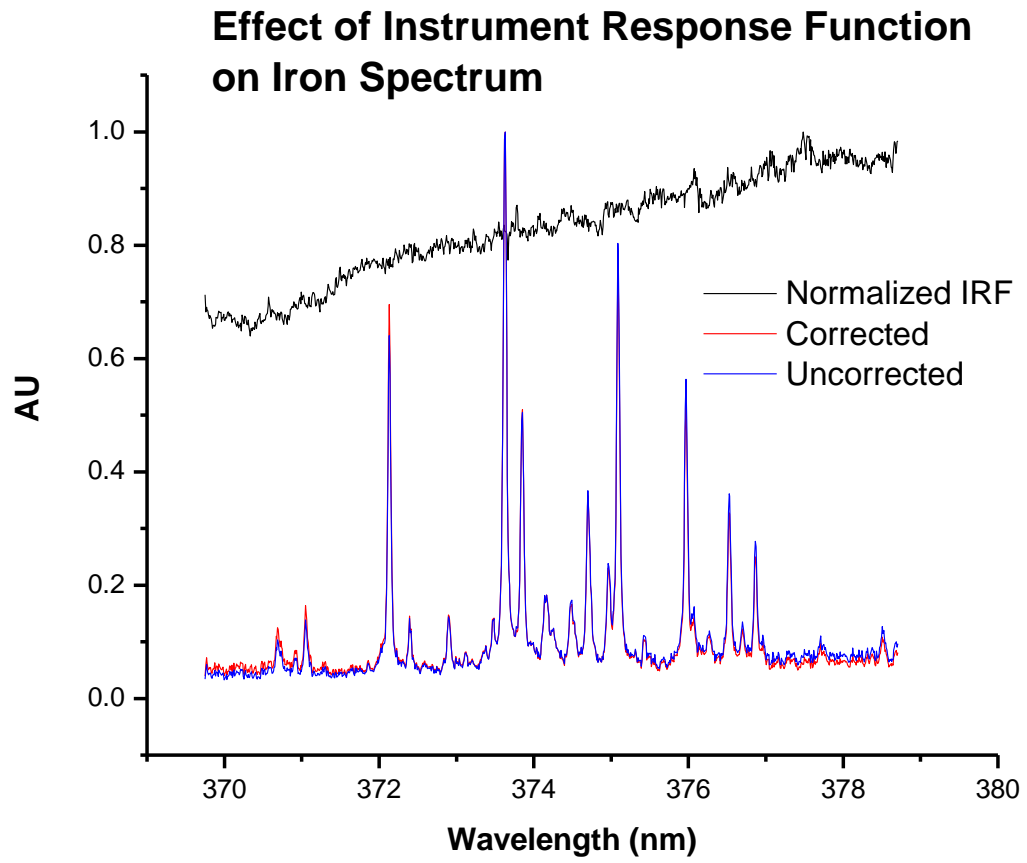


Figure 4-14. Effect of instrument response function (IRF) correction on iron emission lines in LIBS plasma.

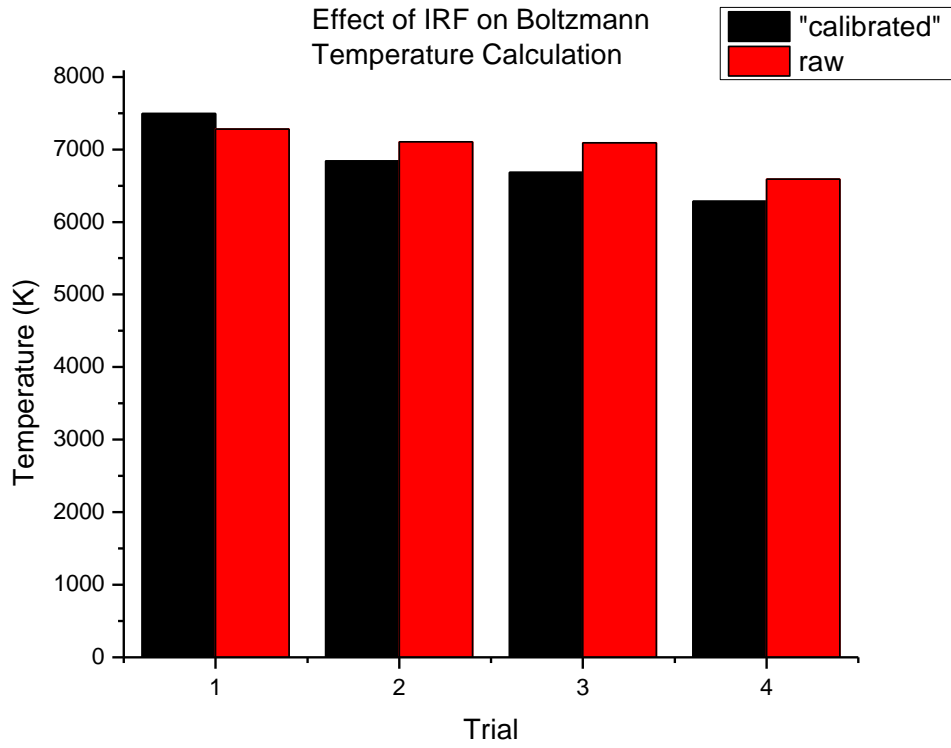


Figure 4-15. Effect of IRF on calculated excitation temperature.

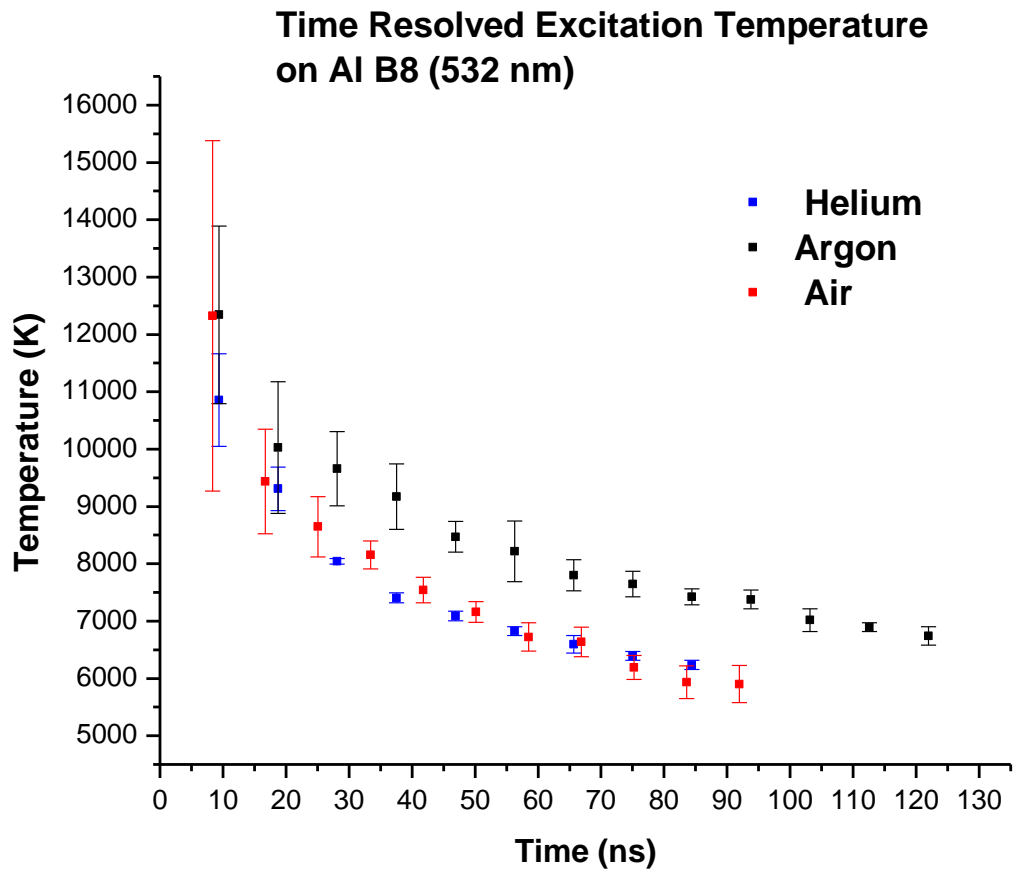


Figure 4-16. Time resolved temperatures under different atmospheres. Error bars represent one standard deviation from n=4.

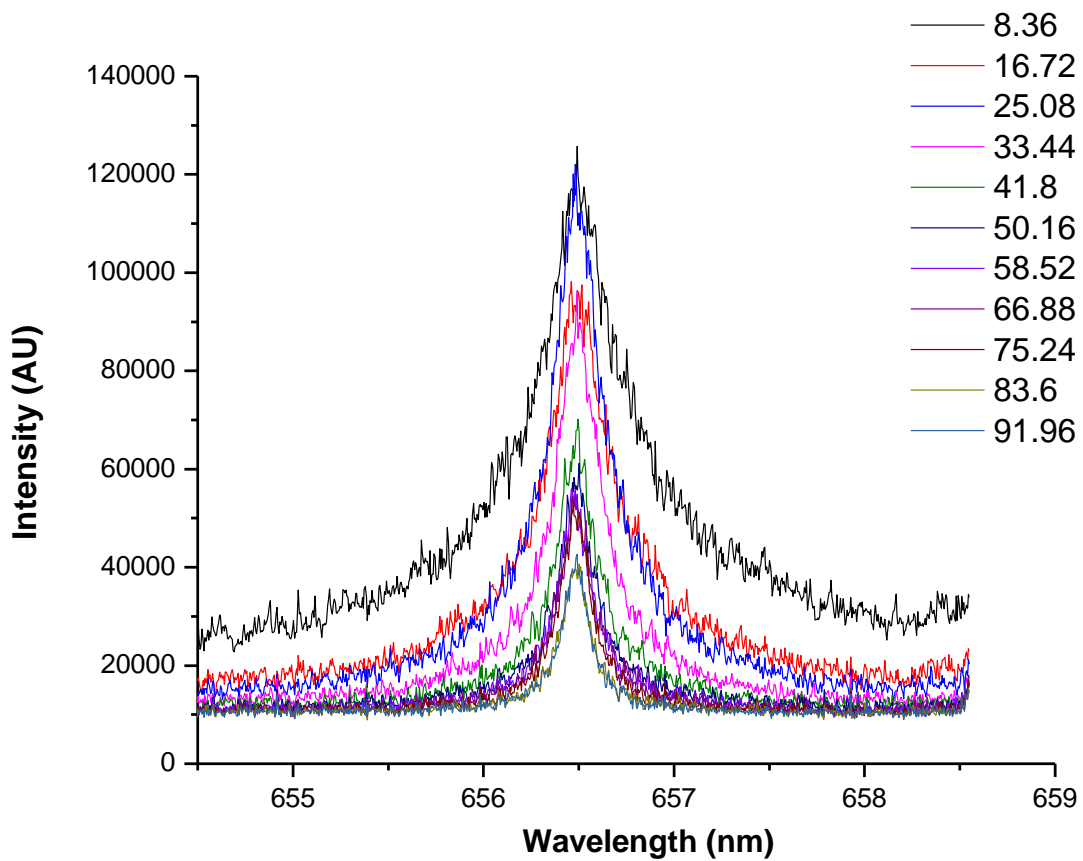


Figure 4-17. Time-resolved H α line profiles from plasmas formed on aluminum under helium. Times are indicated in upper right corner of figure. ICCD gate was 8ns.

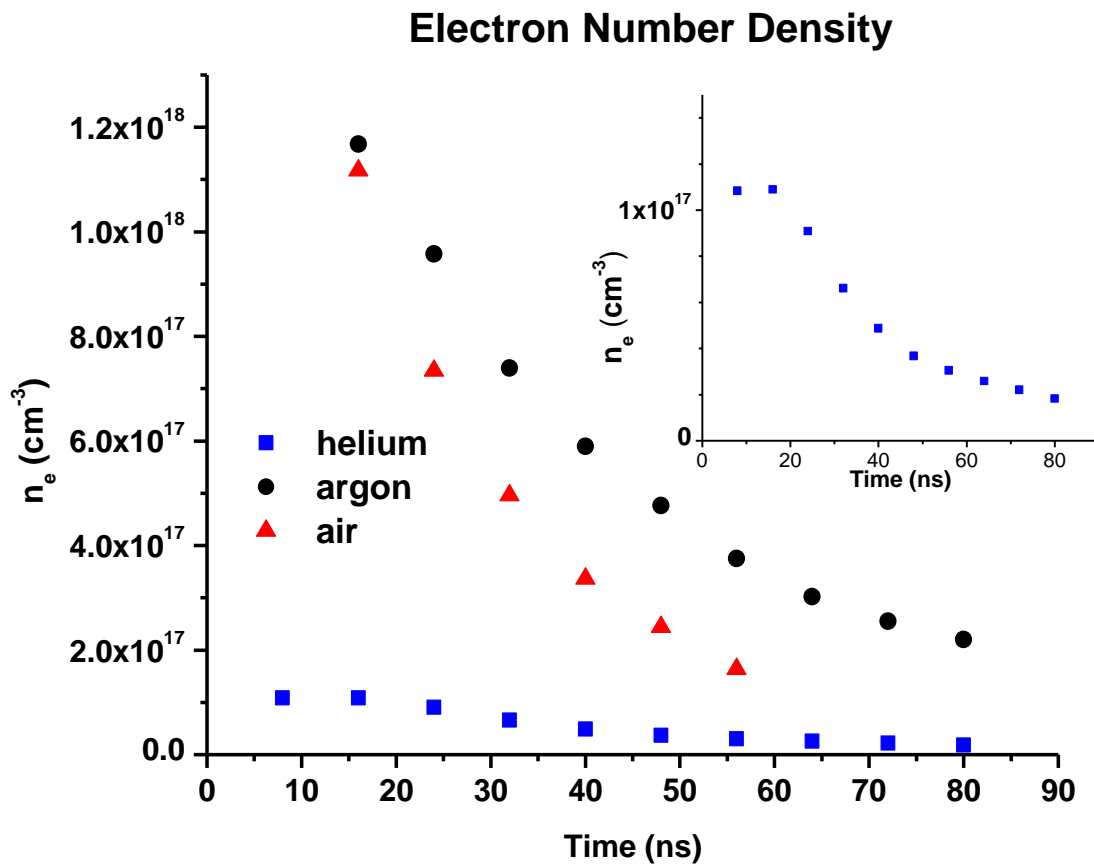


Figure 4-18. Time-resolved aluminum plasma electron number densities in various atmospheres. Inset shows blow-up of helium data to better show helium behavior.

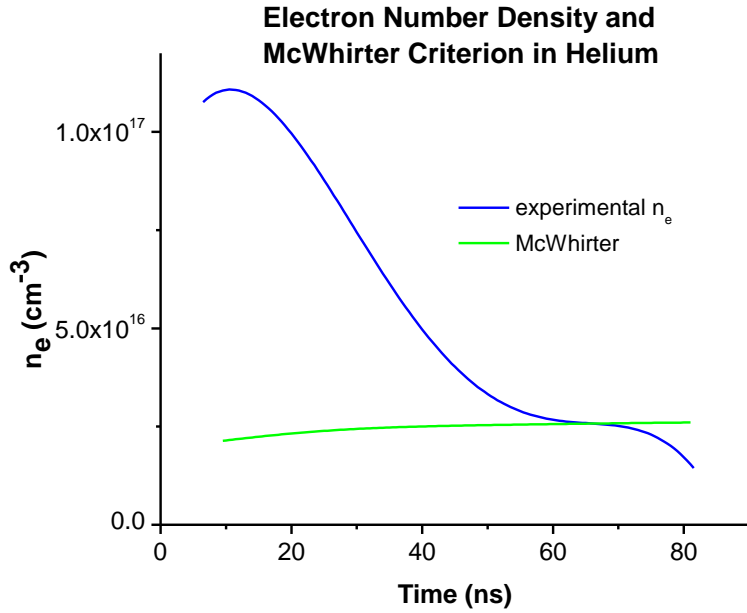


Figure 4-19. Comparison of experimental electron number density under helium as a function of time and the corresponding value required to fulfill the McWhirter criterion.

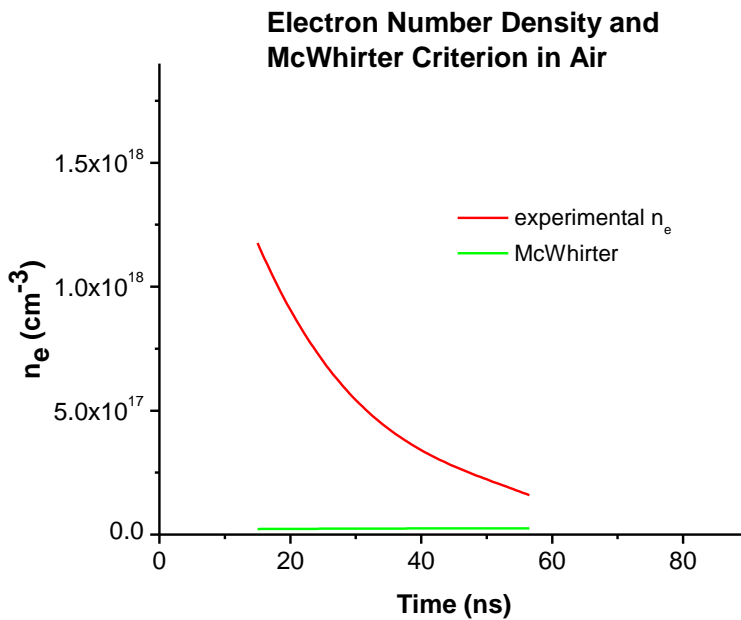


Figure 4-20. Comparison of experimental electron number density under air as a function of time and the corresponding value required to fulfill the McWhirter criterion.

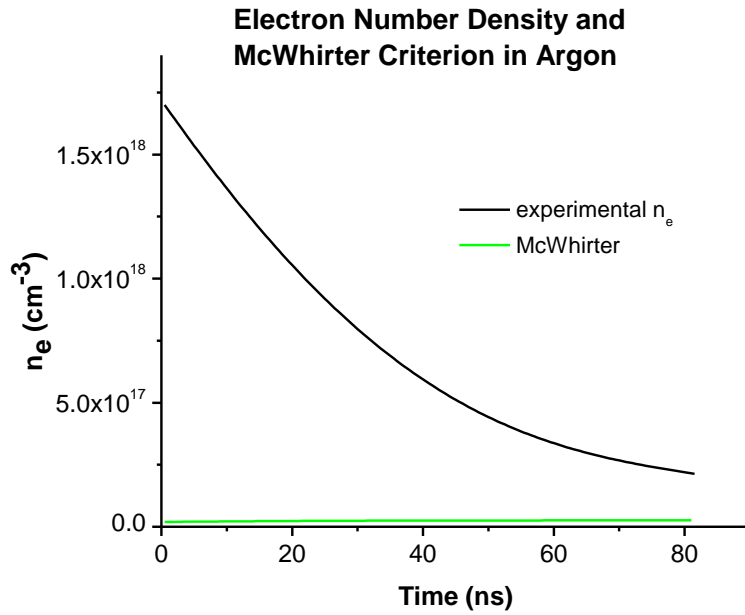


Figure 4-21. Comparison of experimental electron number density under argon as a function of time and the corresponding value required to fulfill the McWhirter criterion.

CHAPTER 5 SIGNAL TO NOISE RATIO CONSIDERATIONS IN POWERCHIP MICROLIBS

Figures of Merit

Although LIBS, and specifically microchip LIBS, touts simplicity, microdestructiveness and portability among its chief advantages, traditional figures of merit (FOM), such as signal to background ratio (S/B), signal to noise ratio (S/N), precision, and limit of detection (LOD) remain important. Chapter 4 provided the beginnings of a physical understanding of the plasma. In Chapter 5, figures of merit are measured and discussed in terms of the physics of the plasma and the instrumentation.

Because of the laser jitter and the electronic requirements for gating ICCD's time resolved measurement adds significant complexity and expense to the experiment. In this section, the possible benefits of detector gating within microchip plasma evolution are explored, as well as the general FOM. Because the plasma continuum generally decays more rapidly than neutral line emission, S/B ratio generally improves with plasma gating in LIBS measurements. Although S/B is often quoted as a surrogate for limit of detection, the two are only inversely related to the extent that background noise is a linear function of the background intensity. The functional dependence of background noise on the different portions of the background signal (continuum photons or CCD dark charge) must be determined in order to minimize limits of detection.

Background noise may also come into play in the precision of measurements. While the limit of detection is a function of background noise alone (and sensitivity), the precision of a given measurement can be a function of background noise or signal noise. The issue is complicated in situations where the two may even be correlated, as one could imagine would be the case in LIBS where plasma evolution can determine

both the atomic excitation temperature and the electron number density. As plasma initiation is a highly non-linear process, significant variability in these parameters is expected. Attempts to decrease uncertainty in the signal using internal standards, acoustic normalization, temperature measurements, etc. require understanding the precision-limiting noise and any potential correlations. Blind application of normalization techniques in LIBS can actually decrease precision, for instance in the case where analyte and internal standard signal are both signal shot noise limited.

Characterizing noise is particularly difficult on a microscopic LIBS setup, as employed in this work, both because of difficulties in sample positioning and because of sample heterogeneity. In fact, there are very few standard samples that are known to be homogenous on a $\sim 10\mu\text{m}$ length scale, and none of them were available or applicable in this experimental configuration. The data presented in this chapter is generated on a series of aluminum standards designed for a LIBS round-robin test. The compositions of the samples can be found in Appendix B. These standards are not, however, known to be microscopically homogenous-- a fact that must be considered when examining the data.

In order to minimize noise from sample preparation and presentation, samples were carefully prepared. After fly-cutting to flatness, they were sanded with a progression of sandpaper grits (320, 400, 600). In between measurements, they were re-sanded as required. Samples were registered against the bottom of a custom-made sample holder and randomly rastered by hand. This was necessary as repeated probings of the same spot modify the sample, which leads to variation in plasma parameters. The sample rastering is a potential source of noise, given that it could not

be well-regulated. Additionally, the likelihood of ablating the same area twice increases with the number of laser shots.

The laser energy stability was also characterized. Although the spectra in this chapter were taken with the laser running at the factory-optimized 1kHz, data from several different repetition rates are presented in Figure 5-1. At the factory-optimized 1kHz, laser stability is 0.5%. Interestingly, the laser energy is slightly higher at 10Hz, with a modestly higher instability. As the plots at 400 and 1500Hz show, the laser stability can suffer at arbitrary frequencies and the pulse energy distribution becomes non-normal. These measurements were made at the end of the delay line (the entrance to the LIBS microscope), and also represent any noise introduced by the delay line. This optimal stability is significantly better than the 2% RSD expected in new flashlamp lasers, especially when one considers that the data in Figure 5-1 was taken after 6 years of daily experiments with the powerchip laser without any maintenance (except replacing the on/off switch).

Precision and Systematic Error

Because the iron lines discussed in Chapter 4 offer so much information about the plasma, a calibration curve for iron was constructed with the 371.9nm iron emission line. (Figure 5-2) It should be noted that each spectrum contained 1000 shots; this is not a single-shot noise study. Twenty-one different standards were included, with varying compositions (Appendix B), some of which were visually distinct from the others. Measurements were made under helium because it offers the narrowest emission lines in this congested spectral region. The curve does show linearity over more than an order of magnitude- extending to more than 1% Fe. (Figure 5-2) This alone is a surprising result given that this line originates in the ground state. Note that the s4

standard was treated as an outlier and excluded from analyses. Figure 5-2 generally indicates either a significant matrix effect or poor precision, with a $R^2=0.930$. Both poor precision and matrix effects would show themselves in the correlation coefficient. Further tests are needed to determine which effect is responsible.

Boltzmann plots were also constructed from the three spectra collected from each sample. As these spectra represent the time integrated emission from 50-200ns after the laser pulse, the temperatures and the line intensities are weighted toward the earlier part of the gate, although Figure 4-16 indicates that the plasma cooling is slowing by 50ns. Comparison of Figures 4-16 and 5-3 does show a systematic discrepancy in temperature not explainable by the longer gate used in the calibration curves. This may be due to variations in laser irradiance resulting from day to day fluctuations in the delay line alignment.

The graph of normalized residuals vs. temperature in Figure 5-4 does not seem to show a correlation between the two, though it should be noted that a linear correlation would not be expected, given the exponential dependence of emissivity on temperature (Equation 3-3). In a further attempt to attribute some of the error, a calibration plot (not shown) was also constructed with the 376.3nm iron line. The residual at each point on each calibration plot was normalized with the iron concentration at that point. The weighted residuals were plotted against each other in Figure 5-5. The residuals are highly correlated, suggesting that ablation volume or plasma wander account for the residuals in the calibration plot. The “outliers” in Figure 5-5 (mn397, n1075a, m7) are necessarily the result of systematic error and may signal error in determining true peak

areas (e.g. baseline or general spectral interference problems), and show the importance of matrix-matched standards in LIBS.

In order to better understand the precision and noise source, the spectral noise and RSD were investigated for a single sample. Array detectors such as CCD's, ICCD's and diode arrays allow simultaneous measurement of the signal and the background. The complete equation for the summation of signal and background noise is given by:

$$\sigma_{total}^2 = \sigma_{back}^2 + \sigma_{analyte}^2 + 2\theta\sigma_{back}\sigma_{analyte} \quad (5-1)$$

where σ_{total} is the standard deviation of the total signal measured at the center of the peak, σ_{back} is the standard deviation of the background, $\sigma_{analyte}$ is the standard deviation due to the analyte signal, and θ is the correlation coefficient. If $\theta=1$, the noises are said to be correlated, if $\theta=-1$, they are said to be anticorrelated. In the case that the noises are uncorrelated, $\theta=0$, and Equation 5-1 reduces to the more often seen form. In LIBS, the limiting background noise is typically noise in the continuum. As the electron number density and the radiance of a spectral line are both functions of temperature, it is easy to see that continuum and line intensity could be correlated. Unfortunately, it is not possible to separate the two.

Plots of spectral standard deviation and RSD were prepared by measuring multiple spectra from an aluminum sample over the course of a few minutes. The sample (aluminum standard 1075) was not resurfaced between individual spectra. Each spectrum consisted of 300 on-chip integrated plasmas, with the ROI binned in the readout register (Figure 4-5). One hundred such spectra were saved and then analyzed with a custom-written Labview program which calculated pixel-by-pixel average,

standard deviation and RSD. The spectral region around the copper 324.7 and 327.4nm line was chosen for its relative simplicity and the diagnostic potential of the two closely spaced transitions originating at the same upper state energy and terminating in the ground state. The sample is certified as containing 0.007% copper by weight, so the lines are expected to be extremely optically thin. Later studies showed that this concentration is still above the LOD for copper.

By blocking the laser, the “dark” contribution to the spectral standard deviation (arising primarily from thermal electron accumulation on the CCD and readout noise) was measured at 17 counts, though a few columns (those containing “hot pixel” defects on the CCD) showed substantially higher noise and were excluded from analyses. Off-peak standard deviations from the plasma background in Figure 5-5, on the other hand, were approximately 300 counts, in comparison to which the dark contribution should be negligible. The standard deviation plots indicate that the analytical precision at even this modest concentration is limited by noise in the atomic emission rather than the continuum.

Limit of Detection

Until now, the value of gating within individual powerchip laser pulses has remained an open question. Where precision is limited by noise in the analytical line at concentrations well above the limit of detection, the LOD itself is limited by noise in the background. As the background bremsstrahlung and free-bound recombination continuum decreases faster than atomic emission with increasing delay, one could expect that the signal to noise ratio would improve as the gating delay is increased decreasing the background signal until the point that the analytical signal becomes so

weak that detector dark charge noise and readout noise approach the level of the continuum shot noise, at which point the SNR would begin to decrease.

To put to rest the question of gating in microchip analysis, a series of S/N determinations were made on the copper 327.4nm line. The ICCD gate was controlled in such a way that the camera gated off at the same time in each series of spectra, but the gate onset was varied in order to include varying amounts of the continuum. Three sets of ten spectra were taken at each gate onset. Spectra were dark-charge subtracted, then corrected for the instrumental response function. Background emission levels were determined using line-free areas on either end of the spectrum. In order to make the measurement more relevant to typical analytical measurements, where the peak is integrated, the peak and an adjacent line-free area were evaluated for signal and background signal to noise. Within each group of 10, the average peak signal and the average background standard deviation (of the integrated background signals) were calculated. Thus, the standard deviation represented noise between spectra, not pixel to pixel noise within a spectrum. This is an important distinction since the pixel to pixel standard deviation can represent shot noise, but not excess noise, and it is unclear which is the limiting noise. The peak integration parameters were not changed with slit width, which does confuse the issue slightly.

Figure 5-7 shows a clear trend to a lower S/N at early gate onsets. The S/N increases to a maximum for both slit widths, then begins to decrease more slowly. Contrary to the usual expectation, the wider gate gave the higher signal to noise ratio and a maximum that is displaced to longer gate onsets, though this may be a function of

the analytical signal filling in the peak integration bounds since these were not optimized for each slit width.

In theory, changes in the continuum result in an approximately equal fluctuation in signal at adjacent pixels- i.e. the noise is correlated. Thus, any excess noise (for instance changes in the continuum due to variations in plasma temperature) should be completely subtractable (in analogy to Equation 5-1). Ideally, background subtraction should remove any excess noise, leaving background shot noise to determine limits of detection, just as dark charge subtraction from CCD images removes flicker noise in the dark charge, leaving only shot noise. This, of course, assumes that the background noise is spectrally flat.

The variation in background noise as a function of background signal was checked on either side of the maxima in Figure 5-7 by attenuating the light with neutral density filters mounted inside the monochromator at the face of the ICCD. At long times, as seen in Figure 5-8, the slope of the log-log plot of noise vs. background signal has a slope of 0.5, indicating that shot noise dominates. As the dark noise is only 17 counts at any gate (dark noise is independent of gate width at high numbers of on-chip integrations) and the measured background noises are an order of magnitude higher, the dominant noise is clearly continuum shot. This result is very surprising, as it indicates that the analytical signal is decaying faster than the continuum, contrary to common expectation in LIBS measurements, and resulting in a “sweet spot” for signal to noise.

Several attempts were made to characterize the dominant noise in early gate onset measurements. In all cases, results were ambiguous, with low log-log plot

correlation coefficients, as exemplified in Figure 5-9, and intermediate slopes, which do not indicate shot or flicker noise. Some of the plots showed almost no trend with R^2 values near 0. This may be a case of undersampling of noise with a strong $1/f$ character, where long measurements are needed to achieve adequate representation. Other authors have reported that microchip laser limits of detection are dominated by $1/f$ noise.^{15d} Further tests are required to identify the source of this noise, however. Because the experiment was performed with a relatively long gate, there is a mixture of noise at early times- i.e. there is still significant continuum shot noise during the later portions of the gate, which may account for the intermediate log-log plot slope. Repeated attempts to characterize the noise were unsuccessful.

Because the powerchip LIBS plasma is known to wander in the course of the measurement, it was suggested that wander in the small, intensely-emitting plasma across the slit might account for the noise at early times. At later times, the plasma would be larger and more diffuse such that small changes in the relative position of the plasma would not affect the signal as much. In order to test this hypothesis, three different binning regions were established on the ICCD chip- one centered on the hottest central part of the plasma, where plasma wander would be expected to create a high level of $1/f$ noise, and two flanking regions, where the plasma is expected to be larger and more diffuse, and therefore less affected by any motion of the ablation spot relative to the spectrometer slit. The ROI's are shown in Figure 5-10 with reference to the plasma position. Once again, the S/N ratio was measured with a variety of gate start times, but with the gate-off fixed as in Figure 5-7. It was hypothesized that the plasma wander noise dominating the early continuum signal would be less in the

flanking ROI's, shifting the S/N maximum to earlier times. The experimental copper peak signal:background noise ratios are plotted by ROI in Figure 5-11. The noise in the sums of various spectra is also plotted.

Clearly, the S/N maximum does not shift to earlier times in the flanking ROI's, suggesting that plasma wander does not produce the limiting noise in gates incorporating the earliest part of the plasma. Figures 5-7 to 5-11, taken together leave us to the following conclusions:

- 1) There is an LOD benefit to gating within powerchip LIBS plasmas of as much as a factor of 10, and likely much more. There is an ideal gate position and width.
- 2) The limiting noise at early times is not strictly shot noise, while later gates are continuum shot noise limited
- 3) The limiting noise early in the plasma is not caused by the plasma image wandering across this spectrometer slit
- 4) At no time measured is the LOD determined by detector noise
- 5) The signal decays faster than the continuum shot noise at later times

Clearly, there is still a benefit to gating plasmas formed by these diminutive lasers. Their rapid sampling rate actually couples quite well with modern ICCD detectors when single shot data is not necessary. Considering the short insertion delay of modern ICCD's (~60ns), optically delaying the laser pulse to allow allow the optimum gate may not be necessary, although if the source of noise at early delays is identified and can be minimized with careful optimization of experimental parameters (spectral bandpass,

laser energy, sample presentation), a slight optical delay may be necessary as the optimal delays are shifted to earlier times.

Furthermore, as the LIBS community continues to embrace echelle spectrometers, where ROI binning is not possible, many of the findings in this chapter need to be revisited on a single-pixel level, where dark and readout noise are likely to be more significant.

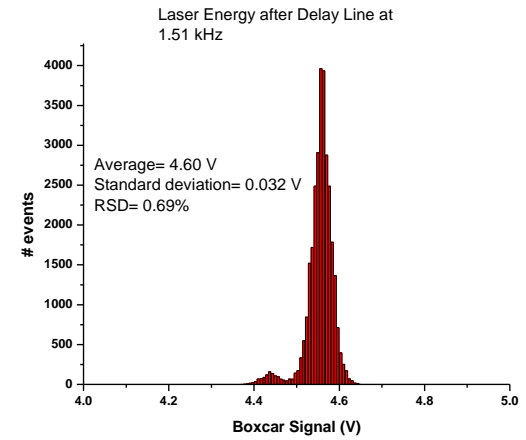
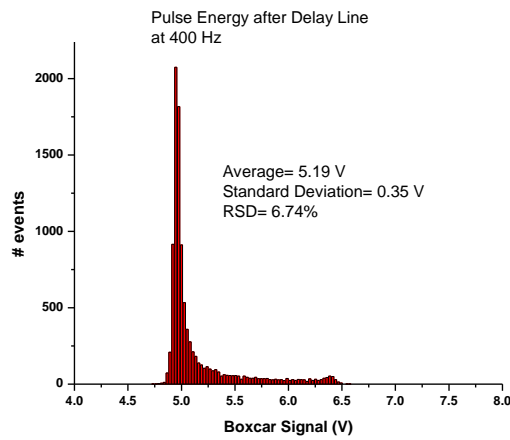
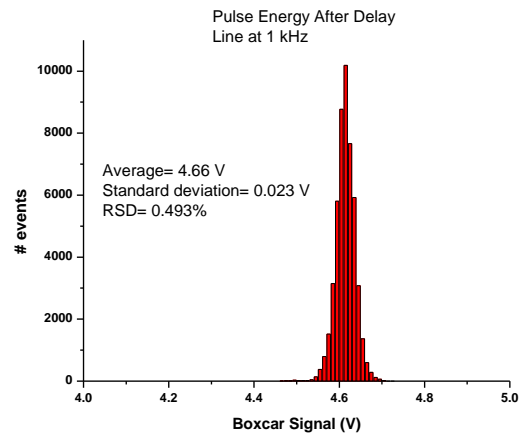
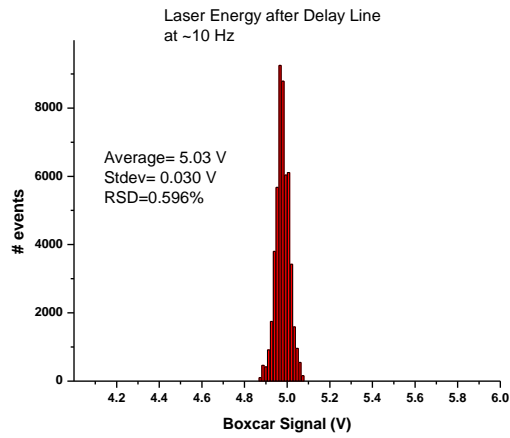


Figure 5-1. Laser shot energy distribution histograms recorded with a boxcar and an amplified photodiode.

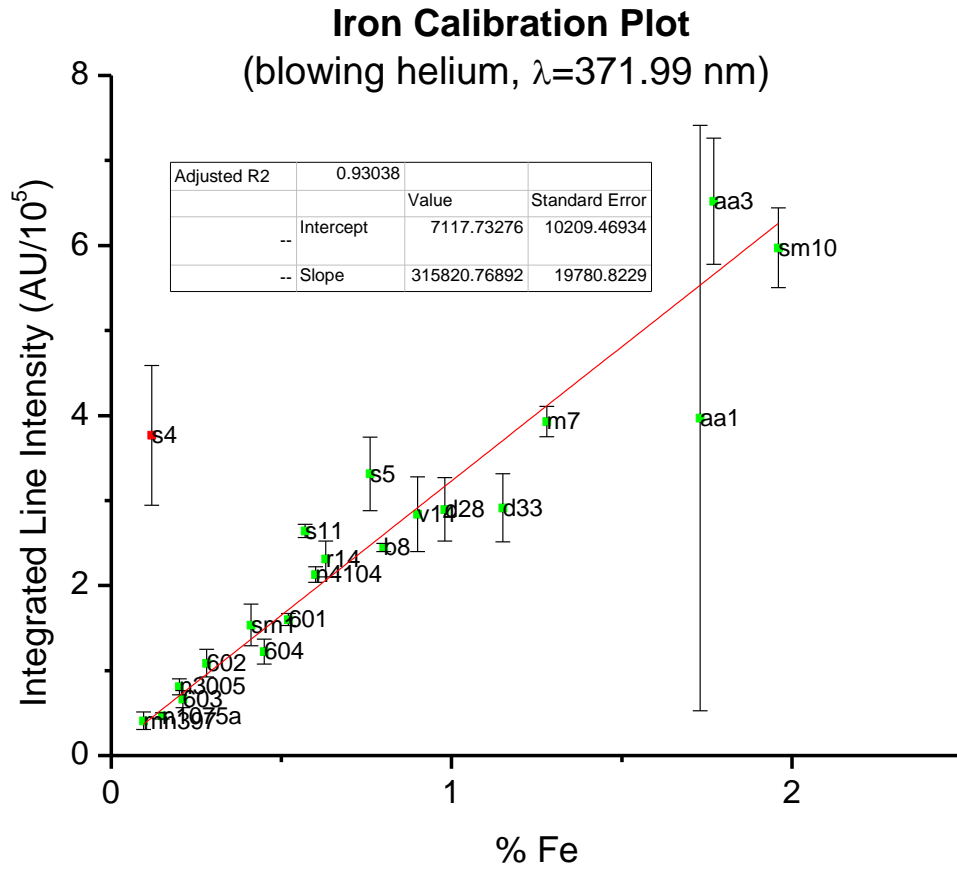


Figure 5-2. Iron calibration curve in aluminum matrix using 379.1nm. Error bars are one standard deviation at n=3.

Excitation Temperature

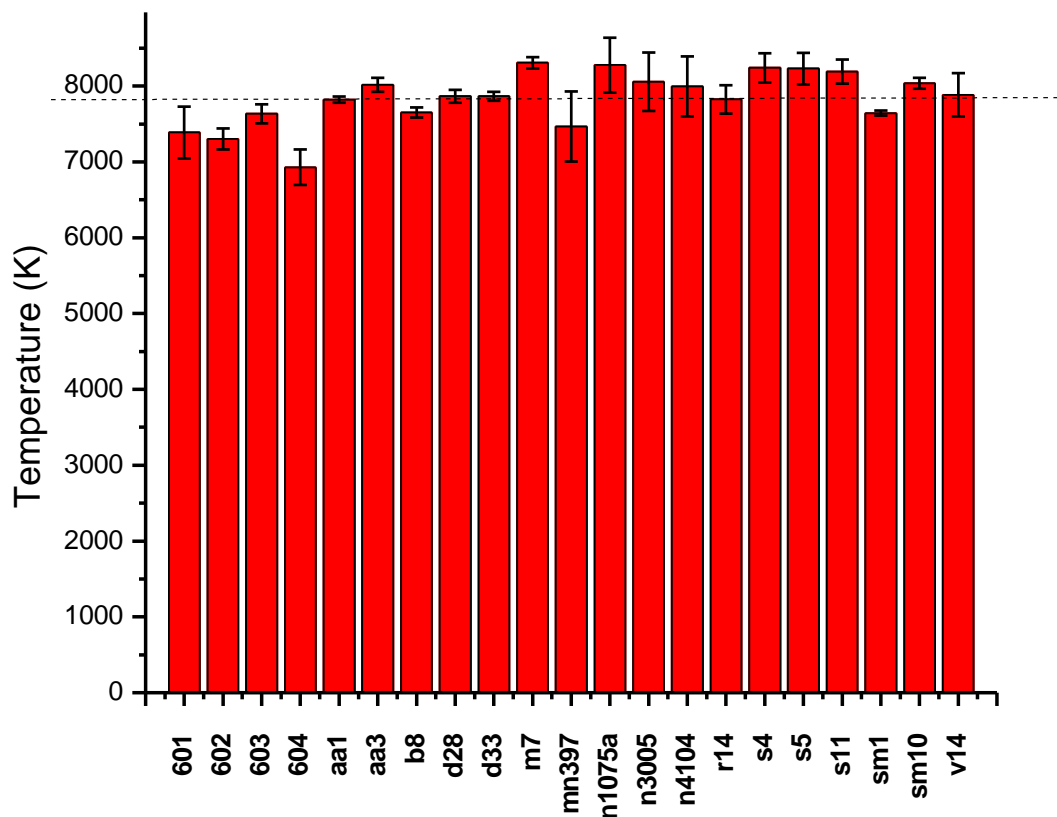


Figure 5-3. Excitation temperatures calculated from iron calibration curve data in aluminum samples. Excitation temperatures were determined with the iron lines tabulated in Appendix A. Error bars are one standard deviation at $n=3$. The dotted line indicates the average temperature.

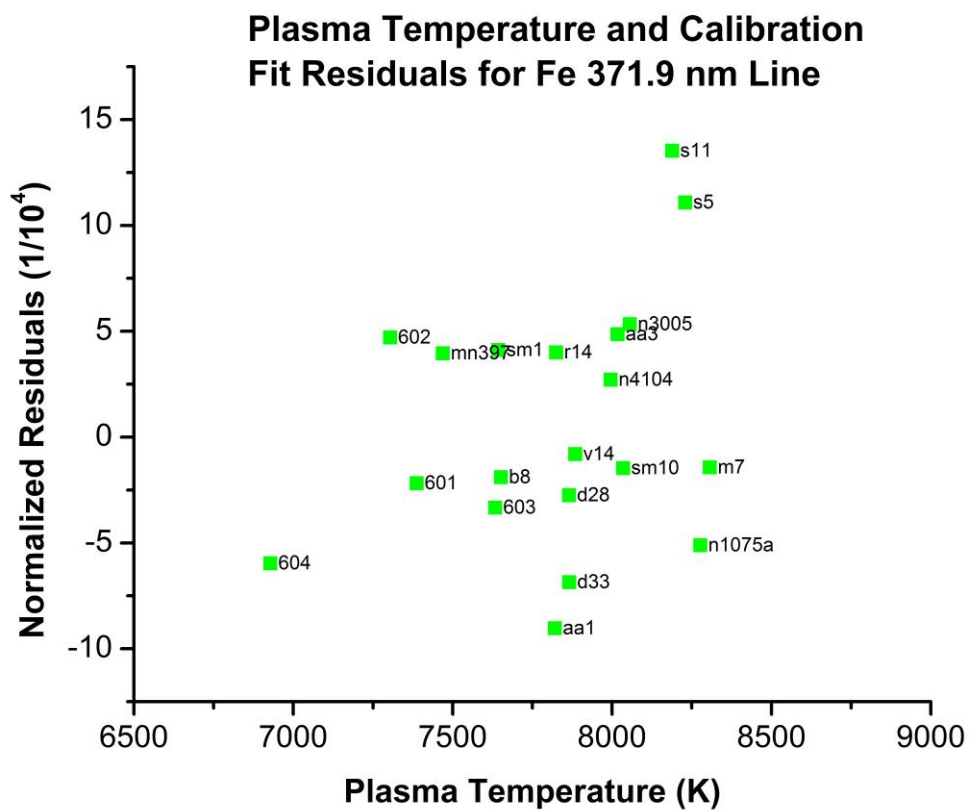


Figure 5-4. Excitation temperature and Fe calibration curve residuals.

Correlation of 376.3 nm Calibration Residuals with 371.99 Calibration Residuals

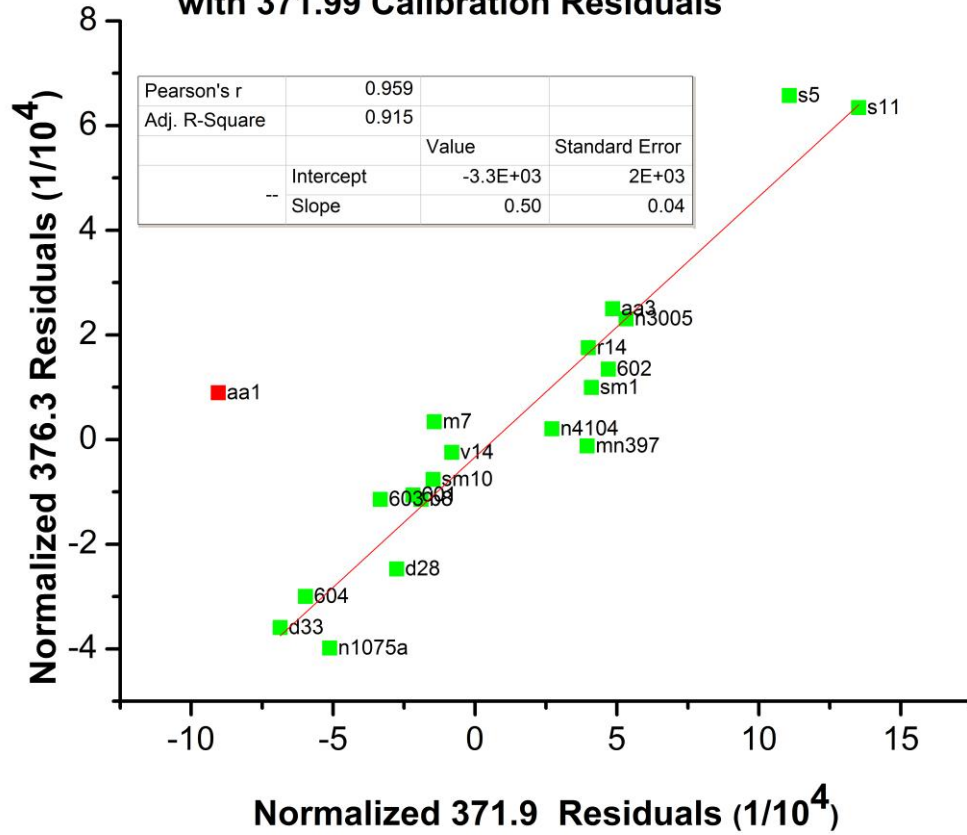


Figure 5-5. Correlation in residuals of iron calibrations using 371.9 and 376.3nm lines (in same spectra).

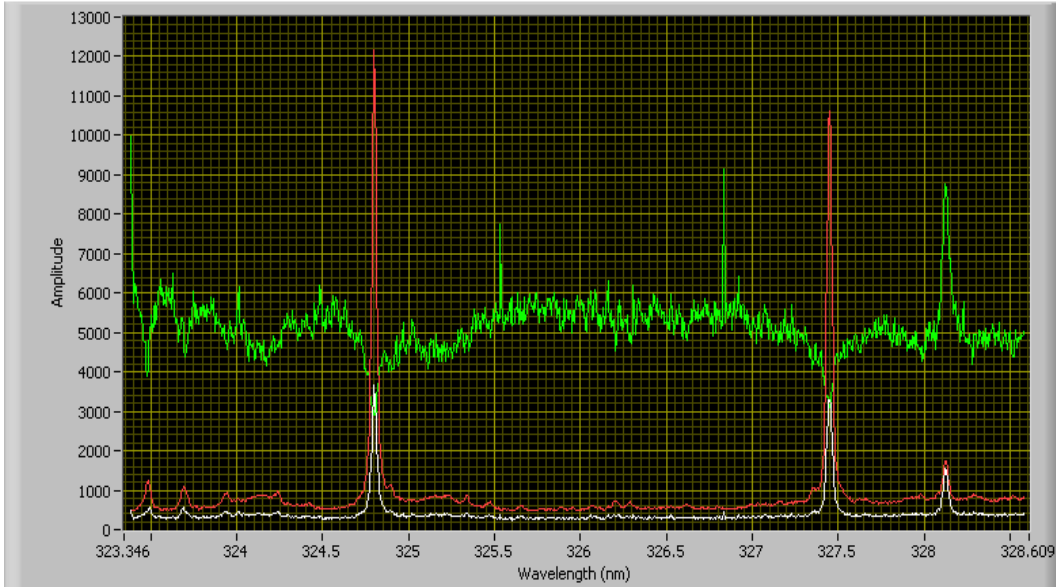


Figure 5-6. Spectral standard deviation and RSD of copper in aluminum. The red trace is signal mean, the white trace is standard deviation and the green trace is RSD (parts per 10^4).

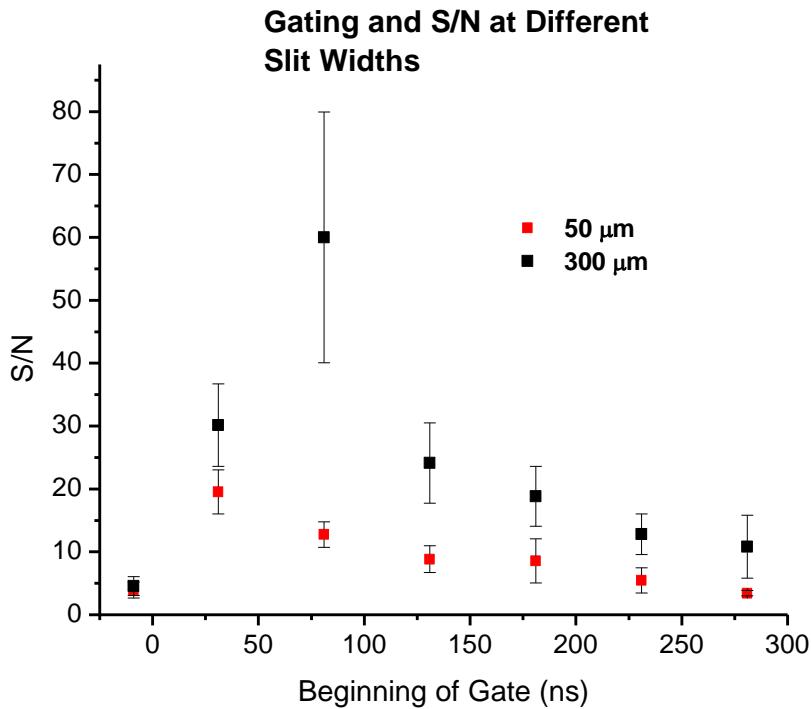


Figure 5-7. S/N of Cu 327.4nm line vs. gate on delay- error bars are one standard deviation from $n=3$. Peak areas and equivalent baseline widths were used. The target was aluminum sample n1075.

Limiting Noise at Late Gate (181-531 ns post-laser)

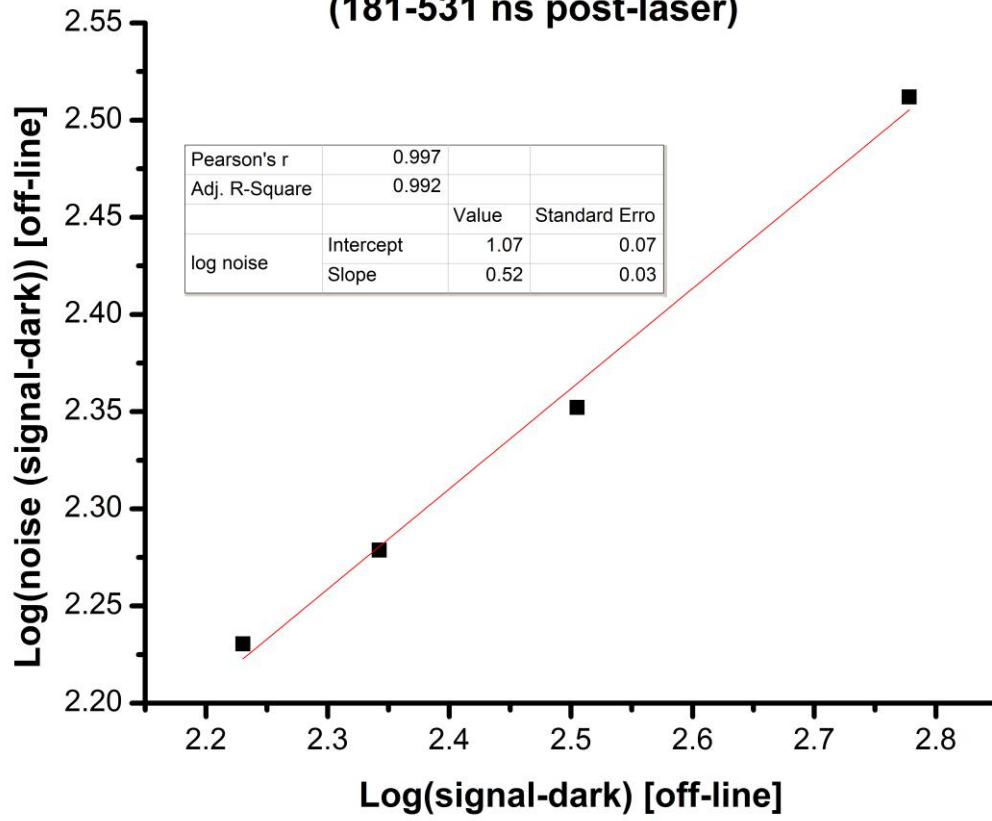


Figure 5-8. Background noise as a function of background signal at late gate onsets in aluminum sample n1075.

Gating on 11 ns post-Laser

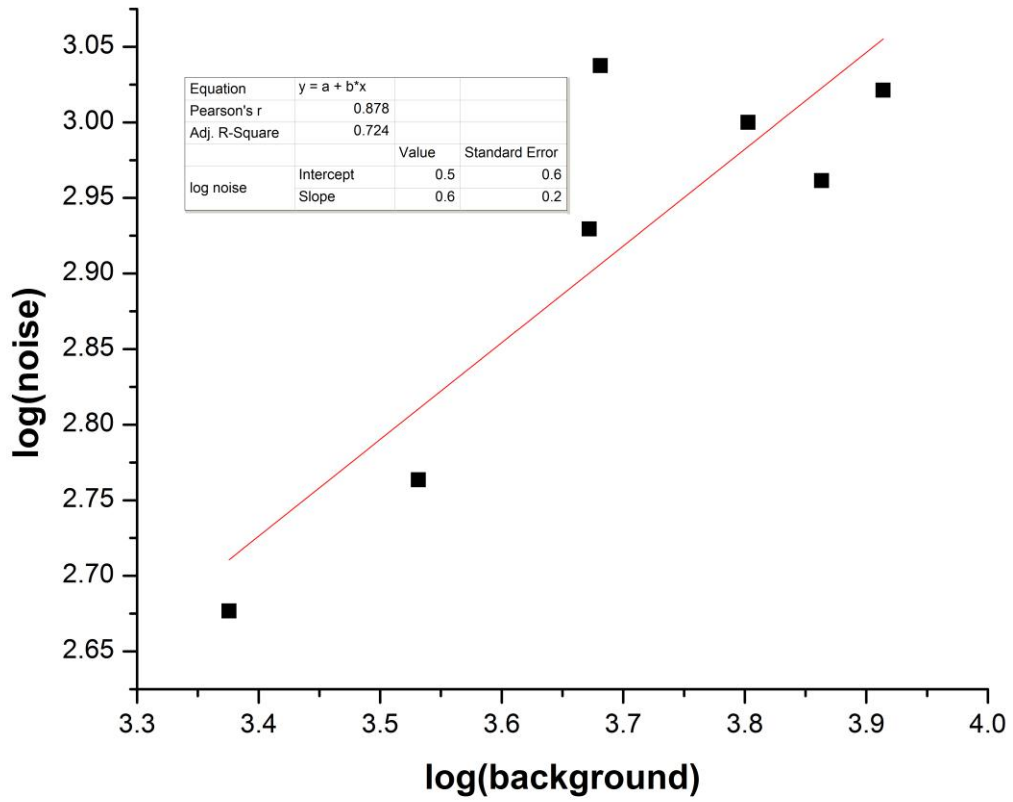


Figure 5-9. Background noise as function of background signal with early gate onset (11-531ns) in aluminum sample n1075.

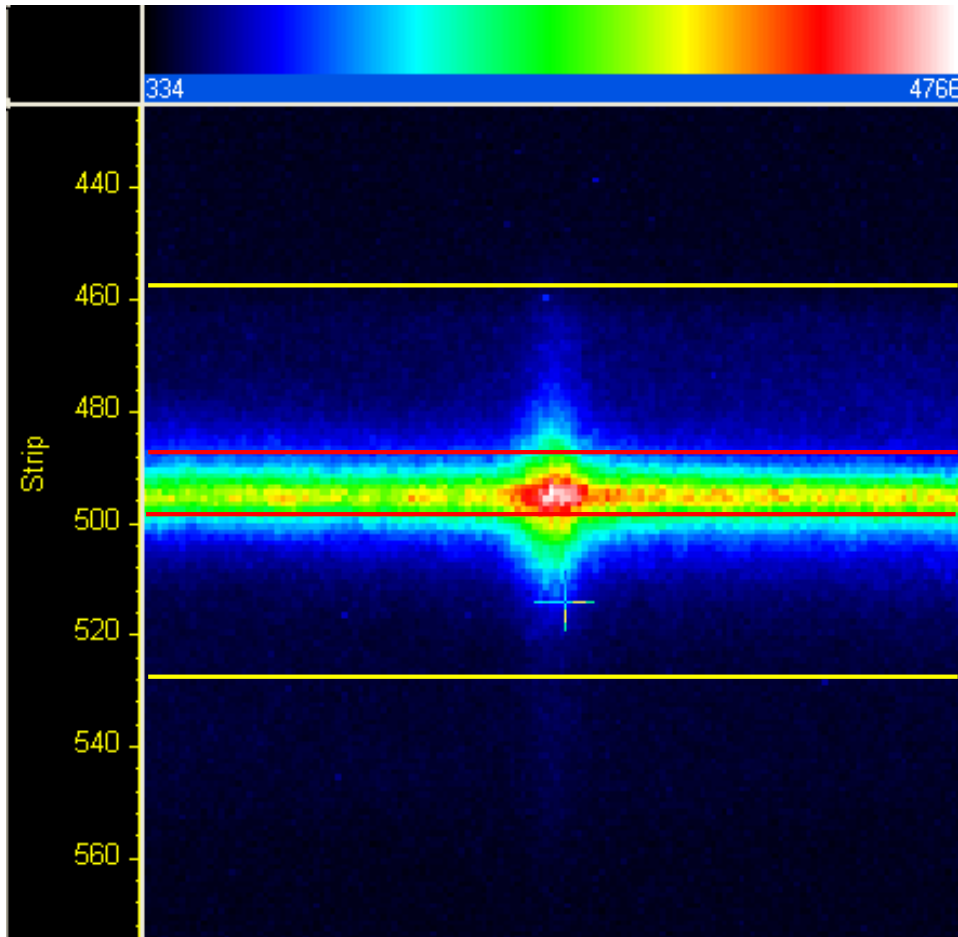


Figure 5-10. Binning regions for time-resolved S/N study. The central region (between red lines) was binned and two flanking regions (from red line to yellow lines) were binned above and below the central region. Note the intensity color code at the top of the figure.

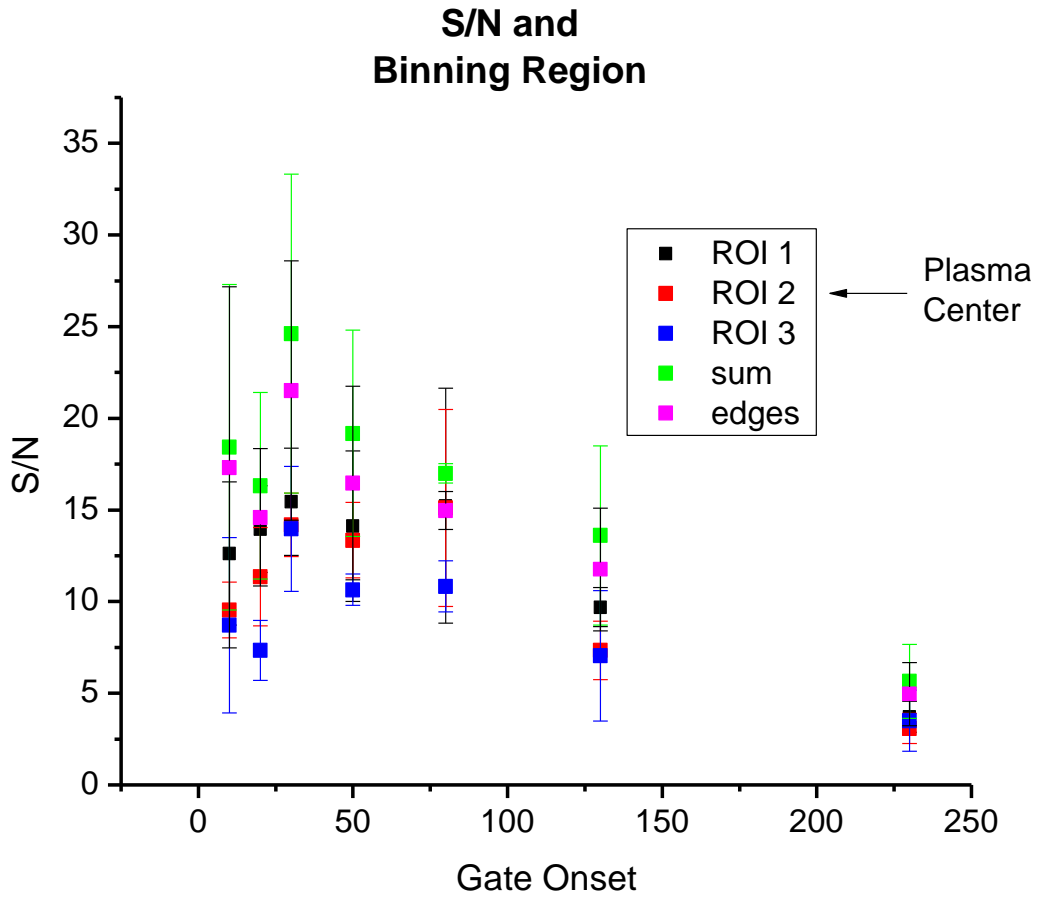


Figure 5-11. Time-resolved signal to background ratio in 327.4nm copper line in the binning regions indicated in Figure 5-10.

CHAPTER 6 CONCLUSIONS

Realistically, the studies in this dissertation are simply part of the initial survey of the analytical possibilities for powerchip lasers. As the technology matures and advances, no doubt the range of applications will grow and the figures of merit of the existing applications will improve. Recent advances in microchip and powerchip laser technology were mentioned in Chapter 1, but these were just a few of the developments in the field. For instance, microchip lasers have been coupled to diode-pumped fiber amplifiers in the past few years, allowing even higher irradiances from these modest sources.⁷⁶ Additionally, microchip lasers face competition from the compact actively q-switched diode-pumped lasers coming onto the market with user-controlled repetition rates (single trigger to 200kHz), higher energies, and three orders of magnitude less jitter, but longer pulses.⁷⁷

Clearly, the advantage of powerchip lasers lies in the simplicity and robustness with which they deliver a uniquely short pulse. Thus, applications that require sub-nanosecond pulses are likely to benefit from the laser. Fluorescence lifetimes, for instance, are generally measured with TCSPC, which requires both the short pulse lengths and the high repetition rates (MHz) available with some powerchip lasers. Although timing jitter should not be a problem for TCSPC applications, the available wavelengths will probably keep the number of microchip fluorescence applications low.

The particle lifetime fluorescence application discussed in Chapter 2 is a unique application both of this laser and the technique of time-resolved fluorescence. Adding spectra to the spectral lifetime data may add more selectivity, though it would need to be determined if the spectral information is orthogonal to the lifetime data or if the two

are highly correlated. The technique may have some limited application for discriminating between different substances in controlled situations, but applying it to separating an infinite variety of samples into an infinite number of possible categories is an impossibly difficult task. This being said, the concept suggested a surprising degree of selectivity and sensitivity even without spectra. As such, single-particle aerosol fluorescence lifetimes *might* be possible with a powerchip setup, but the method would be extremely optically demanding. More controlled particle movement (such as in a microfluidic chip) would be much more amenable to the technique.

The LIBS applications of powerchip lasers discussed in Chapters 4 and 5 benefit from the high repetition rate of the laser. The short pulse duration, on the other hand, serves mainly to allow LIBS at the low pulse energies. It remains to be seen what effect the pulse rate has on the typical figures of merit—side by side comparisons with longer-pulse low energy and high pulse rate lasers are necessary.

This investigation should serve as only a preliminary study of the physics and fundamentals of powerchip LIBS. If the technique is to become analytically useful, many questions remain to be answered. The fundamental limitations imposed by the uncertainty in the laser-sample interaction may well limit the applicability of the technique. Future investigations should focus on the physics of the breakdown with an eye towards making the laser-sample coupling as repeatable as possible. Additionally, the S/N characteristics of powerchip LIBS in different atmospheres should be examined in the light of the different physical evolutions that they demonstrated in Chapter 4.

The high peak power of these short-pulsed lasers allows access to 1064, 532, 355, and 266nm wavelengths. Preliminary data in our lab has found that LIBS plasmas

can be produced on highly pure fused silica using just $\sim 8\mu\text{J}$ of 266nm. LIBS plasma ignition and evolution should be studied at these wavelengths as well, as they may provide a more reproducible laser-sample interaction and, thus, a more reproducible technique. Double pulse combinations of powerchip UV laser ablation combined with IR reheating are intriguing. Additionally, the fiber-amplified versions of powerchips and microchips present interesting possibilities with the higher fluence that they represent, although repetition rates and robustness may be an issue.

Although the setup used for these time-resolved LIBS measurements is unwieldy, with its massive delay line and the uncertainties and difficulties that this adds, technology is rapidly simplifying the instrument. Modern compact, internally-controlled ICCD's with short signal insertion delays have decreased the optical delay necessary, perhaps even to the point where a few meters of multimode fiber could delay the laser without undue pulse stretching. In fact, the signal to noise studies in Chapter 5 indicate that only 10ns (3m) of optical delay would be necessary to optimize S/N with short insertion delay ICCD's. Improvements in laser technology, including simplified active Q-switches or multistage pumping regimes could eliminate the need for delay lines entirely. Newer compact ICCD's also allow higher gating frequencies- in the hundreds of kilohertz, which can allow the use of higher repetition rate lasers with intrapulse gating in order to improve shot noise and target sampling statistics. At the same time, if powerchip lasers are to find an application in scanning microLIBS, the S/N characteristics of single powerchip laser shots need study.

APPENDIX A
SPECTROSCOPIC DATA FOR SELECTED IRON TRANSITIONS

Table A-1. Spectroscopic parameters for atomic iron lines used in excitation temperature calculations

λ (nm)	E_n (cm ⁻¹)	E_m (cm ⁻¹)	g_m	A_{mn} (MHz)
370.55	416	27395	7	3.2
371.99	0	26875	11	16.2
372.25	704	27560	5	4.97
373.48	6928	33695	11	90.1
373.71	416	27167	9	14.2
374.56	704	27395	7	11.5
375.82	7728	34329	7	63.4
376.38	7986	34547	5	54.0

[Values taken from Sabsabi, M.; Cielo, P., Quantitative-Analysis of Aluminum-Alloys by Laser-Induced Breakdown Spectroscopy and Plasma Characterization. *Appl. Spectrosc.* **1995**, 49 (4), 499-507.]

APPENDIX B
COMPOSITION OF ALUMINUM STANDARDS

Table B-1. Composition of aluminum standards used in LIBS microanalysis (%)

	n3005	n1075	n4104	mn397	b8	d33	m7	r14	aa3	aa1	d28	sm9	sm10	s5	s4	s11	308	309	314
Al	97.58	99.7	87.9	98.81	88	84.92	85.47	79.59	69.14	-	81.55	85.34	84.7	-	83.79	89.2	-	-	-
Si	0.084	0.079	9.67	0.049	2.33	8.54	0.52	14	17	14.6	9.66	1.69	2.92	2.24	1.03	0.45	0.071	11.76	11.49
Mg	0.37	0.004	1.33	0.012	0.08	0.038	0.06	0.87	0.2	0.17	0.004	0.43	1.08	0.09	0.35	1.11	2.29	7E-04	0.181
Cu	0.44	0.007	0.15	0.0008	6.95	2.89	11.12	2.05	8	5.7	1.76	3	2.8	5.75	2.64	0.98	1.315	0.005	2.071
Zn	0.041	0.014	0.088	0.24	0.52	0.59	0.51	0.48	3.2	5.9	3.6	3.7	5.45	14.94	10.9	6.85	5.67	0.004	1.195
Fe	0.2	0.15	0.6	0.095	0.8	1.15	1.28	0.63	1.77	1.73	0.98	3.7	1.96	0.76	0.119	0.57	0.163	0.088	0.757
Mn	1.13	0.007	0.052	0.6	0.4	0.4	0.34	0.92	0.21	0.54	0.59	0.76	0.3	0.55	0.38	0.5	0.034	0.055	0.4
Ni	0.026	0.006	0.026	0.008	0.2	0.5	0.205	0.97	0.106	0.6	0.43	0.2	0.07	0.21	0.18	0.1	0.012	9E-04	0.221
Ti	0.05	0.011	0.024	0.14	0.16	0.055	0.065	0.16	0.078	0.03	0.033	0.07	0.06	0.11	0.12	0.065	0.029	0.056	0.164
Cr	0.026	0.006	0.026	0.008	0.17	0.047	0.05	0.11	0.1	0.28	0.21	0.38	0.2	0.11	0.13	0.115	0.196	5E-04	0.052
Sn	0.05	0.003	0.005	0.006	0.16	0.048	0.105	0.12	0.12	0.5	0.3	0.31	0.26	0.11	0.15	0.026	-	-	0.199
Pb	0.005	0.003	0.005	0.006	0.17	0.14	0.11	0.1	0.08	0.38	0.34	0.32	0.25	0.12	0.13	0.022	-	-	0.221
Bi	0.006	0.003	0.09	0.007	0.1	0.68	-	-	-	-	0.54	-	-	-	-	-	-	-	94 ppm
Zr	0.006	0.004	0.005	0.007	-	-	0.17	-	-	-	0.123	-	-	0.06	-	-	-	-	55.2 ppm
Cd	-	-	-	-	-	-	-	-	-	-	-	0.021	-	-	-	0.015	-	-	-

LIST OF REFERENCES

1. T. H. Maiman, Stimulated Optical Radiation in Ruby. *Nature* 1960, *187*. 493-494.
2. J. E. Geusic, H. M. Marcos, L. G. Vanuitert, Laser Oscillations in Nd-Doped Yttrium Aluminum Yttrium Gallium + Gadolinium Garnets (Continuous Operation of $Y_3Al_5O_{12}$ Pulsed Operation of $Y_3Ga_5O_{15}$ + $Gd_3Ga_5O_{12}$ Rm Temp E). *Applied Physics Letters* 1964, *4*. 182.
3. J. J. Zayhowski, A. Mooradian, Single-Frequency Microchip Nd Lasers. *Optics Letters* 1989, *14*. 24-26.
4. J. J. Zayhowski, Microchip lasers. *Optical Materials* 1999, *11*. 255-267.
5. J. J. Zayhowski, D. Welford, J. Harrison, in *The Handbook of Photonics*, ed. M. C. Gupta, J. Ballato. CRC Press: Boca Raton, 2007.
6. J. J. Zayhowski, Q-Switched Operation of Microchip Lasers. *Optics Letters* 1991, *16*. 575-577.
7. Y. C. Chen, S. Q. Li, K. K. Lee, S. H. Zhou, Self-Stabilized Single-Longitudinal-Mode Operation in a Self-Q-Switched Cr,Ndyag Laser. *Optics Letters* 1993, *18*. 1418-1419.
8. J. J. Zayhowski, C. Dill, Diode-Pumped Microchip Lasers Electrooptically Q-Switched at High Pulse Repetition Rates. *Optics Letters* 1992, *17*. 1201-1203.
9. H. Sakai, H. Kan, T. Taira, > 1 MW peak power single-mode high-brightness passively Q-switched Nd^{3+} :YAG microchip laser. *Opt. Express* 2008, *16*. 19891-19899.
10. JDS-Uniphase *Diode Pumped Solid State PowerChip NanoLasers User's Manual*; 2002.
11. O. Hugon, I. A. Paun, C. Ricard, B. van der Sanden, E. Lacot, O. Jacquin, A. Witomski, Cell imaging by coherent backscattering microscopy using frequency-shifted optical feedback in a microchip laser. *Ultramicroscopy* 2008, *108*. 523-528.
12. B. R. Rankin, R. R. Kellner, S. W. Hell, Stimulated-emission-depletion microscopy with a multicolor stimulated-Raman-scattering light source. *Opt. Lett.* 2008, *33*. 2491-2493.
13. E. T. Ritschdorff, J. B. Shear, Multiphoton Lithography Using a High-Repetition Rate Microchip Laser. *Analytical Chemistry* 2010, *82*. 8733-8737.
14. U. P. Paul, Li, M. L. Lee, P. B. Farnsworth, Compact Detector for Proteins Based on Two-Photon Excitation of Native Fluorescence. *Analytical Chemistry* 2005, *77*. 3690-3693.

15. (a) I. B. Gornushkin, K. Amponsah-Manager, B. W. Smith, N. Omenetto, J. D. Winefordner, Microchip laser-induced breakdown spectroscopy: A preliminary feasibility investigation. *Appl. Spectrosc.* 2004, 58. 762-769; (b) K. Amponsah-Manager, N. Omenetto, B. W. Smith, I. B. Gornushkin, J. D. Winefordner, Microchip laser ablation of metals: investigation of the ablation process in view of its application to laser-induced breakdown spectroscopy. *J. Anal. At. Spectrom.* 2005, 20. 544-551, DOI: 10.1039/b419109a; (c) C. Lopez-Moreno, K. Amponsah-Manager, B. W. Smith, I. B. Gornushkin, N. Omenetto, S. Palanco, J. J. Laserna, J. D. Winefordner, Quantitative analysis of low-alloy steel by microchip laser induced breakdown spectroscopy. *J. Anal. At. Spectrom.* 2005, 20. 552-556, DOI: 10.1039/b419173k; (d) J. Wormhoudt, F. J. Iannarilli, S. Jones, K. D. Annen, A. Freedman, Determination of carbon in steel by laser-induced breakdown spectroscopy using a microchip laser and miniature spectrometer. *Appl. Spectrosc.* 2005, 59. 1098-1102.
16. J. R. Lakowicz, *Principles of Fluorescence Spectroscopy*. 3 ed.; Springer: New York, 2006.
17. A. G. Szabo, D. M. Rayner, Fluorescence Decay of Tryptophan Conformers in Aqueous-Solution. *Journal of the American Chemical Society* 1980, 102. 554-563.
18. J. R. Lakowicz, G. Laczko, I. Gryczynski, Picosecond resolution of tyrosine fluorescence and anisotropy decays by 2-GHz frequency-domain fluorometry. *Biochemistry* 1987, 26. 82-90.
19. E. Leroy, H. Lami, G. Laustriat, Fluorescence Lifetime and Quantum Yield of Phenylalanine Aqueous Solutions. Temperature and Concentration Effects. *Photochem. Photobiol.* 1971, 13. 411-421.
20. J. W. Longworth, in *Excited States of Proteins and Nucleic Acids*, ed. R. F. Steiner, I. Weinryb. Plenum Press: New York, London, 1971, pp 319-484.
21. K. Blinova, S. Carroll, S. Bose, A. V. Smirnov, J. J. Harvey, J. R. Knutson, R. S. Balaban, Distribution of Mitochondrial NADH Fluorescence Lifetimes: Steady-State Kinetics of Matrix NADH Interactions. *Biochemistry* 2005, 44. 2585-2594.
22. J. R. Lakowicz, H. Szmecinski, K. Nowaczyk, M. L. Johnson, Fluorescence Lifetime Imaging of Free and Protein-Bound NADH. *Proc. Natl. Acad. Sci. U. S. A.* 1992, 89. 1271-1275.
23. M. S. Ammor, Recent advances in the use of intrinsic fluorescence for bacterial identification and characterization. *Journal of Fluorescence* 2007, 17. 455-459.
24. J. Ho, Future of biological aerosol detection. *Anal. Chim. Acta* 2002, 457. 125-148.
25. S. Ammor, K. Yaakoubi, I. Chevallier, E. Dufour, Identification by fluorescence spectroscopy of lactic acid bacteria isolated from a small-scale facility producing traditional dry sausages. *Journal of Microbiological Methods* 2004, 59. 271-281.

26. M. S. Ammor, S. Delgado, P. Álvarez-Martín, A. Margolles, B. Mayo, Reagentless identification of human bifidobacteria by intrinsic fluorescence. *Journal of Microbiological Methods* 2007, 69. 100-106.
27. B. C. Spector, L. Reinisch, D. Smith, J. A. Werkhaven, Noninvasive Fluorescent Identification of Bacteria Causing Acute Otitis Media in a Chinchilla Model. *The Laryngoscope* 2000, 110. 1119-1123.
28. S. K. Brahma, M. P. Baek, D. Gaskill, R. K. Force, W. H. Nelson, J. Sperry, The Rapid Identification of Bacteria Using Time-Resolved Fluorescence and Fluorescence Excitation Spectral Methods. *Applied Spectroscopy* 1985, 39. 869-872.
29. R. A. Dalterio, W. H. Nelson, D. Britt, J. F. Sperry, J. F. Tanguay, S. L. Suib, The Steady-State and Decay Characteristics of Primary Fluorescence from Live Bacteria. *Applied Spectroscopy* 1987, 41. 234-241.
30. A. Thomas, D. Sands, D. Baum, L. To, G. O. Rubel, Emission wavelength dependence of fluorescence lifetimes of bacteriological spores and pollens. *Applied Optics* 2006, 45. 6634-6639.
31. P. P. Hairston, J. Ho, F. R. Quant, Design of an instrument for real-time detection of bioaerosols using simultaneous measurement of particle aerodynamic size and intrinsic fluorescence. *J. Aerosol. Sci.* 1997, 28. 471-482.
32. TSI Incorporated. UVAPS Operator's Manual. Shoreville, Minnesota, 2011, vol. 2011.
33. J. Ho, M. Spence, P. Hairston, Measurement of biological aerosol with a fluorescent aerodynamic particle sizer (FLAPS): correlation of optical data with biological data. *Aerobiologia* 1999, 15. 281-291.
34. X. Wu, J. A. Merten, N. Omenetto, B. W. Smith, J. D. Winefordner, Development, Characterization, and Application of a Versatile Single Particle Detection Apparatus for Time-Integrated and Time-Resolved Fluorescence Measurements—Part II: Experimental Evaluation. *Laser Chemistry* 2009, 2009. 14.
35. G. Chen, P. Nachman, R. G. Pinnick, S. C. Hill, R. K. Chang, Conditional-firing aerosol-fluorescence spectrum analyzer for individual airborne particles with pulsed 266-nm laser excitation. *Opt. Lett.* 1996, 21. 1307-1309.
36. Y.-I. Pan, P. Cobler, S. Rhodes, A. Potter, T. Chou, S. Holler, R. K. Chang, R. G. Pinnick, J.-P. Wolf, High-speed, high-sensitivity aerosol fluorescence spectrum detection using a 32-anode photomultiplier tube detector. *Review of Scientific Instruments* 2001, 72. 1831-1836.
37. K. Davitt, Y. K. Song, W. R. Patterson, A. V. Nurmikko, M. Gherasimova, J. Han, Y. L. Pan, R. K. Chang, 290 and 340nm UV LED arrays for fluorescence detection from single airborne particles. *Optics Express* 2005, 13. 9548-9555.

38. P. Kaye, W. R. Stanley, E. Hirst, E. V. Foot, K. L. Baxter, S. J. Barrington, Single particle multichannel bio-aerosol fluorescence sensor. *Opt. Express* 2005, *13*. 3583-3593.
39. A. L. van Wuijckhuijse, M. A. Stowers, C. E. Kientz, J. C. M. Marijnissen, B. Scarlett, Bioaerosol detection by aerosol tof-mass spectrometry : Application of Matrix Assisted Laser Desorption/Ionisation. *J. Aerosol. Sci.* 2000, *31*. 1013-1014.
40. A. L. van Wuijckhuijse, M. A. Stowers, W. A. Kleefsman, B. L. M. van Baar, C. E. Kientz, J. C. M. Marijnissen, Matrix-assisted laser desorption/ionisation aerosol time-of-flight mass spectrometry for the analysis of bioaerosols: development of a fast detector for airborne biological pathogens. *J. Aerosol. Sci.* 2005, *36*. 677-687.
41. D. P. Fergenson, M. E. Pitesky, H. J. Tobias, P. T. Steele, G. A. Czerwieniec, S. C. Russell, C. B. Lebrilla, J. M. Horn, K. R. Coffee, A. Srivastava, S. P. Pillai, M.-T. P. Shih, H. L. Hall, A. J. Ramponi, J. T. Chang, R. G. Langlois, P. L. Estacio, R. T. Hadley, M. Frank, E. E. Gard, Reagentless Detection and Classification of Individual Bioaerosol Particles in Seconds. *Analytical Chemistry* 2003, *76*. 373-378.
42. X. Wu, N. Omenetto, J. D. Winefordner, Development, Characterization, and Application of a Versatile Single Particle Detection Apparatus for Time-Integrated and Time-Resolved Fluorescence Measurements—Part I: Theoretical Considerations. *Laser Chemistry* 2009, *2009*.
43. X. Wu. Design, Construction and Experimental Characterization of a Versatile Apparatus for Detecting Single Aerosol Particles. Research, University of Florida, Gainesville, 2006.
44. X. Wu, N. Omenetto, B. W. Smith, J. D. Winefordner, Single Particle Fluorescence: A Simple Experimental Approach to Evaluate Coincidence Effects. *Appl. Spectrosc.* 2007, *61*. 711-718.
45. B. V. Bronk, L. Reinisch, Variability of Steady-State Bacterial Fluorescence with Respect to Growth Conditions. *Applied Spectroscopy* 1993, *47*. 436-440.
46. Picoquant. Fluofit Software Manual. Picoquant GmbH: Berlin.
47. (a) V. Sivaprakasam, A. Huston, C. Scotto, J. Eversole, Multiple UV wavelength excitation and fluorescence of bioaerosols. *Opt. Express* 2004, *12*. 4457-4466; (b) J. R. Stephens, ed. Los Alamos National Laboratory. Edgewood Chemical Biological Center, 1999, p 46; (c) B. V. Bronk, L. Reinisch, Variability of Steady-State Bacterial Fluorescence with Respect to Growth-Conditions. *Applied Spectroscopy* 1993, *47*. 436-440.
48. R. Vehring, C. L. Aardahl, E. J. Davis, G. Schweiger, D. S. Covert, Electrodynamic trapping and manipulation of particle clouds. *Review of Scientific Instruments* 1997, *68*. 70-78.

49. A. H. Thomas, C. Lorente, A. L. Capparelli, M. R. Pokhrel, A. M. Braun, E. Oliveros, Fluorescence of pterin, 6-formylpterin, 6-carboxypterin and folic acid in aqueous solution: pH effects. *Photochemical & Photobiological Sciences* 2002, 1. 421-426.
50. F. Brech, presented in part at X CSI, University of Maryland, June 20, 1962.
51. G. M. Weyl, in *Laser-Induced Plasmas and Applications*, ed. L. J. Radziemski, D. A. Cremers. Marcel Dekker, Inc.: New York, 1989, pp 1-67.
52. R. E. Russo, X. L. Mao, J. H. Yoo, J. J. Gonzalez, in *Laser-Induced Breakdown Spectroscopy*, ed. J. P. Singh, S. N. Thakur. Elsevier: Amsterdam, 2007, pp 49-82.
53. R. G. Root, in *Laser-Induced Plasmas and Applications*, ed. L. J. Radziemski, D. A. Cremers. Marcel Dekker, Inc.: New York, 1989, pp 69-103.
54. G. G. Sahasrabudhe, S. D. Lambade, Temperature dependence of the collective phonon relaxation time and acoustic damping in Ge and Si. *Journal of Physics and Chemistry of Solids* 1999, 60. 773-785.
55. J.-F. Y. Gravel, D. Boudreau, Study by focused shadowgraphy of the effect of laser irradiance on laser-induced plasma formation and ablation rate in various gases. *Spectrochimica Acta Part B: Atomic Spectroscopy* 2009, 64. 56-66.
56. D. W. Hahn, N. Omenetto, Laser-Induced Breakdown Spectroscopy (LIBS), Part I: Review of Basic Diagnostics and Plasma-Particle Interactions: Still-Challenging Issues Within the Analytical Plasma Community. *Appl. Spectrosc.* 2010, 64. 335A-366A.
57. E. H. Piepmeier, H. V. Malmstadt, Q-Switched laser energy absorption in the plume of an aluminum alloy. *Analytical Chemistry* 1969, 41. 700-707.
58. G. Cristoforetti, A. De Giacomo, M. Dell'Aglio, S. Legnaioli, E. Tognoni, V. Palleschi, N. Omenetto, Local Thermodynamic Equilibrium in Laser-Induced Breakdown Spectroscopy: Beyond the McWhirter criterion. *Spectrochimica Acta Part B: Atomic Spectroscopy* 2010, 65. 86-95.
59. R. W. P. McWhirter, in *Plasma Diagnostic Techniques*, ed. R. H. Huddleston, S. L. Leonard. Academic Press: New York, 1965, pp 201-264.
60. M. T. Taschuk, I. V. Cravetchi, Y. Y. Tsui, R. Fedosejevs, in *Laser-Induced Breakdown Spectroscopy*, ed. J. Singh, S. N. Thakur. Elsevier: Amsterdam, 2007, pp 173-196.
61. J. M. Mermet, P. Mauchien, J. L. Lacour, Processing of shot-to-shot raw data to improve precision in laser-induced breakdown spectrometry microprobe. *Spectrochimica Acta Part B: Atomic Spectroscopy* 2008, 63. 999-1005.

62. M. T. Taschuk, Y. Y. Tsui, R. Fedosejevs, Detection and mapping of latent fingerprints by laser-induced breakdown spectroscopy. *Appl. Spectrosc.* 2006, *60*. 1322-1327.
63. R. B. Marinenko, NIST Standards for Microanalysis and the Certification Process. *Journal of Research of the National Institute of Standards and Technology* 2002, *107*. 687-691.
64. D. Menut, P. Fichet, J. L. Lacour, A. Rivoallan, P. Mauchien, Micro-laser-induced breakdown spectroscopy technique: a powerful method for performing quantitative surface mapping on conductive and nonconductive samples. *Applied Optics* 2003, *42*. 6063-6071.
65. D. Kossakovski, J. L. Beauchamp, Topographical and Chemical Microanalysis of Surfaces with a Scanning Probe Microscope and Laser-Induced Breakdown Spectroscopy. *Analytical Chemistry* 2000, *72*. 4731-4737.
66. I. V. Cravetchi, M. Taschuk, Y. Y. Tsui, R. Fedosejevs, Scanning microanalysis of Al alloys by laser-induced breakdown spectroscopy. *Spectrochimica Acta Part B-Atomic Spectroscopy* 2004, *59*. 1439-1450.
67. G. W. Rieger, M. Taschuk, Y. Y. Tsui, R. Fedosejevs, Laser-induced breakdown spectroscopy for microanalysis using submillijoule UV laser pulses. *Appl. Spectrosc.* 2002, *56*. 689-698.
68. H. J. Häkkinen, J. E. I. Korppi-Tommola, UV-Laser Plasma Study of Elemental Distributions of Paper Coatings. *Appl. Spectrosc.* 1995, *49*. 1721-1728.
69. A. Freedman, J. F. J. Iannarilli, J. C. Wormhoudt, Aluminum alloy analysis using microchip-laser induced breakdown spectroscopy. *Spectrochimica Acta Part B: Atomic Spectroscopy* 2005, *60*. 1076-1082.
70. M. Sabsabi, P. Cielo, Quantitative-Analysis of Aluminum-Alloys by Laser-Induced Breakdown Spectroscopy and Plasma Characterization. *Appl. Spectrosc.* 1995, *49*. 499-507.
71. R. C. Weast. *CRC Handbook of Chemistry and Physics*. CRC Press, Inc.: Boca Raton, 66 edn., 1985.
72. J. A. Aguilera, C. Aragon, A comparison of the temperatures and electron densities of laser-produced plasmas obtained in air, argon, and helium at atmospheric pressure. *Applied Physics a-Materials Science & Processing* 1999, *69*. S475-S478.
73. Y. Iida, Effects of atmosphere on laser vaporization and excitation processes of solid samples. *Spectrochimica Acta Part B: Atomic Spectroscopy* 1990, *45*. 1353-1367.
74. H. Griem, *Spectral Line Broadening by Plasmas*. Academic Press: New York, 1974; Vol. 39, p 408.

75. C. A. Henry, P. K. Diwakar, D. W. Hahn, Investigation of helium addition for laser-induced plasma spectroscopy of pure gas phase systems: Analyte interactions and signal enhancement. *Spectrochimica Acta Part B-Atomic Spectroscopy* 2007, 62. 1390-1398.
76. (a) C. Bohling, K. Hohmann, D. Scheel, C. Bauer, W. Schippers, J. Burgmeier, U. Willer, G. Holl, W. Schade, All-fiber-coupled laser-induced breakdown spectroscopy sensor for hazardous materials analysis. *Spectrochimica Acta Part B: Atomic Spectroscopy* 2007, 62. 1519-1527; (b) A. V. Kir'yanov, S. M. Klimentov, I. V. Mel'nikov, A. V. Shestakov, in *CLEO/Europe and EQEC 2009 Conference Digest*. Optical Society of America, 2009.
77. Compact Laser Solutions GmbH. *Product Guide*. Berlin, 2011, vol. 2011.

BIOGRAPHICAL SKETCH

Jonathan Merten was born and raised in Jacksonville, Florida. He attended the University of Virginia, where he received a B.S. in chemistry with a minor in Spanish in 1999. He spent the following two years teaching high school chemistry and playing soccer with his students on the eastern shore of Lake Victoria, Tanzania where he served as a Peace Corps volunteer. Following his return from Africa, he joined the chemistry program at the University of Florida in 2004. Jonathan worked on a variety of projects under the supervision of Jim Winefordner, Nico Omenetto and Ben Smith.